Biodistribution and biological impact of nanoparticles using multimodality imaging techniques : (Magnetic resonance imaging)

Achraf Al Faraj

N° d'ordre: 81-2009 Année 2009

THESE

présentée

devant l'UNIVERSITE CLAUDE BERNARD - LYON I

pour l'obtention

du DIPLOME NATIONAL DE DOCTORAT

(Arrêté du 7 août 2006)

Par

Achraf AL FARAJ

Biodistribution et Effet Biologique des Nanoparticules Utilisant des Techniques d'Imagerie Multimodale (Imagerie de Résonance Magnétique)

Soutenue le 30 Juin 2009

Spécialité : Ingénierie Biomédicale

Directeurs de thèse: Pr. Emmanuelle Canet-Soulas
Dr. Yannick Crémillieux

Jury :

Pr. Robert Muller	Président
Dr. Nicolau Beckmann	Rapporteur
Pr. Patrick Berger	Rapporteur
Dr. Ghislaine Lacroix	Examinateur
Dr. Jorge Boczkowski	Examinateur
Pr. Emmanuelle Canet-Soulas	Directeur
Dr. Yannick Crémillieux	Directeur

UNIVERSITE CLAUDE BERNARD - LYON 1

Président de l'Université	**M. le Professeur L. Collet**
Vice-président du Conseil Scientifique	M. le Professeur J.F. Mornex
Vice-président du Conseil d'Administration	M. le Professeur G. Annat
Vice-président du Conseil des Etudes et de la Vie Universitaire	M. le Professeur D. Simon
Secrétaire Général	M. G. Gay

UFR SANTE

Composantes

UFR de Médecine Lyon R.T.H. Laënnec	Directeur : M. le Professeur P. Cochat
UFR de Médecine Lyon Grange-Blanche	Directeur : M. le Professeur X. Martin
UFR de Médecine Lyon-Nord	Directeur : M. le Professeur J. Etienne
UFR de Médecine Lyon-Sud	Directeur : M. le Professeur F.N. Gilly
UFR d'Odontologie	Directeur : M. O. Robin
Institut des Sciences Pharmaceutiques et Biologiques	Directeur : M. le Professeur F. Locher
Institut Techniques de Réadaptation	Directeur : M. le Professeur Y. Matillon
Département de Formation et Centre de Recherche en Biologie Humaine	Directeur : M. le Professeur P. Farge

UFR SCIENCES ET TECHNOLOGIE

Composantes

UFR de Physique	Directeur : Mme. la Professeure S. Fleck
UFR de Biologie	Directeur : M. le Professeur H. Pinon
UFR de Mécanique	Directeur : M. le Professeur H. Ben Hadid
UFR de Génie Electrique et des Procédés	Directeur : M. le Professeur G. Clerc
UFR Sciences de la Terre	Directeur : M. le Professeur P. Hantzpergue
UFR de Mathématiques	Directeur : M. le Professeur A. Goldman
UFR d'Informatique	Directeur : M. le Professeur S. Akkouche
UFR de Chimie Biochimie	Directeur : Mme. la Professeure H. Parrot
UFR Sciences et Techniques des Activités Physiques et Sportives	Directeur : M. C. Collignon
Observatoire de Lyon	Directeur : M. le Professeur R. Bacon
Institut des Sciences et des Techniques de l'Ingénieur de Lyon	Directeur : M. le Professeur J. Lieto
Institut Universitaire de Technologie A	Directeur : M. le Professeur M. C. Coulet
Institut Universitaire de Technologie B	Directeur : M. le Professeur R. Lamartine
Institut de Science Financière et d'Assurance	Directeur : M. le Professeur J.C. Augros

Université Claude Bernard Lyon 1

Creatis LRMN

Biodistribution and biological impact of Nanoparticles Using Multimodality Imaging Techniques (Magnetic Resonance Imaging)

Achraf AL FARAJ

Inserm cnrs INSA LYON

Remerciements

Mes premiers hommages vont à celui pour qui cette page est bien loin de suffire à exprimer toute ma reconnaissance. Emmanuelle et Yannick, je tiens à vous exprimer de tout mon cœur ma gratitude, ma reconnaissance et mes profonds remerciements pour m'avoir accordé toute votre confiance et m'assurer les moyens de mener d'une façon autonome et idéale cette thèse. Vous restez pour toujours mon exemple de chercheur, et j'espère que nous restons pour toujours des collaborateurs et des amis.

Je vous suis énormément reconnaissant de m'avoir transmis votre intérêt pour la recherche, et vos compétences scientifiques d'excellent niveau. Je n'oublie jamais les moments passés ensemble au laboratoire et durant tous les congrès et voyages …

Je tiens à remercier Dr. Nicolau Beckmann et Pr. Patrick Berger pour leur rapport élogieux sur mon manuscrit de thèse et Pr. Robert Muller pour avoir accepter de présider mon jury de thèse. Sans oublier Dr. Jorge Bocskowski pour la participation au jury et ses conseils et compliments durant les réunions de l'ANR RespiNTTox. Je réserve une place spéciale à Dr. Ghislaine Lacroix pour son amitié, sa collaboration, ses conseils et sa participation au jury. Mes visites à l'INERIS resteront mes plus beaux souvenirs.

J'ai eu également le plaisir de collaborer avec d'autres laboratoires ou de manipuler dans différents centres. Je pense en premier lieu à Simone Peyrol du CECIL pour les conseils et initiations en microscopie électronique. Merci également à Florence Fauvelle du CRSSA pour la spectroscopie HRMAS, Valérie Martinez du LPCM pour la spectroscopie RAMAN et Florence Lagarde du laboratoire des sciences analytiques pour le dosage chimique.

Cette thèse est pour moi une expérience très enrichissante aussi bien sur le plan professionnel que personnel. Elle m'a permis en particulier de faire la connaissance de plusieurs amis avec qui j'ai passé des moments très agréables.
Je tiens à exprimer ma profonde reconnaissance à toi Kasia pour tout l'aide durant les manips d'hélium et les conseils scientifiques et personnels que tu m'as partagés. Tu resteras pour toujours l'exemple d'une scientifique avec un esprit ouvert et collaboratif.

Mes vifs remerciements vont à Fabienne pour les centaines des bons de commande, ordres de mission et réservations... Je suis vraiment reconnaissant de ton travail idyllique.

Mes remerciements s'adressent également à mes collègues du laboratoire. La liste est très longue et même si vous n'êtes pas nominalement ou formellement mentionnés dans ces lignes vous restez toujours dans mon souvenir et mon cœur.
Je réserve une place spéciale à Aziz pour son aide, son amitié et les litres de thé qu'on a bus ensemble et à Amine pour sa disponibilité (même si toujours en retard)! ;)
Je n'oublie jamais Monica, Anoop … et tous les algécociens …
Un grand merci à Sophie, Valérie, Hasan, Vasile, Magda et tous les abonnés de la Newsletter d'arnob !

Ce travail a été également illuminé par la présence de mes amis « Libanais » à Lyon avec des moments de détente, de joie et de fraternité. Merci à mes co-équipiers de foot (Bilal, Mouhamad, Walid, Ouwais et tous les autres …) juste pour les matchs que j'ai gagnés chaque dimanche ! Merci également à tous mes frères et sœurs pour les picnics, les moments agréables ensemble et à toute votre confiance: Osman, Houssam et Hodna, Omar et Najah, Salem … je vous suis vraiment reconnaissant.
Sans oublier ceux qui était toujours à ma côté : Adnan, Maysarah, mon cousin Maher, et mes oncles … Avec vous tous, je n'ai jamais senti que je suis loin de mon pays.

Pour finir, je dédie ce travail à mon père (Mahmoud) et ma mère (Aicha) qui m'ont constamment encouragé et donné les moyens de poursuivre mes études pour être toujours le meilleur. Je tiens ici à vous exprimer mes remerciements, ma gratitude et ma reconnaissance (et c'est encore très peu) pour les sacrifices et le dévouement que vous m'avez faits. J'espère que vous avez trouvé le fruit de votre travail !!

J'adresse également un remerciement particulier à mon frère (Ihab) et mes sœurs (Dana et Alaà), qui malgré la distance qui nous a séparés, j'ai senti qu'ils étaient toujours à côté de moi pour me soutenir et m'encourager.

Et finalement, je réserve ma dernière affection « mention spéciale » à mon épouse Baraà qui m'a partagé tous ces moments et qu'aucun remerciement ne suffira pour lui exprimer ma reconnaissance et à mon petit Mido qui m'a donné toute cette motivation pour obtenir cette thèse avec la plus haute distinction mention très honorable et qui restera pour toujours mon rayon de soleil et ma source d'espoir. Je pense au jour que je lis les remerciements de sa thèse !!!

Achraf

TABLE OF CONTENT

FRENCH SUMMARY

RESUME FRANCAIS

Une problématique récente apparue concernant les effets sur la santé à une exposition aux particules ultrafines ou nanoparticules nécessite une attention particulière. Ces nanoparticules industriellement fabriquées ont révolutionné le domaine de la nanotechnologie avec des applications dans des domaines aussi variés que l'électronique, la mécanique, le biomédical, la pharmacie, la cosmétologie…

Les mêmes propriétés physicochimiques qui rendent ces nanoparticules aussi fascinantes attirent l'attention sur leur toxicité notamment en termes d'exposition accidentelle par voie respiratoire. En plus de la toxicité intrinsèque qui peut varier par rapport aux caractéristiques de chaque nanomatériaux, des études d'épidémiologie et de toxicologie ont montré que lorsqu'on diminue en taille pour atteindre des dimensions nanométriques, les effets de surface deviennent prépondérants par rapport aux effets de volume et ainsi différentes propriétés physico-chimique peuvent apparaître. Ces nanoparticules peuvent également potentiellement traverser les barrières physiologiques après une exposition par inhalation.

Parmi ces nanoparticules, les nanotubes de carbone (NTC) connaissent une utilisation croissante dans le domaine de la nanotechnologie en raison de leurs propriétés uniques (mécanique, électronique et thermique …) et l'impact biologique de ces nano-objets mérite une attention particulière.

Ces nano-objets cylindriques de quelques nanomètres de diamètre sont constitués d'atomes de carbone sous forme hexagonale arrangées en monofeuillet de graphène (SW: « single-walled ») ou multifeuillets (MW: « multi-walled »).

Outre leur exposition accidentelle par voie pulmonaire en cours de production et d'utilisation, l'exploitation des NTC en nanomédecine est potentiellement une perspective intéressante comme agents de contraste pour le diagnostic et/ou la thérapeutique. Leur structure particulière leur permet de traverser les barrières biologiques pour délivrer localement des médicaments et leurs propriétés physicochimiques notamment la possibilité de modifier ou fonctionnaliser leur surface peuvent les rendre plus biocompatibles.

Récemment différentes études ont été menées pour évaluer la biodistribution et l'impact biologique des NTC monofeuillets que ce soit après une exposition par voie pulmonaire (instillation intratrachéal, instillation …) ou une application dans le domaine de la nanomédecine (injection intraveineuse). Les données publiées restent contradictoires ou manquent de spécificité d'où la nécessité de développer des techniques alternatives notamment d'imagerie non-invasive permettant un suivi longitudinal des ces nanoparticules dépendant de leur propriétés intrinsèques.

Parmi les techniques d'imagerie médicales les plus utilisées, l'imagerie par résonance magnétique (IRM) présente l'avantage d'être complètement non-invasive et ne nécessite pas une exposition à des agents ionisants permettant ainsi un suivi longitudinal.

L'IRM proton (standard) donne des images morphologiques et fonctionnelles avec une très bonne résolution spatiale et fonctionnelle des différents organes à l'exception des poumons en raison de leur faible densité en proton et la susceptibilité magnétique liée à l'hétérogénéité des structures microscopiques (interfaces air-tissus). Mais, grâce à l'introduction des gaz rares hyperpolarisés (hélium-3) comme agents de contraste qui diffusent dans les espaces alvéolaires, l'imagerie pulmonaire est désormais possible.

L'objectif de la thèse est en premier lieu de développer des protocoles d'imagerie (pulmonaire et systémique) permettant un suivi longitudinal des nanoparticules après exposition à un modèle de rat par voie pulmonaire ou injection intraveineuse pour des applications en nanomédecine puis de combiner les résultats d'IRM avec des techniques de microscopie optique et électronique pour permettre une évaluation complète de leur biodistribution et leur impact biologique (nanotoxicité).

Parmi les agents de contraste les plus utilisés en IRM, les nanoparticules d'oxyde de fer (USPIO: « ultra-small particle iron oxide ») représentent un bon choix pour valider notre approche en raison de leur taille nanométrique (20-30 nm) et de leur effet de susceptibilité magnétique combinant des effets T2 et T2* (contraste négatif) permettant ainsi leur détection par IRM. La présence de ces nanoparticules à base de fer affecte le contraste du tissu par rapport à la séquence utilisée et se manifeste par une perte de signal (hypo-signal).

Dans le premier manuscrit de cette thèse, la biodistribution de la magnétite (USPIO) exposée par voie pulmonaire (instillation intra-trachéal) à un modèle de rat est évaluée longitudinalement utilisant l'IRM pulmonaire (hélium-3) et systémique (proton).

En IRM pulmonaire hélium-3, les acquisitions utilisant une séquence radiale ont été menées en permettant aux animaux de respirer spontanément à partir d'un masque rempli d'hélium-3 hyperpolarisé. Après une première étude de sensibilité de détection de la magnétite, un temps d'écho de 1-ms a été choisi comme un bon compromis entre la sensibilité de détection et la qualité de l'image.

Un suivi longitudinal de 2 semaines a été ensuite effectué après instillation de 0.5mg de magnétite. L'imagerie de ventilation pulmonaire montre une diminution du signal (région hypo-intense) associée avec la présence de ces nanoparticules magnétiques tandis qu'aucune variation de signal est observée en imagerie systémique dans différents organes d'intérêt susceptibles d'accumuler le fer (rate, foie et reins). Injectées par voie intraveineuse, ces nanoparticules produisent une forte diminution (3 à 5 fois) du rapport contraste-sur-bruit (RCB) avec leur accumulation transitoire dans le foie et la rate.

Cette diminution du signal (en IRM pulmonaire après instillation et en IRM systémique après injection) disparait progressivement avec le temps pour être comparable au groupe contrôle. Ces observations peuvent être expliquées par une distribution plus homogène des nanoparticules avec le temps, à leur dégradation ou à leur encapsulation par des macrophages et ainsi un moindre contact avec l'hélium-3 dans le cas de l'imagerie de ventilation pulmonaire. Ces résultats d'imagerie ont été confirmés par des études *ex vivo* de dosage chimique de fer et d'histologie.

Cette étude illustre ainsi le potentiel de ce protocole d'imagerie IRM non-invasive hélium-3 et proton pour évaluer longitudinalement la distribution intra-pulmonaire des nanoparticules magnétiques après exposition respiratoire.

Dans le 2ème manuscrit de cette thèse, ce même protocole a été appliqué pour évaluer la biodistribution des NTC monofeuillets après exposition intrapulmonaire utilisant l'imagerie de résonance magnétique.

Des NTC bruts et ultra-purifiés ont été utilisés dans ce suivi de 2 semaines. Avant leur exposition aux animaux, leurs propriétés physico-chimiques ont été caractérisées par microscopie électronique et dosage chimique de 68 métaux qui montrent que les nanotubes bruts contiennent plus de 10% d'impureté de fer. Avec ces impuretés de fer, les nanotubes de carbone seront comparés à des agents de contraste négatifs qui produisent une diminution de signal en IRM.

Pour détecter et semi-quantifier cet effet, une nouvelle séquence radiale avec plusieurs temps d'écho (TE=40µs, 1ms, 2ms et 3ms) a été conçue.

Dans cette étude, la susceptibilité magnétique de l'impureté de fer (0,05mg) induit une diminution de T2* largement suffisante pour détecter la présence des nanotubes jusqu'à 48h post-instillation alors qu'aucune variation n'a été observée avec les nanotubes ultra-purifiés. Cet effet diminue progressivement avec le temps en raison de l'encapsulation des nanotubes confirmée en histopathologie par la présence de granulomes inflammatoires dans les poumons des rats instillés et/ou leur distribution plus homogène.

En IRM systémique, aucun changement de signal n'a été détecté après instillation dans les différents organes d'intérêt, par contre une accumulation transitoire surtout dans la rate a été observée après injection par voie intraveineuse, cet effet diminue progressivement avec le temps.

Les analyses d'histopathologie conduites à J14 ne montrent pas la présence des nanotubes dans les différents organes après instillation ou injection.

En raison de la concentration significative endogène de fer dans les différents organes comparée avec la dose injectée du fer, le dosage chimique ne permet pas d'évaluer la concentration de fer dans les différents organes, 2 semaines après exposition, avec un grand niveau de certitude.

La présence de nanotubes de carbone associés avec des impuretés de fer peut être détectée *in vivo* avec ce protocole d'IRM non-invasive. La détection *in vivo* des nanotubes à partir de leur propriété intrinsèque s'avèrent très utile dans le diagnostic de l'impact biologique des nanotubes que ce soit après exposition par voie pulmonaire ou pour des applications biomédicales, études qui feront l'objet des manuscrits 3 et 4 respectivement.

Dans le 3ème manuscrit de cette thèse, un suivi longitudinal de 3 mois a été réalisé pour détecter et évaluer l'impact biologique des NTC bruts suite à une instillation intratrachéal utilisant différentes techniques d'imagerie multimodale combinant l'IRM pulmonaire (hélium-3 et proton) non-invasive avec des techniques de microscopie optique et électronique.

Avec leur impureté intrinsèque de fer, l'imagerie de ventilation pulmonaire utilisant l'hélium-3 hyperpolarisé comme agent de contraste permet de détecter les nanotubes de carbone bruts grâce à un protocole non invasif sous respiration spontanée.

L'absence du signal du parenchyme pulmonaire en IRM proton favorise un rapport de contraste sur bruit suffisant pour détecter une sécrétion de fluide (région en hyper-signal) liée à la présence d'inflammation et œdème, ou déposition de fibre de collagène et d'atélectasie caractéristique de fibrose éventuelle suite à une exposition aux nanotubes de carbone.

L'histopathologie permet d'évaluer l'intégrité du tissu pulmonaire et de localiser la présence des agrégats de nanotubes de carbone et/ou la présence de leur effet pathologique (formation de granulomes inflammatoires).

Avec sa résolution nanométrique, la microscopie électronique à transmission (MET) permet de visualiser directement les nanotubes à l'échelle nanométrique, d'analyser les changements structuraux du système respiratoire et de détecter la présence des cellules inflammatoires produites avec la présence des nanotubes de carbone et finalement d'examiner la nature de leur interaction avec le poumon.

Les images de ventilation pulmonaire (IRM hélium-3) 24h après instillation montrent une diminution du signal proportionnelle à la dose exposée (0,1mg, 0,5mg et 1mg de SWCNT

bruts). Cet effet sur le signal n'est pas observé pour les autres temps d'investigation (J7, J30 et J90).

L'IRM proton pulmonaire à J30 indique la présence de petits nodules inflammatoires (pixels en hyper-signal dans le parenchyme pulmonaire) dans les groupes instillés avec les fortes doses de nanotubes (0,5 et 1mg). Les analyses d'histopathologie montrent la présence de granulomes multifocaux encapsulant les agrégats de nanotubes à partir de J7. L'absence d'effet sur le signal des images de ventilation pulmonaire à partir de J7 pourrait être due à l'encapsulation des nanotubes, leur distribution plus homogène ou l'incorporation de leur fer en ferritine ou hémosidérine.

Les images de microscopie électronique confirment l'accentuation de l'inflammation avec le temps et la dose de nanotubes instillés, observée en IRM pulmonaire proton, et se manifeste par une forte accumulation de fibre de collagène (CF) et montrent que les pneumocytes type II (ATII) et les macrophages alvéolaires (AM) forment le mécanisme de défense principal contre la nanotoxicité aigüe des nanotubes.

En résumé, l'IRM pulmonaire non-invasive proton et hélium-3, combinée avec des analyses *ex vivo* en microscopie optique et électronique permettent l'évaluation de l'impact biologique des nanotubes de carbone brutes. Plus généralement, cette approche pourra être appliquée pour d'autres types de nanoparticules pour lesquelles l'évaluation de l'impact fonctionnel est envisagée.

Dans le 4ème manuscrit de cette thèse, la distribution des NTC est suivie longitudinalement en IRM non-invasive après injection intraveineuse pour des perspectives d'applications en nanomédecine comme agents de contraste (diagnostic et thérapeutique) et leur impact biologique sur le métabolisme du foie est évalué *ex vivo* en RMN HR-MAS (haute résolution à l'angle magique), une technique prometteuse pour l'évaluation du métabolisme des organes cibles.

Avant administration *in vivo*, la caractérisation de la biodistribution et du profil pharmacologique des nanotubes de carbones devient cependant un pré-requis à leur utilisation. La détection des NTC en IRM dépend de l'effet de susceptibilité magnétique

induit par leur impureté de fer. Leur distribution dans les tissus et leur impact potentiel sur le métabolisme dépendent de leur structure, de leur enrobage et des impuretés métalliques.

Les analyses physicochimiques par dosage chimique de fer et spectroscopie Raman, faites pour les différentes solutions de NTC injectés par voie intraveineuse à un modèle de rat, montrent que les NTC bruts, purifiés et fonctionnalisés contiennent respectivement 10%, 2% et 0,7% d'impuretés de fer et possèdent des profils très similaires avec la présence des signatures Raman caractéristiques des NTC : RBM « radial breathing mode » correspondant aux vibrations atomiques des atomes de carbone permet de caractériser le diamètre des nanotubes et la bande G (déplacement Raman ~ 1600cm^{-1}) pourra être utilisée pour détecter les nanotubes de carbone en solution, dans le sang et les tissus car elle est insensible à l'environnement dans lequel les nanotubes sont présents.

Deux autres groupes: un injecté avec du Sinerem® (contrôle positif) et l'autre avec du sérum physiologique (contrôle négatif) ont été aussi inclus dans cette étude.

Une accumulation transitoire est détectée dans la rate (7 jours), foie (48h) et reins (5h) après injection des NTC bruts (effet de susceptibilité magnétique induit par leur impureté de fer) se manifestant par une diminution du signal qui graduellement disparaît avec le temps alors qu'aucun changement n'a été détecté avec les NTC purifiés et fonctionnalisés.

Les analyses conduites sur les organes d'intérêt (rate, foie, reins, poumons et sang) *ex vivo* en dosage chimique de fer, spectroscopie Raman et spectroscopie Raman amplifié (SERS « Surface Enhanced Raman Spectroscopy ») sur le sang, et l'histopathologie confirment les résultats IRM et ne permettent pas de détecter les NTC dans le sang (24h post-injection) et dans les différents organes (2 semaines post-injection).

Aucun signe de toxicité aiguë (comportement et perte de poids) n'est observé dans les différents groupes à travers les 2 semaines du suivi et les analyses en histopathologie ne montrent aucun signe de toxicité ou de changement dans l'intégrité des tissus.

Pour évaluer l'impact biologique après injection des NTC par voie intraveineuse, la spectroscopie RMN haute résolution a été utilisée *ex vivo* pour permettre d'obtenir un profil métabolique du foie des rats avec une haute résolution spectrale. Combinée avec des tests

de statistiques multi-variables (PCA « Principal Component Analysis » et PLS « Partial Least Square »), la technique HR-MAS permet de détecter des bio-marqueurs spécifiques de toxicité avec un éventuel changement du métabolisme.

Les tests PCA conduits sur les spectres RMN ne montrent aucune différence entre les échantillons analysés avec une absence de discrimination entre les différents groupes. L'analyse PLS conduit sur ces spectres en ajoutant une variable qui est dans notre cas le temps, permet le seul regroupement des spectres selon l'âge. Ainsi, aucune variation significative du métabolisme hépatique n'a pu être observée suite à une injection par voie intraveineuse des NTC ce qui montre, dans les conditions du suivi actuel, que ces nanotubes de carbone ne présentent pas une toxicité aiguë après injection.

Finalement, pour la cohérence de ce manuscrit de thèse, des études menées sur la caractérisation et l'application des nanoparticles d'oxyde de fer et sur l'optimisation d'un protocole d'imagerie de ventilation pulmonaire sont résumés brièvement en annexe à la fin de cette thèse.

Les travaux réalisés durant cette thèse ont fait l'objet de 8 publications (publiés ou soumises):

1. **Caractérisation des nanoparticules d'oxyde de fer (relaxivité):**

M. Hamoudeh, **A. Al Faraj**, E. Canet-Soulas, F. Bessueille, D. Léonard and H. Fessi: *Elaboration of PLLA-based superparamagnetic nanoparticles: Characterization, magnetic behaviour study and in vitro relaxivity evaluation*. **International Journal of Pharmaceutics**, Volume 338, Issues 1-2, 29 June **2007**, Pages 248-257

2. **Détection des nanoparticules d'oxyde de fer par IRM proton après administration dans le muscle:**

M. Hamoudeh, H. Fessi, H. Mehier, **A. Al Faraj**, E. Canet-Soulas: *Dirhenium decacarbonyl-loaded PLLA nanoparticles: Influence of neutron irradiation and preliminary in vivo administration by the TMT technique*. **International Journal of Pharmaceutics**, Volume 348, Issues 1-2, 4 February **2008**, Pages 125-136

3. **Contraste positive des nanoparticules d'oxyde de fer:**

M. Sigovan, M. Hamoudeh, **A. Al Faraj**, H. Fessi, E. Canet-Soulas: *Positive Contrast with Therapeutic Iron Nanoparticles at 4.7T*. **Submitted Manuscript.**

4. **Détection des nanoparticules d'oxyde de fer après instillation intrapulmonaire par IRM pulmonaire hélium-3 et systémique proton:**

A. Al Faraj, G. Lacroix, H. Alsaid, D. Elgrabi, V. Stupar, F. Robidel, S. Gaillard, E. Canet-Soulas, and Y. Crémillieux: *Longitudinal 3He and Proton imaging of magnetite biodistribution in a rat model of instilled nanoparticles.* **Magnetic Resonance in Medicine 59: 1298-1303 (2008).**

5. **Détection des nanotubes de carbone après instillation intrapulmonaire par IRM pulmonaire hélium-3 et systémique proton:**

A. Al Faraj, K. Cieslar, G. Lacroix, S. Gaillard, E. Canet-Soulas, and Y. Crémillieux: *In Vivo Imaging of Carbon Nanotube Biodistribution using Magnetic Resonance Imaging*. **Nano Letters 2009, 9 (3), 1023-1027.**

6. **Optimisation d'un protocole d'imagerie de ventilation pulmonaire:**

K. Cieslar, **A. Al Faraj**, V. Stupar, S. Gaillard, Y. Crémillieux: *HYPR method for increasing the performance of dynamic 3He MR ventilation imaging in rats*. **Submitted Manuscript.**

7. **Biodistribution et impact biologique des nanotubes de carbone après instillation intrapulmonaire:**

A. Al Faraj, A. Bessaad, K. Cieslar, S. Peyrol, G. Lacroix, E. Canet-Soulas, and Y. Crémillieux: *Single-walled carbon nanotubes detection and evaluation of impact using multimodality imaging techniques in a 3-months follow-up study*. **Submitted Manuscript**

8. **Biodistribution et impact biologique des nanotubes de carbone après injection intraveineuse:**

A. Al Faraj, F. Fauvelle, G. Lacroix, F. Lagarde, Y. Crémillieux, and E. Canet-Soulas: *In vivo biodistribution and biological impacts of injected carbon nanotubes.* **Submitted Manuscript**

Table of Abbreviations

Abbreviations	*Description*
θ	RF flip angle
µs	Microseconds
^{1}H	Proton
^{3}He	Helium-3
^{129}Xe	Xenon-129
AM	Alveolar macrophages
AS	Alveolar Space
AT II	Alveolar epithelial type II
BN	Brown-Norway
CE	Contrast Enhanced
CF	Collagen Fiber
CNR	Contrast-to-noise ratio
Co	Cobalt
CT	Computed Tomography
CV	Coefficient of variation
CVD	Chemical Vapor Deposition
D	Day
EF	Elastic Fiber
EO	Eosinophil
F	Functionalized
Fe	Iron
FOV	Field of View
G	Gram
GA	Glutaraldehyde
h	Hour
HES	Hematoxylin-Eosin-Saffron
HiPco	High Pressure Carbon monoxide
HP	Hyperpolarized
HPS	Hematoxylin-Phloxine-Saffron

HRMAS	High resolution Magic Angle Spinning
i.v.	Intravenous
ICP-MS	Inductively chemical plasma mass spectroscopy
ICP-OES	Inductively Coupled Plasma – Optical Emission Spectrometer
IR-FISP	Inversion Recovery - Fast Imaging with Steady State Precession
IT	Interstitium
ITI	Intratracheal instillation
LN	Lymph Nodes
M	Molar
MHz	Megahertz
Ml	Milliliter
MNP	Magnetic Nanoparticles
MRI	Magnetic Resonance Imaging
MRS	Magnetic Resonance Spectroscopy
ms	Milliseconds
MWCNT	Multi-walled Carbon Nanotube
NA	Numerical Aperture
Nex	Number of excitations
NFR	Nuclear Fast Red
Ni	Nickel
NIR	Near-Infrared
nm	Nanometer
NMR	Nuclear Magnetic Resonance
NP	Nanoparticles
P	Polarisation
PCA	Principal component analysis
PET	Positron emission tomography
PFA	Paraformaldehyde
PL	Photoluminescence

PLLA	Polyesters like poly(lactide)
PLS-DA	Partial least square – discriminant analysis
PMN	Polymorphonuclear neutrophils
ppm	Particle per million
RBC	Red Blood Cell
RBM	Radial Breathing Mode
$Re_2(CO)_{10}$	Dirhenium decacarbonyl
RES	Reticulo-endothelial system
RF	Radio Frequency
ROI	Region of Interest
SD	Sprague-Dawley
sd	Standard Deviation
SEM	Standard error of mean
SEOP	Spin exchange optical pumping
SI	Signal Intensity
SNR	Signal-to-noise ratio
SP	Super-purified
SWCNT	Single-walled Carbon Nanotube
T	Tesla
T1	Longitudinal relaxation time
T2	Transverse relaxation time
T2*	Transverse relaxation time, taking into account microscopic magnetic field inhomogeneities
TE	Echo time (The time between the RF pulse and the echo signal)
TEM	Transmission Electron Microscopy
TR	Repetition time (the time interval with which the RF pulse sequence is repeated)
USPIO	Ultra Small Particle Iron Oxide
w/w	Weight for weight
λ	wavelength of light

ORGANISATION OF THE THESIS

After a general introductory chapter, the results of this dissertation are presented in several manuscripts with a brief preface. The first section of the introductory chapter focuses on the novel and fascinating properties of nanoparticles and draw attention to the fact that the same properties that make them interesting in nanotechnology raise concerns about their potential biological impacts to respiratory system after accidental exposure and their potential use in nanomedicine especially for single-walled carbon nanotube (SWCNT). In the second section, the different techniques used to detect and assess the effect of carbon nanotubes are presented and the advantages and limitations of each technique are briefly summarized. However, a noninvasive imaging technique allowing longitudinal follow-up of SWCNT biodistribution after entering living species based on the intrinsic properties of carbon nanotubes is necessary and MRI can be the method of choice. In the third section of this chapter, after a general introduction of the basics of MRI, the attention is shifted to proton lung MRI and finally the principles and the practical implementation of hyperpolarized helium-3 (HP-^{3}He) lung MRI are highlighted.

The biodistribution of magnetite nanoparticles, the core of ultra-small particle iron oxide, was assessed in manuscript 1 to validate our approach for the detection of nanoparticles in the lung using HP-^{3}He MRI and in systemic organs using proton MRI in a longitudinal study.

The same approach was used in manuscript 2 to evaluate the biodistribution and biological impact of raw single-wall CNT (raw-SWCNT) and super-purified SWCNT (SP-SWCNT) *in vivo* based on their intrinsic properties.

In manuscript 3, *in vivo* detection of raw-SWCNT with HP-^{3}He MRI in a 3-months follow-up study was used in combination with proton lung MRI, optical and electron microscopy (multimodality imaging techniques) to evaluate their toxicological impact after lung exposition.

When administered *in vivo*, SWCNT biodistribution and pharmacological profile have to be fully characterized for safe biomedical applications. Tissue distribution of carbon

nanotubes and potential impact on metabolism depends both on nanotubes shape, coating and metallic impurities. In manuscript 4, different types of injected SWCNT were monitored *in vivo* using systemic MRI and the biological impacts on liver metabolism as an index of toxicity were assessed using *ex vivo* HRMAS (High resolution Magic Angle Spinning) ^{1}H NMR.

Manuscript 1 has been accepted for publication in *Magnetic Resonance in Medicine*, manuscript 2 in *Nano Letters* and manuscript 3 and 4 have been submitted for consideration.

Annex study 1 and 2 have been accepted for publication in *International Journal of Pharmaceutics* and annex study 3 and 4 have been submitted for consideration.

This thesis was performed at the University of Lyon 1 in Créatis-LRMN laboratory. Part of this work was conducted within the framework of an ANR project "RespiNTTox" (SEST program). Special thanks to the support from the European Union Marie Curie Research Training Network PHeLINet Contract Number MRTN-CT-2006-036002.

MR imaging protocols were conducted on a 2T Oxford magnet (HP-^{3}He MRI) and 4.7T Bruker magnet (Proton MRI), facilities of Créatis-LRMN at the University of Lyon1, Lyon.
Histopathological analyses were performed at INERIS, Verneuil-en-Halatte and TEM analyses at Cecil, Lyon.
Part of iron assays were carried out at INERIS (manuscript 1 to 3) and the other part (manuscript 4) at Laboratoire des Sciences Analytiques at the University of Lyon1, Lyon.
Raman spectroscopic analyses were conducted at CECOMO (Centre Commun de Microscopie Optique), of the Laboratoire de Physico-Chimie des Matériaux Luminescents at the University of Lyon1, Lyon.
HRMAS analyses were carried out at the laboratoire de RMN, CRSSA, La Tronche.

GENERAL INTRODUCTION

1. Nanoparticles: from nanotechnology to nanotoxicity

The last few years have witnessed the discovery, development and, in some cases, large-scale manufacturing and production of novel materials that lie within the nanometer scale. Nanotechnology is a rapidly advancing science research and technology development fuelled by the numerous revolutionary benefits and applications of engineered nanoparticles that captured the attention of researchers, governments and industries worldwide.

In general, these nanoparticles can be categorized into carbon-based materials such as fullerenes and carbon nanotubes and inorganic nanoparticles including the ones based on metal oxides (zinc oxide, iron oxide, titanium dioxide and cerium oxide etc), metals (gold, silver and iron) and quantum dots (cadmium sulfide and cadmium selenide) (figure1).

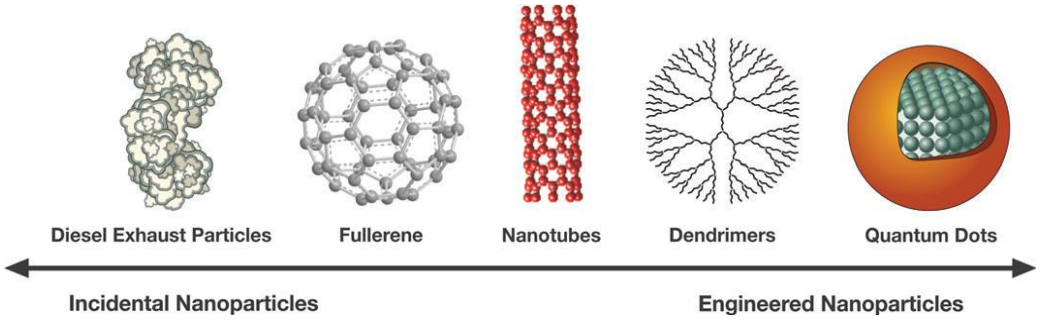

Figure1: Schematic illustration of incidental and engineered nanoparticles (1).

Nanoparticles possess unique electrical, mechanical, and thermal properties, with potential wide applications in the electronics, computer, aerospace, and other industries. They may be also used in an array of manufacturing sectors, including sporting goods, cosmetics, clothing, transistors, and biomedical products (2,3). The increase in nanomaterial manufacture and application will make likely the exposure to workers, consumers, medical staff members, and the general population.

While nanotechnology looms large with commercial promise and potential benefit, an equally large issue is the evaluation of potential effects on human and environmental health (1,4,5). A scientifically sound approach for developing safety evaluation strategies and

standards is therefore required (6). In addition, the disaster associated with the use of asbestos fibers in the past highlights the importance of identifying rapidly the potential hazards of new materials (7-9).

Epidemiological and toxicological studies have provided evidence that accidentally inhaled nanosize ultrafine particles can induce chronic or acute health damage (10-12). Due to their nanometric size, nanoparticles may have the ability to enter, translocate within, and damage living organisms. Some nanoparticles, depending on their composition and size, can produce irreversible damage to cells by oxidative stress or/and organelle injury.

The harmful effects of nanoparticles arise from the combination of various factors, two of which are particularly important: (a) the high surface area (figure2) and (b) the intrinsic toxicity of the material (13,14).

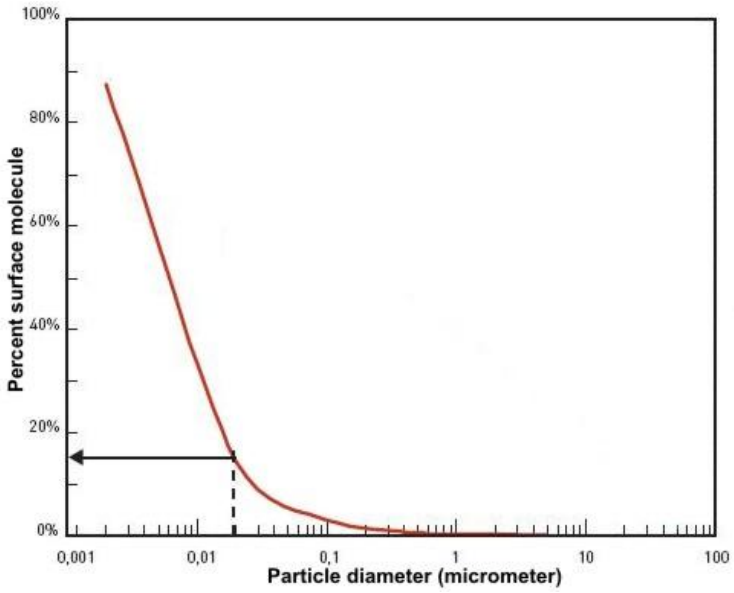

Figure2: Surface molecules as a function of particle size: Surface molecules increase exponentially when particle size decreases < 100 nm, reflecting the importance of surface area for increased chemical and biologic activity of NP (15).

a- CNT physicochemical properties:

Among different types of nanoparticles, carbon nanotubes with their unique and fascinating mechanical, electric, and thermal properties may be also uniquely toxic, thus necessitating evaluation of their biodistribution and nanotoxicity.

Since their discovery (16), they are the most promising engineered nanomaterials (17) used in different domains and for various industrial and commercial applications (18).

> *Carbon nanotubes are the best conductors of electricity of any organic molecule ever discovered with a current carrying capacity per unit area 100 times greater than copper. Carbon nanotube transistors can have a mobility that is 70 times higher than silicon. The thermal conductivity along the carbon nanotube is twice that of diamond and the tensile strength of carbon nanotubes is 100X greater than steel, but CNTs are less dense than aluminum. Nanotubes are the stiffest, strongest, and toughest molecule known.*
>
> *From: Carbon Nanotechnologies Inc. (CNI, Houston, TX)*
> *http://www.unidym.com/technology/cnt_property.html*

Carbon nanotubes consist of carbon atoms arranged in a series of condensed benzene rings rolled-up into a tubular structure (figure3). This novel nanomaterial belongs to the family of fullerenes, the third allotropic form of carbon along with graphite and diamond. CNT can be classified in two general categories, based on their structure: single-walled (SWCNT), which consist of a single layer of cylinder graphene and multi-walled (MWCNT), which contain several concentric graphene sheets. SWCNT have diameters ranging from 0.4 to 2.0 nm and lengths in the range of 20–1000 nm, while MWCNT are bigger objects with diameters in the range of 1.4–100 nm and lengths from 1 to several micrometers (19).

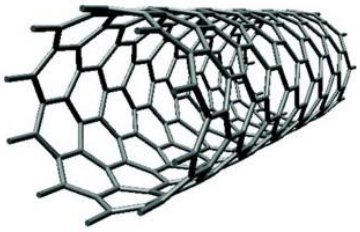

Figure3: Schematic illustration of a single-walled carbon nanotube structure (20).

Several methods exist today to synthesized carbon nanotubes, including chemical vapor deposition (CVD) (21), electric arc discharge (22), laser ablation (23), HiPco (high pressure carbon monoxide) (24), and surface mediated growth of vertically aligned tubes. The commercial large-scale manufacture of CNT mainly uses the HiPco and CVD methods (25).

When assessing biodistribution and biological impacts, carbon nanotubes impurities should be considerably taken into consideration. As-synthesized CNT prepared by various processes contain carbonaceous impurities, typically amorphous carbon and graphite nanoparticles, as well as particles of the transition-metal catalyst such as Fe, Ni, and Co, which can play a major role in their toxicity, biodistribution and properties.

Concern about the harmful effect of carbon nanotubes and more specifically in their single-walled form (SWCNT) may arise from three properties that are clearly associated with particles pathogenicity. With their nanometric size, SWCNT can be classified as NP and therefore could have more toxicity than larger sized particles. They are fiber shaped and so might behave like asbestos and other pathogenic fibers which have toxicity associated with their needle-like shape. SWCNT are essentially graphitic and so are expected to be biologically biopersistent (26).

Although several studies have reported potential toxic effects of carbon nanotubes on different types of cells *in vitro* (27-31), more studies about the biological impacts of SWCNT *in vivo* are required.

Schematically, there are two major situations in which people could be exposed to SWCNT: accidental respiratory exposure, essentially to an aerosol in the context of SWCNT production and manipulation; and exposure as a result of SWCNT use for biomedical purposes (32).

b- CNT pulmonary impacts:

With its large surface area in contact with the environment, the lung is a common target of many toxicants. The vast majority of published reports on the biological impacts of respiratory exposed CNT addressed the potential harmful effects of these nanomaterials by inducing the formation of epithelial granulomas and inflammatory responses with CNT biopersistence. (26,33-38).

However, the current knowledge about the determinants of lung toxicity of CNT required to make recommendations for its safe use is fragmentary, sometimes contradictory and still inconclusive.

Biologic and toxicological responses to CNT may vary by dose, way of exposition (inhalation, intratracheal instillation, pharyngeal aspiration …), type and physicochemical characteristics of CNT (SWCNT or MWCNT, pristine or functionalized, raw or purified …) (39).

Therefore, alternative ways to assess the biodistribution and biological impacts of inhaled CNT in the lung are highly needed especially for pristine non-purified SWCNT which may present major risk to exposed persons.

c- CNT as nanomedicine:

With their distinct architecture which allows them to selectively penetrate across biological barriers and their novel physicochemical properties in particular their propensity to functional modification, SWCNT hold promise for applications in nanomedicine field as

contrast agents or target delivery carriers designed to improve the distribution and performance of drug molecules (20,40,41).

The discovery of their impressive array of optical properties, including size-tunable emission (42), near infra-red (NIR, wavelength ~0.8-2 µm) (43) and high photo-stability (44) in addition to their intrinsic Raman scattering (45,46) opened the possibility to directly detect them at the single molecule level in living cells (47,48).

For their safe biomedical applications, SWCNT biodistribution, clearance, and pharmacological profiles have to be fully characterized before their introduction (49). Tissue distribution of carbon nanotubes and their potential impact on metabolism depends both on nanotubes shape, coating and metallic impurities (50).

Different methods have been proposed to improve SWCNT biocompatibility and reduce their toxicity for their use in nanomedicine.

In addition to purification, chemical modifications or functionalization of carbon nanotubes surfaces, required for their aqueous suspension, render them more hydrophilic which improve their biocompatibility profile and reduce the bundling/aggregation of individual tubes through van der Waals forces (51).

In general, different non-covalent and covalent modification strategies can be used. Non-covalent methods (association to surfactants, aromatic organic molecules, fluorophores, polymers, lipids, DNA, proteins and endohedral functionalization) preserve the pristine CNT structure while covalent modification (ends and defects, and sidewall functionalization) introduces structural perturbations (52,53).

2. SWCNT detection techniques:

Whether or not and how these materials are cleared from the body is unknown in many cases, because of the difficulties in long term *in vivo* tracking and monitoring of the materials.

To assess the biodistribution and biological impacts of SWCNT, different methods have been proposed to study their presence and effect after exposition to living species.

a- Optical Microscopy:

The oldest and simplest imaging method, optical or light microscopy is the most widely used technique to assess the integrity of tissue *ex vivo* and localize the presence of particles.

Biological samples for optical microscopy do not necessitate complex preparation procedures and therefore histopathological analysis was routinely performed in the vast majority of studies assessing the toxicity of carbon nanotubes.

Optical microscopy has however a fundamental limit in resolution (approximately 200 nm) that is affected both by the wavelength of light (λ), the refractive materials used to manufacture the objective lens and the numerical aperture (NA) of the objective lens.

With their van der Waals force attraction, carbon nanotubes bundle into ropes, which are further associated into loose aggregates and therefore they may be accessible for direct detection (figure4) using traditional light microscopy (38).

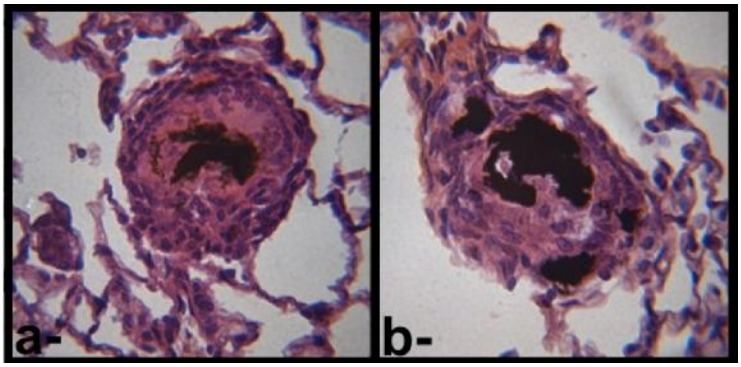

Figure4: Hematoxylin-Eosin-Saffron (HES) stained histological cuts of lung lobe (400× magnification) showing the presence of aggregated raw-SWCNT (a) and SP-SWCNT (b) that induce multifocal granulomas around the sites of SWCNT deposition (54).

The current advance in fluorescence optical microscopy using the phenomenon that certain material emits energy detectable as visible light when irradiated with the light of a specific wavelength was extensively applied to image carbon nanotubes using both confocal and near-field approaches (43,55,56).

However, chemical processing of nanoparticles may dramatically change their biological fate (biodistribution and nanotoxicity) as they are linked to visible-wavelength fluorophores which can resist enzymatic cleavage (i.e. sidewall functionalization with fluorescent markers).

Currently used fluorescent and radio-labels (57) for *in vivo* studies are useful for carbon nanotubes tracking over short periods of time (a few hours to a few days), but these labels may gradually dissociate from the materials or decay and lose activity over time. In addition, background auto-fluorescence emanating from superficial tissue layers restricts the sensitivity and the depth to which fluorescence imaging can be used (58).

Therefore, it is thus highly desirable to detect nanomaterials based on their intrinsic physical properties rather than relying on radiolabels or spectroscopic tags for indirect detection/measurement. The direct detection method may lead to a more accurate assessment of how nanomaterials behave *in vivo* in both short and long terms, i.e., during

the blood circulation stage and during time periods lasting several months after the exposure (59).

b- Near Infrared fluorescence:

It was newly discovered in 2002 (43) that single-walled carbon nanotubes possess an impressive array of optical properties, including size-tunable emission, near-infrared fluorescence, and high photo-stability very useful for single-particle tracking (60). Therefore, rather than fluorescent or radio-label SWCNT to allow their detection, SWCNT intrinsic optical qualities make them appealing as biological sensors and imaging contrast agents as their NIR photoluminescence (PL) lies within the "biological window" (700-1300 nm) where absorption, scattering, and auto-fluorescence by tissues, blood, and water are minimized (44,61).

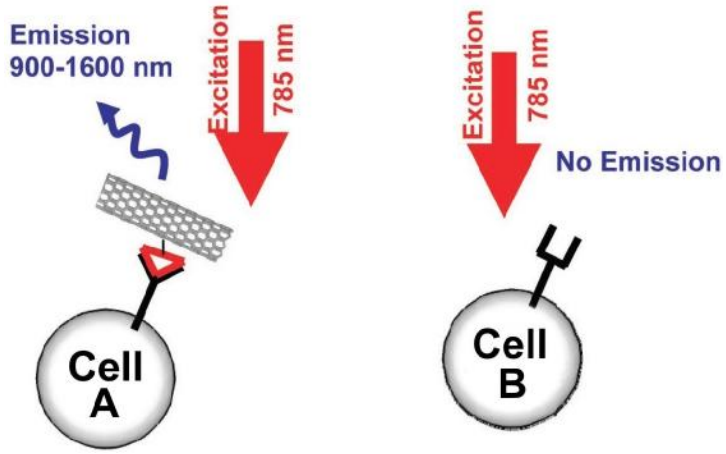

Figure: Schematic of NIR photoluminescence detection of SWCNT-cell complex (adapted from (48). SWCNT selectively bound to cell A surface receptor. NIR emission of SWCNT (900-1600nm) allows the detection of cell A.

However, NIR photoluminescence can be only observed when SWCNT are individually dispersed due to fluorescence quenching (62,63) and therefore this technique can be more readily used for biomedical perspectives of SWCNT where dispersion, functionalization and physiochemical properties can be controlled prior to administration.

Thus far, NIR imaging of the photoluminescence of SWCNT has been only demonstrated *in vitro* and *ex vivo* even though biological tissues allow for relatively high transmission and penetration of NIR light near 1 µm (48).

c- Raman Micro-spectroscopy:

Raman micro-spectroscopy recently applied to address various biomedical issues such as the early detection of cancers, monitoring of the effect of various agents on the skin, determination of atherosclerotic plaque composition, and rapid identification of pathogenic microorganisms (64,65) has been also presented as one of the main tools for SWCNT physicochemical characterization. It tells about the quality of the material, the microscopic structure of the tube, and phonon and electron quantum confinement (46,66).

In Raman scattering experiments (inelastic scattering of light) photons create or absorb phonons in the nanotubes and the change of energy is observed in the spectrum of the scattered light (figure5). Thus, Raman spectrum provides information about the nanotube phonons and because the electrons participate in the scattering process the spectrum also conveys information about the peculiar electronic structure of the nanotubes.

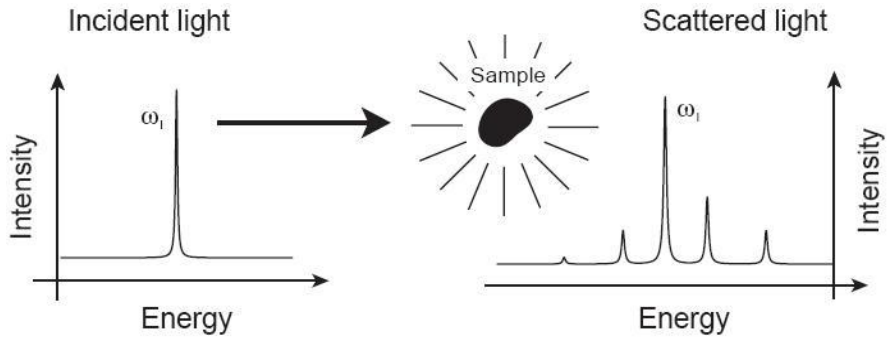

Figure5: Schematic illustration of the Raman experiment. A monochromatic beam of light impinges on a sample and the spectrum of the scattered light is recorded.

The Raman spectrum of carbon nanotubes consists primarily of two main features, the radial breathing mode (RBM) and the G-band (67) which present a good indication of complex formation and/or aggregate bundling (68) (figure6).

Unlike the resonance breathing model, the intensity of tangential graphene-like G band is relatively insensitive to the diameter and bundling of nanotubes (46,69).

The Raman signatures of SWCNT have therefore been used to directly probe the presence of nanotubes by providing specific intrinsic vibrational signatures of the chemical composition, molecular structure, and molecular interactions in cells and tissues (45).

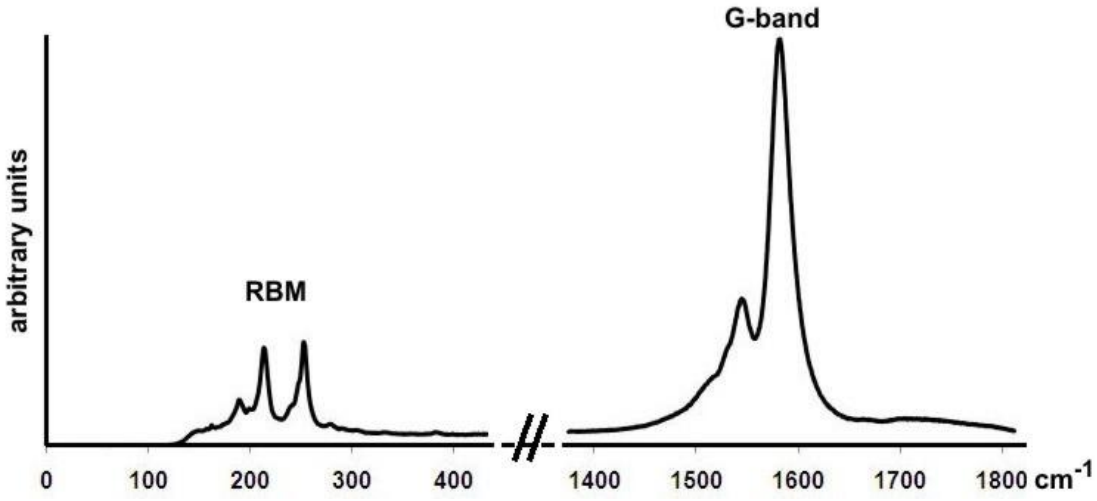

Figure6: Raman spectrum of a non-purified SWCNT excited with a 632.5 nm laser showing the characteristic RBM (a) and G-band (b) peaks.

It can differentiate the spectral fingerprint of many molecules, resulting in very high multiplexing capabilities (70). Narrow spectral features are easily separated from the broadband auto-fluorescence, because Raman is a scattering phenomenon as opposed to absorption/emission in fluorescence, and Raman active molecules are more photo-stable compared with fluorophores, which are rapidly photo-bleached (71).

The intrinsic Raman scattering intensity of SWCNT does not decay over time while being relatively insensitive to the types of non-covalent coatings and solution environments of SWCNT.

For these reasons, Raman spectroscopy presents an advantageous technique to sensitively detect (in paraffin-embedded tissues (50,72)) and quantify (in blood and organs samples suspension (57,59,72)) SWCNT presence in organs relying on their intrinsic physical properties.

d- Electron Microscopy:

One of the great challenges in directly detecting and assessing the interaction and effect of SWCNT within tissues or single cells at sub-cellular scale is their nanometric size.

With its high resolution that lies in the order of carbon nanotubes dimension, transmission electron microscopy was at the origin of carbon nanotubes discovery in 1991 in their multi-walled form (16) and in 1993 in their single-walled form (73) and it is still the technique of choice used by researchers to physically characterize carbon nanotubes production, purification, dispersion and modifications (74-77) (figure7).

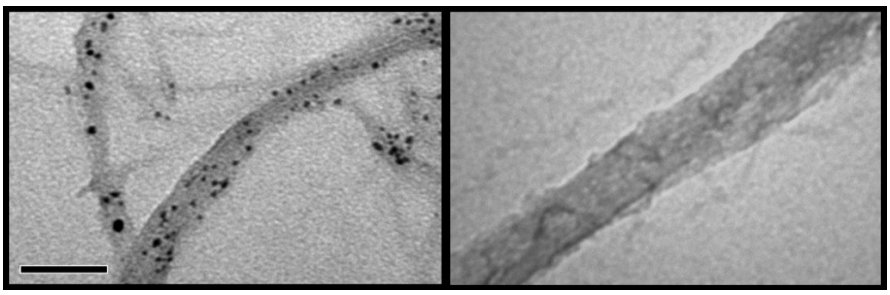

Figure7: TEM images showing the presence of impurities (black dots) in raw SWCNT bundles (left) and their absence in super-purified SWCNT bundles (right). Scale bar represents 50 nm (54).

TEM contribution for the toxicological evaluation of ultrafine and fibrous particles was intensively studied in the past to detect particles intracellular localization and to assess the morphology of tissue or cell samples (78-81). Similarly, transmission electron microscopy provides an ideal tool to analyze SWCNT-related structural changes, to reveal their localization within tissues and cells and to investigate the nature of interactions within biological environment after exposition living species to SWCNT. The data concerned with the previous SWCNT-like nanoparticles (i.e. asbestos) can be very useful for the evaluation and comparison with SWCNT investigations.

A major limitation for using TEM in biological assay is the stringent requirement of samples that can be examined. A prerequisite for transmission electron microscopy is that all cells or tissues entering the microscope have to be fixed in order to preserve them as close to the living state as possible.

Currently, there are two major approaches to fix biological samples: chemical and physical fixation (figure8).

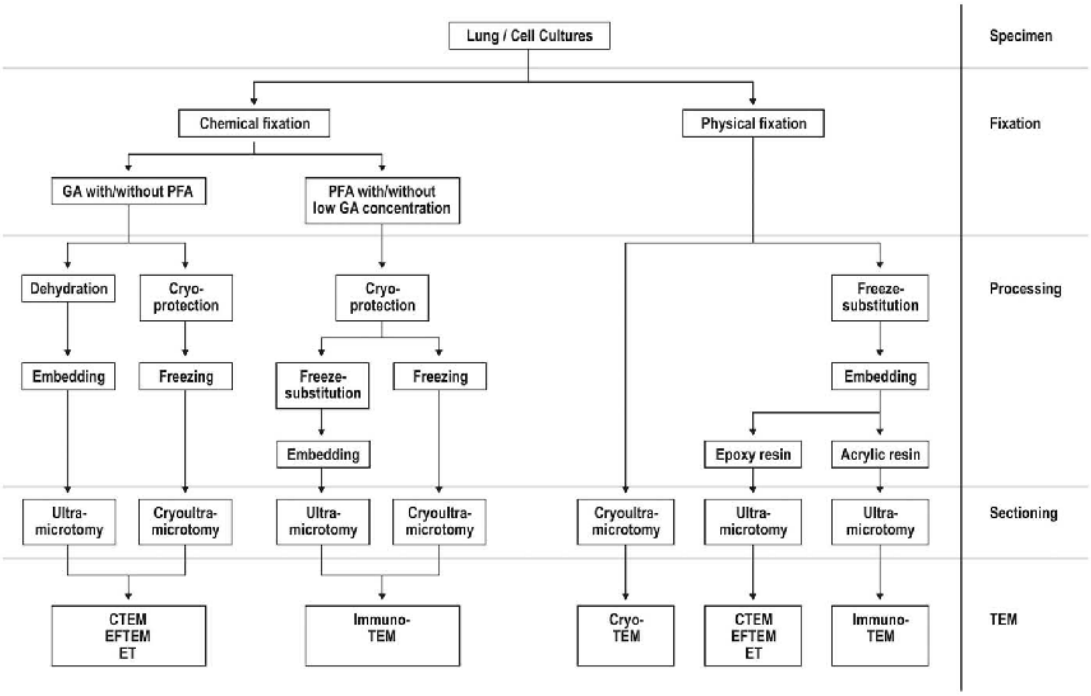

Figure8: Diagram showing the different possible procedure of lung/cell cultures preparation and their impact for the different TEM techniques (79).

GA = glutaraldehyde; PFA = paraformaldehyde; CTEM = conventional TEM; EFTEM = energy-filtered TEM; ET = electron tomography.

During chemical fixation (most adapted for lung tissue), preservation of samples with glutaraldehyde which covalently cross links proteins and osmium tetroxide which stabilizes lipid bilayers and proteins, allows the specimen to be further dehydrated and permeated with a resin. The specimen in this form can be sliced with an ultra-microtome to create thin

sections (less than 100 nm) that are free of water and volatile substances and allow the electrons to penetrate the specimens.

In the precedent section, the most widely used or advantageous techniques to assess the biodistribution and biological impacts of carbon nanotubes were briefly summarized. Histopathological analyses were routinely used but are limited to aggregated-SWCNT. Electron microscopy offers high spatial resolution imaging of SWCNT but is limited to slices of tissues that have been fixed. Fluorescent and radio-labels used for in vivo detection (i.e PET imaging) may gradually dissociate from the materials or decay and lose activity over time and chemical processing of SWCNT may have effects on their biological fate. Thus, it is highly desirable to detect nanomaterials based on their intrinsic physical properties: the intrinsic Raman scattering intensity of SWCNT and their intrinsic near infrared (NIR) photoluminescence which allow their specific and direct detection. However these techniques are more adapted to in vitro and ex vivo investigations. Therefore, development of a noninvasive imaging technique which allow longitudinal follow-up of SWCNT effect based on their intrinsic properties is highly desirable. When noninvasive and longitudinal imaging investigations are considered, Magnetic Resonance Imaging (MRI) could be a method of choice.

3. Magnetic Resonance Imaging:

Based on the principles of nuclear magnetic resonance (NMR), a spectroscopic technique used by scientists to obtain microscopic chemical and physical information about molecules, Magnetic Resonance Imaging has become the primary technique throughout the body in the routine diagnosis of many disease processes.

For comprehensive description of the NMR technology the reader is referred to the NMR handbooks by Callaghan (82) and Haacke (83) and the review by Wehrli (84) and Wright (85).

a. Conventional MRI Basics:

Conventional or standard MRI relies on the magnetic moments of the protons that make up the nuclei of the hydrogen atoms in water. Protons can be enticed to oscillate by placing them in a magnetic field and tickling them with a radio frequency pulse. In a magnetic field, protons magnetic moments can either line up with the magnetic field or against it. A radiofrequency pulse applied to the sample via the same coil used for detection torques the magnetization away from the magnetic field axis and causes them to wobble around this axis at a frequency that is precisely proportional to the strength of the magnetic field and their own magnetic moment. This wobbling is called precession. For example, in a 4.7 Tesla MRI scanner, the proton precession frequency is about 200 MHz. The flux from the spinning nuclear moments is then picked up by the coil, amplified, and digitized. In the case of water protons, after a few hundred milliseconds of precessing, proton's magnetic moments return back to being aligned with the magnetic field and they can be pulsed and detected again.

To generate a magnetic resonance image rather than a single-frequency signal, a linear magnetic field gradient has to be applied during signal acquisition. The gradient reduces the magnetic field strength at one end of the sample and increases it at the other end. This makes the nuclei at one end of the sample precess more slowly than at the other because

precession frequency is proportional to magnetic field strength. The detected signal is then broken down by its frequency components whose amplitudes represent a 1-dimensional image of the sample. This approach of using magnetic field gradients to encode the spatial distribution of nuclei can be readily extended to acquire images in 3 dimensions.

The role of the magnetic field in imaging is to bring enough order to the system of nuclei to make them detectable. To see an MRI signal, an imbalance must exist in the number of magnetic moments starting out aligned versus anti-aligned with the magnetic field. These two populations have precession signals of opposite signs and would cancel each other exactly if present in equal numbers. The interaction of the nuclei with the magnetic field makes it slightly more energetically favorable for them to be aligned rather than anti-aligned with the field. This imbalance in the population of nuclei is called polarization and is defined as:

$P = \frac{\left| N_{\uparrow} - N_{\downarrow} \right|}{\left| N_{\uparrow} + N_{\downarrow} \right|}$; *where $N_{\uparrow}$ is the number of aligned nuclei and $N_{\downarrow}$ is the number of anti-aligned nuclei.*

However, even in large magnetic fields, the tiny energy difference between states gives a polarization only few parts per million. Thus, most of the magnetic moments still cancel one another. The strength of the MRI signal coming from a given three dimensional pixel element (voxel) in the image is:

$S_{MRI} \alpha \mu \times \omega \times P \times \rho \times V_{vox}$; where μ is the nuclear magnetic moments, ω is their precession frequency around the magnetic field, P is their polarization, ρ is their density, and V_{vox} is the voxel volume.

Both precession frequency ω and polarization P increase linearly with magnetic field strength. The intuitive dependence on density also explains why water is the favored imaging source. The concentration of hydrogen nuclei [1H] is 110 M, sufficient to provide ample signal despite relatively low nuclear polarization in even the largest magnetic fields (86).

MRI has particular advantages over competing noninvasive modalities in that it is noninvasive, using non-ionising radiation, and has a high soft-tissue resolution and discrimination in any imaging plane. It may also provide both morphological and functional information of the entire body.

b. Proton Lung MRI:

However, lung parenchyma still remains one of the most difficult tissue to be imaged using MRI because of the low density of air-filled lung parenchyma, resulting in low proton density and weak NMR signal intensity (SI), the important motion artifacts due to physiological displacements (cardiac and respiratory motions) and because of the susceptibility effects induced by multiple air and tissue interfaces which cause many local gradients responsible for very short T2 of T2* relaxation times (87).

Different strategies have been proposed to minimize motion artifacts. Image acquisition during breath hold or using respiratory gating and/or EKG triggering procedures (88) results in reduced motion artifacts and a fixed position of the diaphragm and the cardiac cavities during image acquisition (89).

However, breath hold is not adapted to all patients (i.e young children) and cannot be performed for animal studies (90) and cardiac and ventilation triggered techniques do not allow predetermined and constant repetition time of the sequence, resulting in variable image contrast and acquisition time might be relatively long for routine use (91).

As presented by Beckmann and colleagues, image averaging technique combined to short echo time present a very good alternative to obtain a very good quality images (figure9) with reduced motions artifacts in proton lung MRI (87,92). This method interferes minimally with the well-being of the animals, because neither respiratory nor electrocardiogram triggering is necessary, and they are allowed to respire freely during data collection (93).

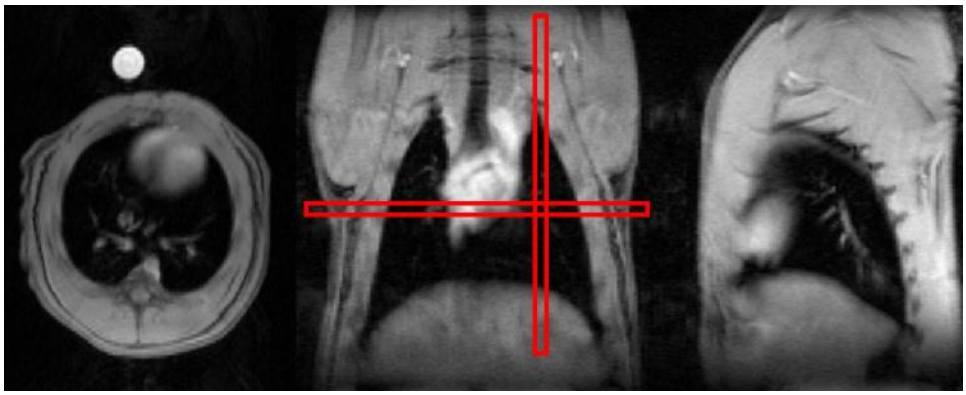

Figure9: Proton lung MR images of a Brown-Norway rat (a: axial, b: coronal and c: sagittal slices) acquired using a gradient echo sequence (TR/TE=7.9/2.1-ms; Nex=50, total acquisition time=50seconds) on a 4.7T-magnet. Neither cardiac nor respiration triggering was applied.

The absence of lung parenchyma MR proton signal in combination with a background free of artifacts provides a high contrast-to-noise ratio for the detection of fluid secretion related to inflammation and edema (92,94) or to collagen deposition and atelectasis (hallmarks of fibrosis) (95).

To obtain a higher NMR signal from the lung parenchyma several approaches have been proposed. One of the approaches consists of the inhalation of paramagnetic contrast agent such as gadolinium chelates aerosol (96) or molecular oxygen gas (97) in order to increase the relaxivity of protons and thus the recovery rate of the NMR signal.

Another novel approach is based on the use of ultra-short sequence (i.e radial sequence) with an echo time of less than 500 µs (98,99) which allow obtaining a higher signal from lung parenchyma.

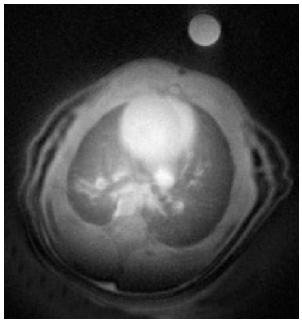

Figure10: Proton lung MR image of a Brown-Norway rat acquired in axial slice using a radial sequence with an ultra-short echo time (TE=450µs) on a 4.7T-magnet. Neither cardiac nor respiration triggering was applied.

Compared to conventional water proton imaging, MRI of gases is inherently limited by the much lower spin density (typically a three orders of magnitude drop in spin density).

Despite this low MR sensitivity, MR ventilation imaging using gaseous fluorinated compounds have been demonstrated previously (100) but this technique suffers from poor spatial resolution and long acquisition times, on the order of 30 min per image or longer (101).

However, with the introduction of hyperpolarized (HP) gases (i.e. ^{3}He, ^{129}Xe) acting as contrast agents that diffuse rapidly to fill the airspaces of the lungs and allow visualization and measurement of the ventilated airways and alveolar spaces, pulmonary ventilation imaging became possible with a high spatial and temporal resolution (102).

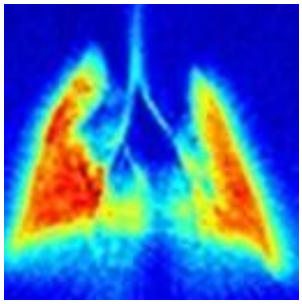

Figure11: Color chart of ^{3}He ventilation image of a rat lung acquired using a radial sequence with 40µs echo time on a 2T magnet.

c. Hyperpolarized gases (^{3}He and ^{129}Xe):

HP gases provide large MR signal created outside of the principal magnetic field of the MR scanner with the use of optical polarization methods. These polarization methods are capable of generating polarization levels ~10^5 times greater than thermal equilibrium for these nuclei (103).

For a detailed description of the principles, design and practical implementation of the optical pumping laser polarization techniques, the reader is referred to the reviews by Goodson (104) and Moller (105).

A polarization system based on spin-exchange optical pumping technique was developed in our laboratory (figure12) to polarized helium-3 gas (106). A quantity of ~1.2 liter of gas with end polarization levels in the order of 20% was obtained after approximately 24 hours of polarization time.

Figure12: HP gases polarization system based on the spin-exchange optical pumping technique (Creatis-LRMN, Lyon, France).

Despite the fact that ^{129}Xe has a much higher natural abundance and is more widely available, ^{3}He has been so far the most widely used gas for lung MRI animal research with it larger gyromagnetic ratio (γ^{3He}=0.76 γ^{1H} vs. γ^{129}Xe=0.28 γ^{1H}) lending to a higher NMR signal-to-noise ratio (SNR) (107).

However, ^{3}He has a larger diffusion coefficient than ^{129}Xe, meaning the MRI signal is more sensitive to attenuation by diffusion in applied gradients. There are also certain

physiological issues relating to choice of HP noble gas; helium is virtually insoluble, meaning it is confined to the lung air-space during a breath-hold. Xenon is, however, highly soluble and can indeed be used to study gas exchange by perfusion. Once dissolved in the blood, its lypophilic nature means that xenon also has an anesthetic effect (108). The use of ^{129}Xe has much potential for studying gas exchange physiology and perfusion mechanisms, as xenon can be localized in the various phases of lung-to-blood transportation using spectroscopic methods (107).

d. HP-^{3}He Lung MRI:

Small animal imaging of HP-^{3}He is predictably more challenging with their higher cardiac and respiratory rates leading to high demands on the sequence timing than clinical imaging. Furthermore, as mentioned before, human patients can be asked to take a deep breath of gas from a bag and hold for 10 or 15 seconds while imaging is performed, but not so with a rodent. In addition to motion degradation of image quality, blurring and signal attenuation can occur because of the high diffusivity of ^{3}He gas, creating an additional obstacle for resolving small airways and related structures. Thus, specialized MRI image acquisition strategies with specific pulse sequences (small flip angle and very short echo time) have been implemented specifically for high-quality imaging of hyperpolarized gases in small animals (109).

Hyperpolarized ^{3}He can be introduced into the animal lungs using either tracheal intubation or invasive tracheotomy. Ideally, the investigation of lung function changes in small animals requires a noninvasive imaging protocol with minimal interference with the physio-pathological conditions of the animals and the possibility of performing multiple and longitudinal imaging studies. Furthermore, the ventilation imaging protocol is expected to yield relevant quantitative parameters related to the animal's lung function (110).

A completely noninvasive HP-^{3}He lung ventilation imaging protocol was implemented in our laboratory for small animals. During acquisition, animals were allowed to breathe freely a mixture of air and ^{3}He from a mask and a gas reservoir fitted to their heads

(figure13). A retrospective cine image reconstruction with a sliding windows approach (111) for dynamic and anatomical imaging was used. Images can therefore be reconstructed using a gridding algorithm (112) running under IDL software (Research System Inc., Boulder, CO) at the end of inspiration to visualize the largest fraction of ventilated alveolar spaces (figure14).

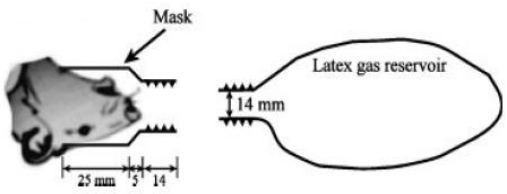

Figure13: Outline of the noninvasive HP-^{3}He breathing system designed for small animal ventilation imaging (110).

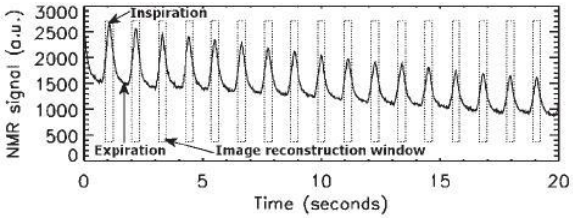

Figure14: View-to-view ^{3}He NMR signal amplitude evolution during the animal ventilation protocol (110).

References:

1. Stern ST, McNeil SE. Nanotechnology safety concerns revisited. Toxicol Sci 2008;101(1):4-21.

2. McCauley LA, McCauley RD. Nanotechnology: are occupational health nurses ready? Aaohn J 2005;53(12):517-521.

3. Staggers N, McCasky T, Brazelton N, Kennedy R. Nanotechnology: the coming revolution and its implications for consumers, clinicians, and informatics. Nursing outlook 2008;56(5):268-274.

4. Ju-Nam Y, Lead JR. Manufactured nanoparticles: an overview of their chemistry, interactions and potential environmental implications. The Science of the total environment 2008;400(1-3):396-414.

5. Bouwmeester H, Dekkers S, Noordam MY, Hagens WI, Bulder AS, de Heer C, ten Voorde SE, Wijnhoven SW, Marvin HJ, Sips AJ. Review of health safety aspects of nanotechnologies in food production. Regul Toxicol Pharmacol 2009;53(1):52-62.

6. Schulte PA, Salamanca-Buentello F. Ethical and scientific issues of nanotechnology in the workplace. Environmental health perspectives 2007;115(1):5-12.

7. Mossman BT, Bignon J, Corn M, Seaton A, Gee JB. Asbestos: scientific developments and implications for public policy. Science (New York, NY 1990;247(4940):294-301.

8. Rai A, Gupta TN. Asbestos an important insulating material; its varieties, properties and safe uses. Indian journal of environmental health 2002;44(3):220-224.

9. Castleman B. Asbestos products, hazards, and regulation. Int J Health Serv 2006;36(2):295-307.

10. Kreyling WG, Semmler-Behnke M, Möller W. Ultrafine Particle-Lung Interactions: Does Size Matter? Journal of Aerosol Medicine 2006;19(1):74-83.

11. Englert N. Fine particles and human health--a review of epidemiological studies. Toxicology letters 2004;149(1-3):235-242.

12. Schlesinger RB, Kunzli N, Hidy GM, Gotschi T, Jerrett M. The health relevance of ambient particulate matter characteristics: coherence of toxicological and epidemiological inferences. Inhalation toxicology 2006;18(2):95-125.

13. Donaldson K, Tran CL. Inflammation caused by particles and fibers. Inhalation toxicology 2002;14(1):5-27.

14. Donaldson K, Stone V, Tran CL, Kreyling W, Borm PJ. Nanotoxicology. Occupational and environmental medicine 2004;61(9):727-728.

15. Oberdorster G, Oberdorster E, Oberdorster J. Nanotoxicology: an emerging discipline evolving from studies of ultrafine particles. Environmental health perspectives 2005;113(7):823-839.

16. Iijima S. Helical microtubules of graphitic carbon. Nature 1991;354(6348):56-58.

17. Giles J. Top five in physics. Nature 2006;441(7091):265.

18. Polizu S, Savadogo O, Poulin P, Yahia L. Applications of carbon nanotubes-based biomaterials in biomedical nanotechnology. Journal of nanoscience and nanotechnology 2006;6(7):1883-1904.

19. Lin Y, Taylor S, Li H, Fernando KAS, Qu L, Wang W, Gu L, Zhou B, Sun Y-P. Advances toward bioapplications of carbon nanotubes. Journal of Materials Chemistry 2004;14(4):527-541.

20. Foldvari M, Bagonluri M. Carbon nanotubes as functional excipients for nanomedicines: I. Pharmaceutical properties. Nanomedicine 2008;4(3):173-182.

21. Cassell AM, Raymakers JA, Kong J, Dai H. Large Scale CVD Synthesis of Single-Walled Carbon Nanotubes. The Journal of Physical Chemistry B 1999;103(31):6484-6492.

22. Journet C, Maser WK, Bernier P, Loiseau A, de la Chapelle ML, Lefrant S, Deniard P, Lee R, Fischer JE. Large-scale production of single-walled carbon nanotubes by the electric-arc technique. Nature 1997;388(6644):756-758.

23. Thess A, Lee R, Nikolaev P, Dai H, Petit P, Robert J, Xu C, Lee YH, Kim SG, Rinzler AG, Colbert DT, Scuseria GE, Tomanek D, Fischer JE, Smalley RE. Crystalline Ropes of Metallic Carbon Nanotubes. Science (New York, NY 1996;273(5274):483-487.

24. Nikolaev P, Bronikowski MJ, Bradley RK, Rohmund F, Colbert DT, Smith KA, Smalley RE. Gas-phase catalytic growth of single-walled carbon nanotubes from carbon monoxide. Chemical Physics Letters 1999;313(1-2):91-97.

25. Ge C, Lao F, Li W, Li Y, Chen C, Qiu Y, Mao X, Li B, Chai Z, Zhao Y. Quantitative Analysis of Metal Impurities in Carbon Nanotubes: Efficacy of Different Pretreatment Protocols for ICPMS Spectroscopy. Analytical chemistry 2008;80(24):9426-9434.

26. Donaldson K, Aitken R, Tran L, Stone V, Duffin R, Forrest G, Alexander A. Carbon nanotubes: a review of their properties in relation to pulmonary toxicology and workplace safety. Toxicol Sci 2006;92(1):5-22.

27. Cui D, Tian F, Ozkan CS, Wang M, Gao H. Effect of single wall carbon nanotubes on human HEK293 cells. Toxicology letters 2005;155(1):73-85.

28. Jia G, Wang H, Yan L, Wang X, Pei R, Yan T, Zhao Y, Guo X. Cytotoxicity of carbon nanomaterials: single-wall nanotube, multi-wall nanotube, and fullerene. Environmental science & technology 2005;39(5):1378-1383.

29. Tian F, Cui D, Schwarz H, Estrada GG, Kobayashi H. Cytotoxicity of single-wall carbon nanotubes on human fibroblasts. Toxicol In Vitro 2006;20(7):1202-1212.

30. Monteiro-Riviere NA, Nemanich RJ, Inman AO, Wang YY, Riviere JE. Multi-walled carbon nanotube interactions with human epidermal keratinocytes. Toxicology letters 2005;155(3):377-384.

31. Shvedova AA, Castranova V, Kisin ER, Schwegler-Berry D, Murray AR, Gandelsman VZ, Maynard A, Baron P. Exposure to carbon nanotube material: assessment of nanotube cytotoxicity using human keratinocyte cells. Journal of toxicology and environmental health 2003;66(20):1909-1926.

32. Boczkowski J, Lanone S. Potential uses of carbon nanotubes in the medical field: how worried should patients be? Nanomedicine (London, England) 2007;2(4):407-410.

33. Liu A, Sun K, Yang J, Zhao D. Toxicological effects of multi-wall carbon nanotubes in rats. Journal of Nanoparticle Research 2008;10(8):1303-1307.

34. Helland A, Wick P, Koehler A, Schmid K, Som C. Reviewing the environmental and human health knowledge base of carbon nanotubes. Environmental health perspectives 2007;115(8):1125-1131.

35. Warheit DB, Laurence BR, Reed KL, Roach DH, Reynolds GA, Webb TR. Comparative pulmonary toxicity assessment of single-wall carbon nanotubes in rats. Toxicol Sci 2004;77(1):117-125.

36. Muller J, Huaux F, Moreau N, Misson P, Heilier JF, Delos M, Arras M, Fonseca A, Nagy JB, Lison D. Respiratory toxicity of multi-wall carbon nanotubes. Toxicology and applied pharmacology 2005;207(3):221-231.

37. Lam CW, James JT, McCluskey R, Hunter RL. Pulmonary toxicity of single-wall carbon nanotubes in mice 7 and 90 days after intratracheal instillation. Toxicol Sci 2004;77(1):126-134.

38. Lam CW, James JT, McCluskey R, Arepalli S, Hunter RL. A review of carbon nanotube toxicity and assessment of potential occupational and environmental health risks. Critical reviews in toxicology 2006;36(3):189-217.

39. Muller J, Huaux F, Lison D. Respiratory toxicity of carbon nanotubes: How worried should we be? Carbon 2006;44(6):1048-1056.

40. Mehra NK, Jain AK, Lodhi N, Raj R, Dubey V, Mishra D, Nahar M, Jain NK. Challenges in the use of carbon nanotubes for biomedical applications. Critical reviews in therapeutic drug carrier systems 2008;25(2):169-206.

41. Foldvari M, Bagonluri M. Carbon nanotubes as functional excipients for nanomedicines: II. Drug delivery and biocompatibility issues. Nanomedicine 2008;4(3):183-200.

42. Bachilo SM, Strano MS, Kittrell C, Hauge RH, Smalley RE, Weisman RB. Structure-assigned optical spectra of single-walled carbon nanotubes. Science (New York, NY 2002;298(5602):2361-2366.

43. O'Connell MJ, Bachilo SM, Huffman CB, Moore VC, Strano MS, Haroz EH, Rialon KL, Boul PJ, Noon WH, Kittrell C, Ma J, Hauge RH, Weisman RB, Smalley RE. Band gap fluorescence from individual single-walled carbon nanotubes. Science (New York, NY 2002;297(5581):593-596.

44. D. A. Heller SBTEEMSS. Single-Walled Carbon Nanotube Spectroscopy in Live Cells: Towards Long-Term Labels and Optical Sensors. Advanced Materials 2005;17(23):2793-2799.

45. Freudiger CW, Min W, Saar BG, Lu S, Holtom GR, He C, Tsai JC, Kang JX, Xie XS. Label-free biomedical imaging with high sensitivity by stimulated Raman scattering microscopy. Science (New York, NY 2008;322(5909):1857-1861.

46. Rao AM, Richter E, Bandow S, Chase B, Eklund PC, Williams KA, Fang S, Subbaswamy KR, Menon M, Thess A, Smalley RE, Dresselhaus G, Dresselhaus MS. Diameter-Selective Raman Scattering from Vibrational Modes in Carbon Nanotubes. Science (New York, NY 1997;275(5297):187-191.

47. Cherukuri P, Bachilo SM, Litovsky SH, Weisman RB. Near-infrared fluorescence microscopy of single-walled carbon nanotubes in phagocytic cells. Journal of the American Chemical Society 2004;126(48):15638-15639.

48. Welsher K, Liu Z, Daranciang D, Dai H. Selective probing and imaging of cells with single walled carbon nanotubes as near-infrared fluorescent molecules. Nano letters 2008;8(2):586-590.

49. Prato M, Kostarelos K, Bianco A. Functionalized carbon nanotubes in drug design and discovery. Accounts of chemical research 2008;41(1):60-68.

50. Schipper ML, Nakayama-Ratchford N, Davis CR, Kam NW, Chu P, Liu Z, Sun X, Dai H, Gambhir SS. A pilot toxicology study of single-walled carbon nanotubes in a small sample of mice. Nature nanotechnology 2008;3(4):216-221.

51. Lacerda L, Bianco A, Prato M, Kostarelos K. Carbon nanotubes as nanomedicines: from toxicology to pharmacology. Advanced drug delivery reviews 2006;58(14):1460-1470.

52. Hirsch A, Vostrowsky O. Functionalization of Carbon Nanotubes. Functional Molecular Nanostructures; 2005. p 193-237.

53. S. Banerjee TH-BSSW. Covalent Surface Chemistry of Single-Walled Carbon Nanotubes. Advanced Materials 2005;17(1):17-29.

54. Al Faraj A, Cieslar K, Lacroix G, Gaillard S, Canet-Soulas E, Crémillieux Y. In Vivo Imaging of Carbon Nanotube Biodistribution Using Magnetic Resonance Imaging. Nano letters 2009;9(3):1023-1027.

55. Tsyboulski DA, Bachilo SM, Weisman RB. Versatile visualization of individual single-walled carbon nanotubes with near-infrared fluorescence microscopy. Nano letters 2005;5(5):975-979.

56. Chaudhary S, Kim JH, Singh KV, Ozkan M. Fluorescence Microscopy Visualization of Single-Walled Carbon Nanotubes Using Semiconductor Nanocrystals. Nano letters 2004;4(12):2415-2419.

57. Liu Z, Cai W, He L, Nakayama N, Chen K, Sun X, Chen X, Dai H. In vivo biodistribution and highly efficient tumour targeting of carbon nanotubes in mice. Nature nanotechnology 2007;2(1):47-52.

58. Faulds K, Barbagallo RP, Keer JT, Smith WE, Graham D. SERRS as a more sensitive technique for the detection of labelled oligonucleotides compared to fluorescence. The Analyst 2004;129(7):567-568.

59. Liu Z, Davis C, Cai W, He L, Chen X, Dai H. Circulation and long-term fate of functionalized, biocompatible single-walled carbon nanotubes in mice probed by Raman spectroscopy. Proceedings of the National Academy of Sciences of the United States of America 2008;105(5):1410-1415.

60. Carlson LJ, Maccagnano SE, Zheng M, Silcox J, Krauss TD. Fluorescence efficiency of individual carbon nanotubes. Nano letters 2007;7(12):3698-3703.

61. Wray S, Cope M, Delpy DT, Wyatt JS, Reynolds EO. Characterization of the near infrared absorption spectra of cytochrome aa3 and haemoglobin for the non-invasive monitoring of cerebral oxygenation. Biochimica et biophysica acta 1988;933(1):184-192.

62. Strano MS, Moore VC, Miller MK, Allen MJ, Haroz EH, Kittrell C, Hauge RH, Smalley RE. The role of surfactant adsorption during ultrasonication in the dispersion of single-walled carbon nanotubes. Journal of nanoscience and nanotechnology 2003;3(1-2):81-86.

63. Moore VC, Strano MS, Haroz EH, Hauge RH, Smalley RE, Schmidt J, Talmon Y. Individually Suspended Single-Walled Carbon Nanotubes in Various Surfactants. Nano letters 2003;3(10):1379-1382.

64. Choo-Smith LP, Edwards HG, Endtz HP, Kros JM, Heule F, Barr H, Robinson JS, Jr., Bruining HA, Puppels GJ. Medical applications of Raman spectroscopy: from proof of principle to clinical implementation. Biopolymers 2002;67(1):1-9.

65. Owen CA, Notingher I, Hill R, Stevens M, Hench LL. Progress in Raman spectroscopy in the fields of tissue engineering, diagnostics and toxicological testing. Journal of materials science 2006;17(11):1019-1023.

66. Jorio A, Pimenta MA, Filho GS, Saito R, Dresselhaus G, Dresselhaus MS. Characterizing carbon nanotube samples with resonance Raman scattering. New Journal of Physics 2003;5:139.

67. Dresselhaus MS, Dresselhaus G, Jorio A, Souza Filho AG, Samsonidze GG, Saito R. Science and applications of single-nanotube Raman spectroscopy. Journal of nanoscience and nanotechnology 2003;3(1-2):19-37.

68. Hadjiev VG, Iliev MN, Arepalli S, Nikolaev P, Files BS. Raman scattering test of single-wall carbon nanotube composites. Applied Physics Letters 2001;78(21):3193-3195.

69. Peters MJ, McNeil LE, Lu JP, Kahn D. Structural phase transition in carbon nanotube bundles under pressure. Physical Review B 2000;61(9):5939.

70. Liu Z, Li X, Tabakman SM, Jiang K, Fan S, Dai H. Multiplexed multicolor Raman imaging of live cells with isotopically modified single walled carbon nanotubes. Journal of the American Chemical Society 2008;130(41):13540-13541.

71. Keren S, Zavaleta C, Cheng Z, de la Zerda A, Gheysens O, Gambhir SS. Noninvasive molecular imaging of small living subjects using Raman spectroscopy. Proceedings of the National Academy of Sciences of the United States of America 2008;105(15):5844-5849.

72. Liu Z, Chen K, Davis C, Sherlock S, Cao Q, Chen X, Dai H. Drug delivery with carbon nanotubes for in vivo cancer treatment. Cancer research 2008;68(16):6652-6660.

73. Iijima S, Ichihashi T. Single-shell carbon nanotubes of 1-nm diameter. Nature 1993;363(6430):603-605.

74. Vivekchand SR, Jayakanth R, Govindaraj A, Rao CN. The problem of purifying single-walled carbon nanotubes. Small (Weinheim an der Bergstrasse, Germany) 2005;1(10):920-923.

75. Wick P, Manser P, Limbach LK, Dettlaff-Weglikowska U, Krumeich F, Roth S, Stark WJ, Bruinink A. The degree and kind of agglomeration affect carbon nanotube cytotoxicity. Toxicology letters 2007;168(2):121-131.

76. Rastogi R, Kaushal R, Tripathi SK, Sharma AL, Kaur I, Bharadwaj LM. Comparative study of carbon nanotube dispersion using surfactants. Journal of colloid and interface science 2008;328(2):421-428.

77. Ersen O, Werckmann J, Houlle M, Ledoux MJ, Pham-Huu C. 3D electron microscopy study of metal particles inside multiwalled carbon nanotubes. Nano letters 2007;7(7):1898-1907.

78. Takenaka S, Karg E, Kreyling WG, Lentner B, Möller W, Behnke-Semmler M, Jennen L, Walch A, Michalke B, Schramel P, Heyder J, Schulz H. Distribution Pattern of Inhaled Ultrafine Gold Particles in the Rat Lung. Inhalation toxicology 2006;18(10):733 - 740.

79. Muhlfeld C, Rothen-Rutishauser B, Vanhecke D, Blank F, Gehr P, Ochs M. Visualization and quantitative analysis of nanoparticles in the respiratory tract by transmission electron microscopy. Particle and fibre toxicology 2007;4:11.

80. Rothen-Rutishauser BM, Schurch S, Haenni B, Kapp N, Gehr P. Interaction of fine particles and nanoparticles with red blood cells visualized with advanced microscopic techniques. Environmental science & technology 2006;40(14):4353-4359.

81. Geiser M, Casaulta M, Kupferschmid B, Schulz H, Semmler-Behnke M, Kreyling W. The role of macrophages in the clearance of inhaled ultrafine titanium dioxide particles. American journal of respiratory cell and molecular biology 2008;38(3):371-376.

82. Callaghan P. Principles of nuclear magnetic resonance microscopy. New York: Oxford University Press; 1991.

83. Haacke E, Brown R, Thompson M, Venkatesan R. Magnetic Resonace Imaging: Physical Principles and Sequence Design. New York: Willey; 1999.

84. Wehrli FW. From NMR diffraction and zeugmatography to modern imaging and beyond. Prog Nucl Magn Reson Spectrosc 1995;28(1):87-135.

85. Wright GA. Magnetic resonance imaging. IEEE Sign Proc Mag 1997;14(1):56-66.

86. Driehuys B, Hedlund LW. Imaging techniques for small animal models of pulmonary disease: MR microscopy. Toxicologic pathology 2007;35(1):49-58.

87. Beckmann N, Tigani B, Mazzoni L, Fozard JR. MRI of lung parenchyma in rats and mice using a gradient-echo sequence. NMR in biomedicine 2001;14(5):297-306.

88. Cassidy PJ, Schneider JE, Grieve SM, Lygate C, Neubauer S, Clarke K. Assessment of motion gating strategies for mouse magnetic resonance at high magnetic fields. J Magn Reson Imaging 2004;19(2):229-237.

89. Mosbah K, Ruiz-Cabello J, Berthezene Y, Cremillieux Y. Aerosols and gaseous contrast agents for magnetic resonance imaging of the lung. Contrast media & molecular imaging 2008;3(5):173-190.

90. Bannier E, Neyran B, Cieslar K, Rivoire J, Heidemann RM, Gaillard S, Sulaiman AR, Canet-Soulas E, Cremillieux Y. Free breathing hyperpolarized 3He lung ventilation spiral MR imaging. Investigative radiology 2009;44(4):185-191.

91. Hiba B, Richard N, Janier M, Croisille P. Cardiac and respiratory double self-gated cine MRI in the mouse at 7 T. Magn Reson Med 2006;55(3):506-513.

92. Beckmann N, Tigani B, Ekatodramis D, Borer R, Mazzoni L, Fozard JR. Pulmonary edema induced by allergen challenge in the rat: noninvasive assessment by magnetic resonance imaging. Magn Reson Med 2001;45(1):88-95.

93. Beckmann N, Tigani B, Sugar R, Jackson AD, Jones G, Mazzoni L, Fozard JR. Noninvasive detection of endotoxin-induced mucus hypersecretion in rat lung by MRI. American journal of physiology 2002;283(1):L22-30.

94. Tigani B, Schaeublin E, Sugar R, Jackson AD, Fozard JR, Beckmann N. Pulmonary inflammation monitored noninvasively by MRI in freely breathing rats. Biochemical and biophysical research communications 2002;292(1):216-221.

95. Karmouty-Quintana H, Cannet C, Zurbruegg S, Ble FX, Fozard JR, Page CP, Beckmann N. Bleomycin-induced lung injury assessed noninvasively and in spontaneously breathing rats by proton MRI. J Magn Reson Imaging 2007;26(4):941-949.

96. Haage P, Karaagac S, Spuntrup E, Truong HT, Schmidt T, Gunther RW. Feasibility of pulmonary ventilation visualization with aerosolized magnetic resonance contrast media. Investigative radiology 2005;40(2):85-88.

97. Edelman RR, Hatabu H, Tadamura E, Li W, Prasad PV. Noninvasive assessment of regional ventilation in the human lung using oxygen-enhanced magnetic resonance imaging. Nat Med 1996;2(11):1236-1239.

98. Tyler DJ, Robson MD, Henkelman RM, Young IR, Bydder GM. Magnetic resonance imaging with ultrashort TE (UTE) PULSE sequences: technical considerations. J Magn Reson Imaging 2007;25(2):279-289.

99. Robson MD, Gatehouse PD, Bydder M, Bydder GM. Magnetic resonance: an introduction to ultrashort TE (UTE) imaging. Journal of computer assisted tomography 2003;27(6):825-846.

100. Kuethe DO, Caprihan A, Fukushima E, Waggoner RA. Imaging lungs using inert fluorinated gases. Magnetic Resonance in Medicine 1998;39(1):85-88.

101. Beckmann N, Cannet C, Karmouty-Quintana H, Tigani B, Zurbruegg S, Ble FX, Cremillieux Y, Trifilieff A. Lung MRI for experimental drug research. European journal of radiology 2007;64(3):381-396.

102. Albert MS, Cates GD, Driehuys B, Happer W, Saam B, Springer CS, Wishnia A. Biological magnetic resonance imaging using laser-polarized 129Xe. Nature 1994;370(6486):199-201.

103. Fain SB, Korosec FR, Holmes JH, O'Halloran R, Sorkness RL, Grist TM. Functional lung imaging using hyperpolarized gas MRI. Journal of Magnetic Resonance Imaging 2007;25(5):910-923.

104. Goodson BM. Nuclear magnetic resonance of laser-polarized noble gases in molecules, materials, and organisms. J Magn Reson 2002;155(2):157-216.

105. Möller HE, Chen XJ, Saam B, Hagspiel KD, Johnson GA, Altes TA, Lange EEd, Kauczor H-U. MRI of the lungs using hyperpolarized noble gases. Magnetic Resonance in Medicine 2002;47(6):1029-1051.

106. Stupar V, Berthezene Y, Canet E, Tournier H, Dupuich D, Cremillieux Y. Helium3 polarization using spin exchange technique: application to simultaneous pulmonary ventilation/perfusion imaging in small animals. Investigative radiology 2003;38(6):334-340.

107. Van Beek EJR, Wild JM, Kauczor H-U, Schreiber W, Mugler III JP, De Lange EE. Functional MRI of the lung using hyperpolarized 3-helium gas. Journal of Magnetic Resonance Imaging 2004;20(4):540-554.

108. Harris PD, Barnes R. The uses of helium and xenon in current clinical practice. Anaesthesia 2008;63(3):284-293.

109. Zhao L, Albert MS. Biomedical imaging using hyperpolarized noble gas MRI: Pulse sequence considerations. Nuclear Instruments and Methods in Physics Research Section A: Accelerators, Spectrometers, Detectors and Associated Equipment 1998;402(2-3):454-460.

110. Stupar V, Canet-Soulas E, Gaillard S, Alsaid H, Beckmann N, Cremillieux Y. Retrospective cine 3He ventilation imaging under spontaneous breathing conditions: a non-invasive protocol for small-animal lung function imaging. NMR in biomedicine 2007;20(2):104-112.

111. Viallon M, Berthezene Y, Callot V, Bourgeois M, Humblot H, Briguet A, Cremillieux Y. Dynamic imaging of hyperpolarized (3)He distribution in rat lungs using interleaved-spiral scans. NMR in biomedicine 2000;13(4):207-213.

112. O'Sullivan JD. A fast sinc function gridding algorithm for fourier inversion in computer tomography. IEEE transactions on medical imaging 1985;4(4):200-207.

Manuscript I

Longitudinal ^{3}He and Proton Imaging of Magnetite Biodistribution in a Rat Model of Instilled Nanoparticles

Magnetic Resonance in Medicine 59:1298–1303 (2008)

1. Preface:

To assess the biodistribution of nanoparticles and the induced pulmonary functional alterations after exposition to a rat model, the potential of combined noninvasive HP-^{3}He lung MRI and proton systemic MRI were used.

Magnetite nanoparticles, currently referenced for medical imaging applications as ultra-small particle iron oxide (USPIO), were preferred in this feasibility study.

Super-paramagnetic USPIO were known to affect the transversal relaxation time of the nuclear magnetization and the proton/helium-3 magnetic environment (susceptibility effect) and were widely used in biomedical MRI as negative contrast agent.

The presence of iron nanoparticles translates into hypo-intense regions and induces a significant drop in the MR signal intensity of the ^{3}He ventilation images and the proton systemic images.

A dose range and a follow-up study of the nanoparticle distribution in lungs, liver, spleen and kidneys using HP-^{3}He and proton MRI were reported. *In vivo* MRI findings were compared with *ex vivo* iron assay and histological analysis.

A radial sequence with two different echo times (40µs and 1ms) and a total acquisition time of 20s was used for HP-^{3}He lung imaging and a gradient echo sequence sensitive to changes of relaxation time values was preferred for proton systemic imaging.

2. Manuscript 1:

Longitudinal ^{3}He and Proton imaging of magnetite biodistribution in a rat model of instilled nanoparticles

Achraf Al Faraj[1], Ghislaine Lacroix[2], Hasan Alsaid[1], Dan Elgrabi[2], Vasile Stupar[1], Franck Robidel[2], Sophie Gaillard[1], Emmanuelle Canet-Soulas[1], and Yannick Crémillieux[1*]

[1]Université Lyon 1, Villeurbanne, F-69622, France; CNRS, UMR 5220, U630 INSERM, CREATIS-LRMN; ESCPE Lyon, Villeurbanne, F-69622, France.

[2]INERIS, Parc Technologique Alata, 60550 Verneuil-en-Halatte, France

Abstract:

Epidemiological and toxicological studies have provided evidence that accidentally inhaled nano-size ultrafine particles can induce chronic or acute health damage. MRI, being noninvasive, is able to assess the biodistribution and clearance of magnetically labeled nanoparticles induced by instillation or inhalation. We here report ^{3}He and proton MRI follow-up of lung, liver, spleen and kidney distribution of USPIO (ultrasmall superparamagnetic iron oxide) in a rat model. The sensitivity of the imaging technique to various concentrations of instilled magnetite suspension was first assessed *in vivo* (n=12). A 2-week longitudinal imaging study was then performed on animals (n=7) instilled with a 0.5 mg magnetite solution. Hypo-intense and void signal regions associated with intrapulmonary USPIO were observed in the ^{3}He ventilation images throughout the study, whereas no USPIO-related proton signal intensity changes were found. Intrapulmonary magnetite nanoparticle confinement was confirmed by *ex vivo* iron assay and histological analysis. This study demonstrates that combined ^{3}He and proton MRI enables noninvasive assessment of the distribution and clearance of magnetically labeled instilled nanoparticles.

Introduction:

Nanotechnology is a rapidly growing research and industrial field, fuelled by the numerous revolutionary benefits and applications of nanoparticles and nano-objects in the fields of medicine, energy, materials, etc. However, there are some concerns about the potential impact of these new materials on human health and the environment, mainly due to the fact that their physical activity and reactivity can change drastically according to their surface-to-volume ratio. Accidentally inhaled, they may induce chronic or acute health damage, whether in the pulmonary system or, passing the pulmonary barrier, in remote organs (1). It is thus of prime importance to assess their biodistribution and clearance and to assess their nanotoxicity and biological effects.

MRI, with its high spatial resolution, is one of the best noninvasive imaging techniques used today for medical diagnosis and tissue characterization. Standard MRI (proton imaging) gives morphological and functional images of various organs – with, however, the exception of the lungs, because of magnetic susceptibility due to the heterogeneity of microscopic structures (air-tissue interfaces) and because of their weak proton density (2). Pulmonary ventilation imaging with excellent spatial and temporal resolution is, however, possible using hyperpolarized (HP) ^{3}He (3-5).

The present study assessed the potential of combined ^{3}He and proton MRI for noninvasive monitoring of the biodistribution of magnetically labeled nanoparticles and the pulmonary functional alterations induced. An experimental animal model instilled with a solution of USPIO (ultrasmall superparamagnetic iron oxide) nanoparticles was investigated. A dose range and a follow-up study of the nanoparticle distribution in lungs, liver, spleen and kidneys using ^{3}He and proton MRI were reported. *In vivo* MRI findings were compared with *ex vivo* iron assay and histological analysis.

For this feasibility study, intra-tracheal instillation (ITI) of nanoparticles was preferred to inhalation procedure. ITI is a reproducible administration technique in the lungs, designed to choose the appropriate aqueous suspension dose of particles, after dissociation to respirable size by sonication (6). Indeed, ITI is the most suitable technique for pulmonary absorption and deposition studies where dosage precision is of prime concern (7). When

administrated by intra-tracheal instillation (ITI), the bolus of particle suspension enters deeper into rat lungs during breathing after hyperventilation.

Materials and methods:

Particles:

Non-coated iron-based nanoparticles (magnetite: Fe_3O_4) with a diameter of 20-30 nm (iron oxide nanopowder #637106, Aldrich, France) were suspended in saline (0.15 mL NaCl 0.9%) and sonicated for at least 10 minutes in an ultrasonic bath.

Animals:

Six- to eight-week old male Sprague-Dawley rats were obtained from Charles River (L'Arbresle, France). Animals were housed in the Lyon-1 University animal-care unit, a facility accredited by the local veterinary authority. They had free access to conventional laboratory diet and water and were handled in accordance with official French guidelines for the care and use of laboratory animals.

Animal exposure and experimental design:

Twelve rats were used in the dose-range and in the follow-up study. They were anesthetized by intramuscular administration of 0.12 ml/100g of the following mixture: 3.5 ml of ketamine (1000 mg/ml, Virbac, Carros, France), 3ml of xylazine (2%, Bayer HealthCare, Leverkusen, Germany) and 1 ml of atropine (1mg/ml, Aguettant, Lyon, France).

Nanoparticles were instilled via an intratracheal plastic catheter after hyperventilation (ventilator model 683, Harvard apparatus, Holliston, MA) for 30 seconds at 150 strokes per min (tidal volume = 2.5 ml).

In the dose-range study, the animals were divided into four groups: group 1 comprised three control animals instilled with saline (vehicle controls), and groups 2, 3 and 4

comprised three animals each instilled with 1 mg, 0.5 mg and 0.1 mg of magnetite nanoparticles respectively, by intratracheal route. Pulmonary ^{3}He and systemic proton imaging was performed at day 0 (D0) and day 3 (D3). Animals were sacrificed for post-mortem study.

In the follow-up study, seven animals were instilled with 0.5 mg of magnetite nanoparticles by intratracheal route. Three control animals were instilled with saline. A second control group (n=2) received an intravenous injection of 0.5 mg of magnetite suspension (intravenous controls). Pulmonary and systemic imaging was performed at D0, D2, D7 and D14 and animals were sacrificed at the end of the 2 weeks. A water tube used as a reference was positioned on the rat to enable contrast-to-noise ratio (CNR) measurement and proton NMR signal normalization.

Lung ventilation imaging:

Acquisition:

Lung ventilation imaging was performed on a 12-cm bore 2 Tesla Oxford magnet (Oxford magnet, Oxford, UK) with actively shielded gradients (180 mT/m) interfaced to an MRRS console (MRRS, Guildford, UK). An 8-cm diameter Alderman-Grant RF coil tuned to the ^{3}He frequency was used. ^{3}He polarization was achieved by a spin-exchange optical pumping system (8). A breathing mask was fitted on the rat's head and the animal was allowed to breathe freely from the ^{3}He reservoir during the 20 seconds of ventilation image acquisition (9). Pulmonary ventilation images using a radial imaging sequence were acquired with two different echo times of 40 μs and 1 ms, to evaluate simultaneously ventilation and lung susceptibility effects after iron particles ITI. A total of 200 radial projections with 128 samples were acquired per image. The repetition time was 10 ms and the field of view (FOV) was 80mm with a flip angle of 30°.

Image reconstruction and image analysis:

Image reconstruction and analysis were carried out using IDL software (RSI, Boulder, CO). Ventilation images were reconstructed using a retrospective Cine approach (9) with the

synchronization of the image acquisition with the breathing pattern of the animal. Each reconstructed ventilation image corresponded to a 100-ms time window.

For the measurement of the image signal-to-noise ratio (SNR), the maximal intensity grayscale image, corresponding to the end-inspiration breathing cycle, was selected. A region of interest (ROI) encompassing the whole lung was manually selected. The inclusion of the whole lung was based on the ventilation image obtained with 40µs echo time.

Systemic proton imaging:

Acquisition:

To evaluate systemic iron particles distribution, susceptibility proton imaging was performed on a 10-cm bore actively-shielded 4.7 Tesla Bruker magnet (Bruker Biospin GmbH, Rheinstetten, Germany) interfaced to ParaVision software for preclinical MR imaging research. A Bruker transmission and reception proton volume RF coil was used for good RF homogeneity over the volume of interest. A gradient echo sequence with TR/TE = 380/5 ms, flip angle = 30°, FOV = 6 cm, 4 averages, and a pixel resolution of 430x430µm were used. Axial slices (thickness = 2mm) were positioned so as to image the organs of interest (liver, spleen and kidneys). In the follow-up study, a reference water tube positioned on the rat was used to normalize the SNR and to enable CNR analysis in the various organs. The imaging protocol was identical for each animal.

Image analysis:

For whole body 2D proton images, CNR was calculated using ImageJ software (NIH, Bethesda, MD) on a region of interest (ROI) in liver, spleen and kidneys to compare and quantify the effect of the nanoparticles: $CNR = \frac{(SNR_{ref} - SNR_{ROI})}{SNR_{ref}}$ with $SNR = \frac{Mean_{Signal}}{SD_{Noise}}$

where *ref* refers to the water tube reference and SD is the standard deviation of the noise in the image.

Chemical assay:

After completion of the imaging studies, the animals were sacrificed by intraperitoneal injection of pentobarbital. Blood was sampled and the lungs, liver, kidneys, spleen, heart, brain, thymus, lymph nodes (LN) and testicles were removed for ICP-OES (Inductively Coupled Plasma – Optical Emission Spectrometer) iron assay and histological analysis.

The organs were weighed and lyophilized for 24 hours in a freeze dryer (Alpha 1-4, Christ, Osterode, Germany). They were then mineralized in 5 mL nitric acid, and heated at 180°C for 15 min in a microwave oven (MarsXpress, CEM, Matthews, NC). The mixture was filtrated and the volume was adjusted to 20 or 50 mL with distilled water. Samples were then analyzed for iron content by ICP-OES (Ultima, HORIBA Jobin Yvon, Edison, NJ). The difference measured between control and treated animals represent the iron from nanoparticles.

Histological study:

The lungs of one control rat and three instilled rats from the follow-up study were removed and fixed in formaldehyde. They were then dehydrated and embedded in paraffin. 5-µm transverse sections were cut (Leica 2045 microtome) and stained with hematoxylin-phloxine-saffron (HPS). The hematoxylin stains cell nuclei, the phloxine stains the cytoplasm and connective tissue, and the saffron stains collagen and connective tissue. With this technique, the cell nuclei are colored in dark blue, the cytoplasm in shades of red and the connective tissues are in yellow.

Statistical analyses:

All data are expressed as means ± SD. Non-parametric statistical tests (SPSS, SPSS Inc, Chicago, IL) were done; Kruskal Wallis for unpaired groups and Friedman test for comparison between time. A p value <0.05 was considered significant for all tests.

Results:

Injected and instilled rats started with a weight of 260 ± 5 g. They had a standard and normal gain, weighing 340 ± 10 g at the completion of the follow-up study, identical to controls, and without any abnormal behavior.

^{3}He lung imaging:

i- Dose-range study:

^{3}He images acquired before and after instillation, with a short 40 µs echo-time (TE), exhibited homogeneous lung ventilation patterns, and no ventilation defect was observed in any of the groups.

^{3}He images acquired with a long TE (1 ms) demonstrated increasing signal intensity loss with increasing magnetite concentration (Fig. 1). This effect predominated in the left lung.

Image SNR with 1-ms TE was found to decrease with the quantity of instilled iron particles: 22.3 ± 0.7 with 0.1 mg, 17.1 ± 1.4 with 0.5 mg, and 13.1 ± 4.6 with 1 mg magnetite.

No signal loss was observed in control animals instilled with saline, where the SNR was 23.6 ± 1.

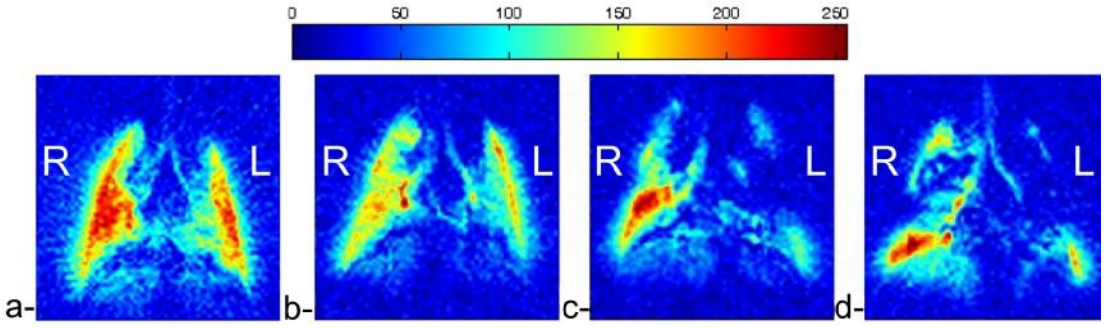

Figure1: Color chart of ^{3}He images acquired with a long (1ms) TE in the dose-range study showing the effect of magnetite (a-control; b-0.1mg; c-0.5mg; d-1mg). Scale corresponds

to arbitrary unit.

ii- Follow-up study:

^{3}He images acquired with a short 40-µs TE demonstrated homogeneous ventilation without noticeable defects.

Ventilation images acquired with 1-ms TE exhibited hypo-intense and void signal regions in all animals instilled with the 0.5 mg magnetite suspension. During the 2-week study, lung ventilation images (Fig. 2) gradually recovered a more homogeneous pattern with increasing signal intensity, SNR increasing from 11.8 ± 2.2 (day 2) and 11.5 ± 1.9 (day 7) to 18.3 ± 3 (day 14).

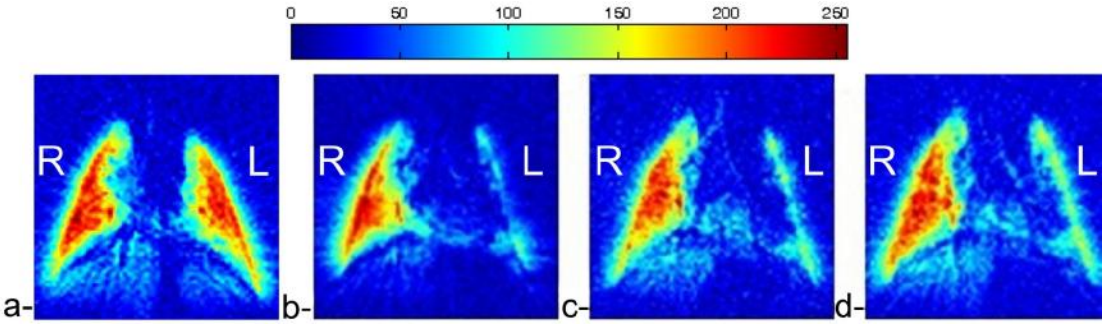

Figure2: Color chart of ^{3}He images acquired with a long (1ms) TE in the follow-up study showing the effect of magnetite (a-control; b-day 2; c-day7; c-day14). Scale corresponds to arbitrary unit.

The two control groups did not exhibit any detectable hypo-intense regions, and SNR was stable, varying from 16.9 ± 1.4 to 20.8 ± 4.1 for saline instillation controls and 16.5 ± 0.4 to 16.6 ± 0.4 for magnetite injection controls.

Systemic proton imaging:

i- Dose-range study:

Axial proton images of the various organs of interest (kidneys, spleen and liver) (Fig. 3) and SNR measurements showed no difference between control and instilled rats, even at the highest dose, whether at day 0 or at day 3 (data not shown).

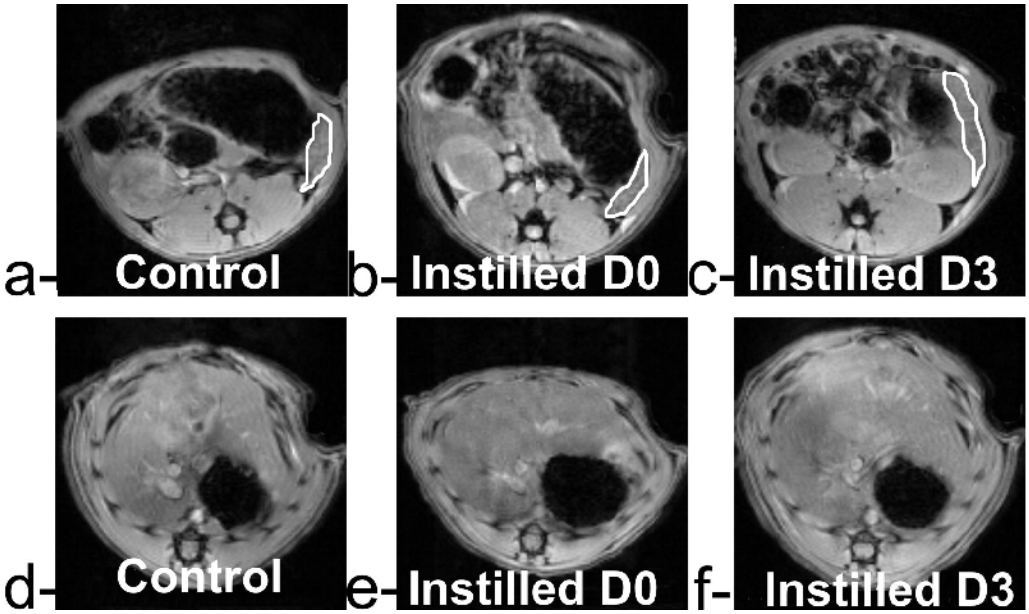

Figure3: Top row: axial images at the kidneys and spleen (white contour) level of control (a) and instilled with 1 mg magnetite (highest instillation dose of the dose range study) at day0 (b) and day3 (c). Bottom row: axial images at the level of the liver of control (d) and instilled with 1 mg magnetite (highest instillation dose of the dose range study) at day0 (e) and at day3 (f).

ii- Follow-up study:

In the magnetite-instilled group, the liver, spleen and kidney CNR values on proton imaging remained unchanged over the 2-weeks of the investigation and were not statistically different from control values (Fig. 4 and Table 1) ($p > 0.05$).

On Day0, magnetite-injected animals exhibited a 3-5 fold CNR increase in liver from (20.2 ± 4.4 to 70.6 ± 14.7) and spleen (from 16.5 ± 5 to 81 ± 1.4) relative to the saline controls due to iron particle accumulation, which gradually decreased over the 2 weeks of the study (Fig. 4 and Table 1).

A small decrease in kidney CNR was also observed between day 2 and day 14.

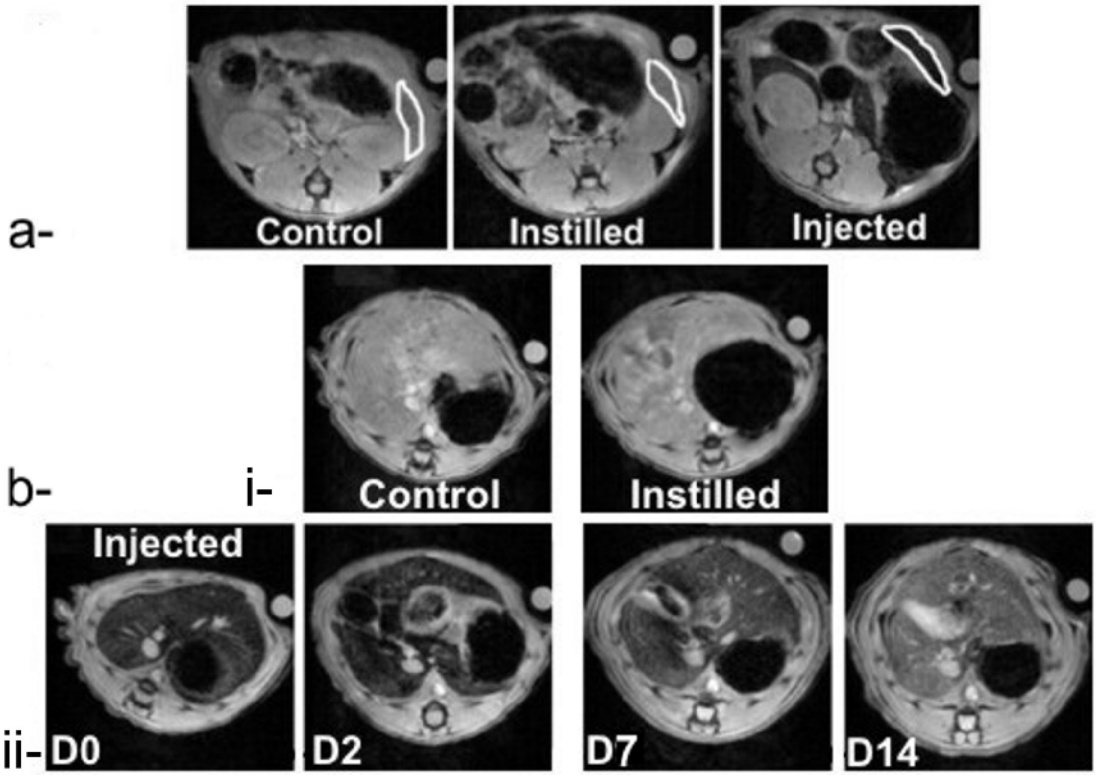

Figure4: a- Axial images showing the kidneys and the spleen (white contour) of control, instilled and injected rats at day 0. b- Axial images showing the liver, i- control and instilled rats, ii- injected rats at day 0, day 2, day 7 and day 14 respectively.

	Kidneys			Spleen			Liver		
CNR	Control	Instilled	Injected	Control	Instilled	Injected	Control	Instilled	Injected
D0	5.5±6.2	-1.3±6.1	0.5±3	16.5±5	13.5±6	81.3±1.4	20.2±4.5	24.2±11.2	70.6±14.7
D2	2.6±4.6	-3.7±6.3	-11.7±5.8	15.8±3.9	16.6±6.2	74.7±3.6	19.4±9.2	21.9±11.7	61.8±9.9
D7	5.9±4.2	-3.6±3.2	-16±4.8	18.6±1.5	18.7±2.8	56.6±2.9	17.5±9.5	25.8±12.8	50.6±9.2
D14	6.9±2.9	-11.5±6	-21.2±6.1	18.2±1.9	10±6.2	44.3±1.9	25.4±7.5	19.2±10	36.18±13

Table1: CNR of kidneys, spleen and liver for control (n=3), instilled (n=7) and injected (n=2) rats after administration (injection or instillation) of 0.5mg of magnetite at day 0, day 2, day 7 and day 14.

Chemical assay:

In the magnetite-instilled group, the concentration of iron in the lungs measured by ICP-OES at day 3 (dose range study) and day 14 (follow-up study) was respectively 72% (±10, n=3) and 88% (±5, n=4) of the initial instilled iron concentration. Blood, liver, spleen, kidneys, testicles, heart, brain and thymus concentrations in instilled animals were not statistically different from control values in either study (Table 2).

Iron Assay	Control (n=2)	Instilled (n=4)	Injected (n=2)
Lung	67.9±5.6	278.1±6.8	93.5±6.7
Liver	103.5±30.4	104.6±21.6	339.5
Spleen	347.9±45.5	341.8±64.7	492.3±78.7
Kidneys	68.2±9.5	59.7±8.1	91.4±12.3
Blood	384.8±9.6	410.2±61.4	487.8±45.8
Brain	13.8±0.9	17.6±2	22.3±4.5
Heart	91.9±28.1	95.8±20.6	96.1±24.4
Thymus+LN	32.8±11	35.0±9.9	39.1±9.4
Testicles	15.1±1.4	14.2±1.3	13.7±1.8

Table2: Iron assay by ICP-OES in µg/g of organ in the follow-up study after sacrifice at day 14.

In the magnetite-injected group, a 3-fold increase in iron concentration was measured at day 14 in the liver compared with control or instilled groups, with a smaller augmentation in the spleen, kidneys and blood.

Histological study:

HPS-stained 5µm histological slices from the control and instilled rats in the follow-up study showed no pulmonary lesions. Iron particles were clearly visible as brown spots on high magnification images of HPS-stained lung slices (Fig. 5).

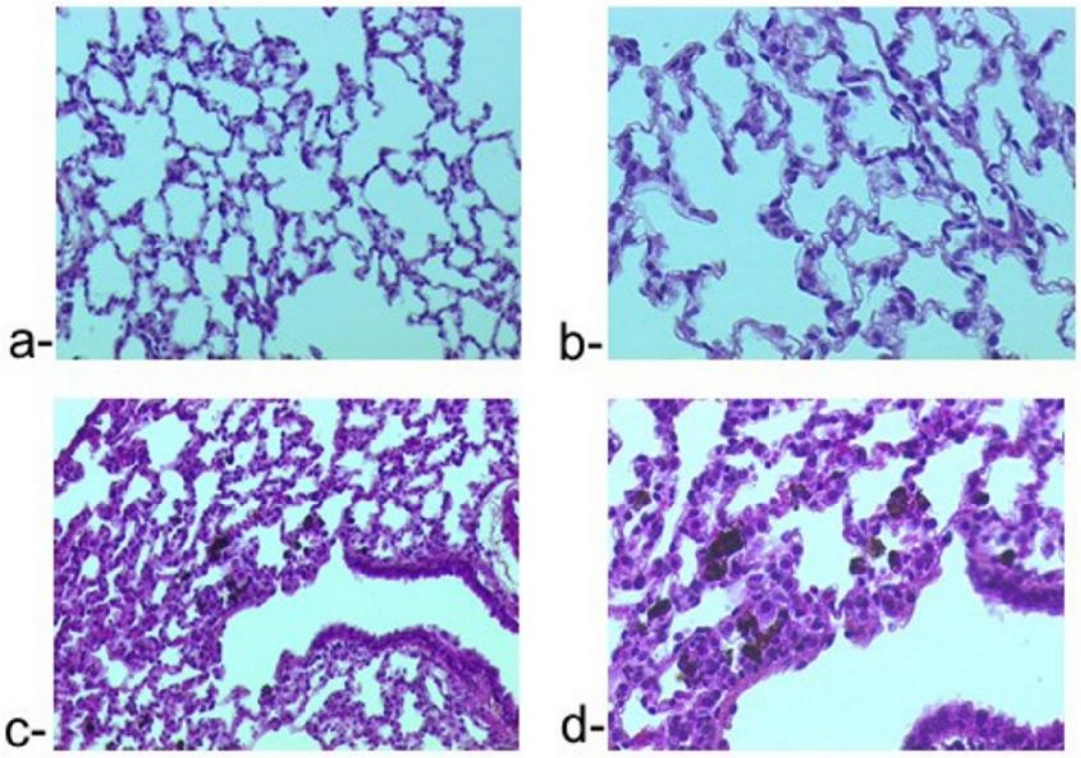

Figure5: Histological cuts of the lungs of a control rat (a: 100x, b: 200x) and of a 0.5 mg instilled rat (c: 100x, d: 200x) showing the presence of iron associated macrophages.

Discussion:

^{3}He lung images acquired in the dose-range study showed that the effects of magnetite could be detected on ventilation images acquired at a 1-ms TE with a 0.1 mg magnetite suspension. It was observed that the sensitivity of detection could be improved using longer

echo times (data not shown here), but a 1-ms TE was chosen as a good compromise between sensitivity to magnetite suspension and image quality.

For the follow-up study, instillation with 0.5 mg magnetite suspension was chosen due to the expected decrease in intrapulmonary magnetite levels with time.

The ventilation images acquired at very short echo time (40 μs) exhibited homogenous ventilation patterns identical to controls. The ventilation defects visible with a long (1 ms) TE were thus related to signal attenuation due to the local increase in magnetic susceptibility induced by the instilled magnetite solution.

The chemical assay demonstrated that most of the instilled iron (88% in the case of the follow-up study) was still present in the lungs and that only a limited amount of magnetite passed through the pulmonary barrier or was cleared by the mucociliary escalator. This finding is consistent with the absence of any noticeable increase in iron concentration in the systemic organs.

The lower percentage of iron remaining in the dose range study (72 % of instilled iron) was due to an optimization of the instillation protocol (catheter type, instillation angle and more homogeneous suspension) leading to improved intrapulmonary iron particles delivery in the follow-up study.

Thus the 38 % mean SNR increase and the improved image quality observed during the 2-week follow-up study cannot be attributed to clearance of intrapulmonary instilled iron.

One possible explanation of SNR recovery could be pulmonary macrophage degradation of iron oxide particles to ferritin and/or hemosiderin (10), which are antiferromagnetic forms of iron that do not give the same magnetization. Although the net magnetization exhibited by ferritin and hemosiderin is approximately one tenth that of superparamagnetic iron oxide particles, both materials induce significant susceptibility effects (T2* effects) that reduce the proton MR signal when compartmentalized within the cells (11). In the case of ^{3}He MRI, this compartmentalization effect might be not operative, since the gaseous helium and macrophages are in distinct compartments and an increased ^{3}He MR signal can be expected when magnetite degradation takes place.

Another explanation for the increase in image SNR and image homogeneity with time might be related to a more homogenous biodistribution of magnetic materials due to the migration of pulmonary macrophages encapsulating iron particles.

The absence of increased iron concentration in organs other than the lungs after instillation of 0.5 mg magnetite was demonstrated on both *in vitro* analysis and MRI: the passage of the magnetite particles from the alveolar space to the systemic circulation was thus limited.

Although various physical and chemical properties may influence pharmacokinetics and cellular distribution, all iron oxide particles are eventually phagocytosed or endocytosed by the reticulo-endothelial system (RES) (12). The proton images of organs (kidneys, spleen and liver) most likely to accumulate instilled magnetite after passage through the pulmonary membranes and barriers did not show any visual difference from the control rats. CNR analysis of the regions of interest after normalization with an external reference using a water tube did not show any significant effect of the nanoparticles, which were probably captured by pulmonary alveolar macrophages and confined to the alveolar space (13).

With 0.5mg magnetite suspension intravenous injection, a 3- to 5-fold CNR increase in liver and spleen images was observed as expected, decreasing gradually over the 2 weeks of the study, accompanied by a decrease in the CNR in the kidney images. ICP-OES assay after sacrifice at day 14 showed a 2- to 3-fold increase in iron concentration in its various forms in the liver with a small increase in the spleen, kidneys and blood. Thus, comparison of these results with those from injected control animals validated the effectiveness of our *in vivo* MRI technique. Additionally, organs from injected control animals served as the baseline for the *ex vivo* iron assay demonstrating its sensitivity in quantifying iron in organs from magnetite instilled and injected animals.

The *ex vivo* histological analysis confirmed the effectiveness of our instillation procedure for the delivery of nanoparticles to the acinus regions of the lungs. HPS staining is neither Fe nor macrophage-specific marker. The objective was to assess the integrity of lung tissue and localize unstained nanoparticles that are visible as brown particulates.

A limitation of the present study is the lack of quantification of the magnetite effect on the ^{3}He signal. Work in progress includes multi-echo ventilation image acquisition. Following the signal equation $S = S_0 \exp(\frac{-TE}{T_2 *})$, it will be then possible to calculate the T2* value in the presence of the magnetite nanoparticles, which is thought to be inversely proportional to the iron concentration. A pixel-by-pixel map would then represent the local iron concentration, which could be correlated with the iron dosage in the lungs and with the presence of iron on histology.

Another limitation is the lack of direct comparison between ^{3}He and proton images acquired at two different magnetic fields. ^{3}He ventilation imaging does not need a high magnetic field as it relies on the laser-induced polarization of noble gases, whereas for systemic imaging, a higher magnetic field is preferred to get a more pronounced susceptibility effects. For proton images, CNR was used as a metric for the assessment of iron presence. For the ^{3}He studies, in the absence of external gas reference, SNR variations were preferred to estimate the presence of iron particles.

In conclusion, this study illustrates the potential of noninvasive ^{3}He and proton imaging protocols for longitudinal assessment of the distribution of intrapulmonary magnetically labeled nanoparticles. Hypo-intense and void signal regions associated with intrapulmonary USPIO were observed in the ^{3}He ventilation images throughout the study, whereas no USPIO-related proton signal intensity changes were found. In the future, this approach could prove useful for investigating the biodistribution, clearance and biological effects of inhaled or instilled manufactured nanoparticles.

Acknowledgments:

Grant sponsors: This work was supported by a grant from the French Ministry of Education and Research and INERIS (*Institut National de l'Environnement Industriel et des Risques*).

We thank François Duboeuf for his help in statistical analysis and Valbex (Centre de Bioexpérimentation, Université Lyon 1) for rat housing and care.

References:

1. Kreyling WG, Semmler-Behnke M, Moller W. Ultrafine particle-lung interactions: does size matter? J Aerosol Med 2006;19(1):74-83.

2. Kauczor HU, Kreitner KF. MRI of the pulmonary parenchyma. European radiology 1999;9(9):1755-1764.

3. Albert MS, Cates GD, Driehuys B, Happer W, Saam B, Springer CS, Jr., Wishnia A. Biological magnetic resonance imaging using laser-polarized 129Xe. Nature 1994;370(6486):199-201.

4. Moller HE, Chen XJ, Saam B, Hagspiel KD, Johnson GA, Altes TA, de Lange EE, Kauczor HU. MRI of the lungs using hyperpolarized noble gases. Magn Reson Med 2002;47(6):1029-1051.

5. van Beek EJ, Wild JM. Hyperpolarized 3-helium magnetic resonance imaging to probe lung function. Proc Am Thorac Soc 2005;2(6):528-532, 510.

6. Driscoll KE, Costa DL, Hatch G, Henderson R, Oberdorster G, Salem H, Schlesinger RB. Intratracheal instillation as an exposure technique for the evaluation of respiratory tract toxicity: uses and limitations. Toxicol Sci 2000;55(1):24-35.

7. Leong BK, Coombs JK, Sabaitis CP, Rop DA, Aaron CS. Quantitative morphometric analysis of pulmonary deposition of aerosol particles inhaled via intratracheal nebulization, intratracheal instillation or nose-only inhalation in rats. J Appl Toxicol 1998;18(2):149-160.

8. Stupar V, Berthezene Y, Canet E, Tournier H, Dupuich D, Cremillieux Y. Helium3 polarization using spin exchange technique: application to simultaneous pulmonary ventilation/perfusion imaging in small animals. Investigative radiology 2003;38(6):334-340.

9. Stupar V, Canet-Soulas E, Gaillard S, Alsaid H, Beckmann N, Cremillieux Y. Retrospective cine 3He ventilation imaging under spontaneous breathing conditions: a non-invasive protocol for small-animal lung function imaging. NMR in biomedicine 2007;20(2):104-112.

10. Turi JL, Yang F, Garrick MD, Piantadosi CA, Ghio AJ. The iron cycle and oxidative stress in the lung. Free Radic Biol Med 2004;36(7):850-857.

11. Briley-Saebo K, Bjornerud A, Grant D, Ahlstrom H, Berg T, Kindberg GM. Hepatic cellular distribution and degradation of iron oxide nanoparticles following single intravenous injection in rats: implications for magnetic resonance imaging. Cell Tissue Res 2004;316(3):315-323.

12. Allkemper T, Bremer C, Matuszewski L, Ebert W, Reimer P. Contrast-enhanced blood-pool MR angiography with optimized iron oxides: effect of size and dose on vascular contrast enhancement in rabbits. Radiology 2002;223(2):432-438.

13. Geiser M, Rothen-Rutishauser B, Kapp N, Schurch S, Kreyling W, Schulz H, Semmler M, Im Hof V, Heyder J, Gehr P. Ultrafine particles cross cellular membranes by nonphagocytic mechanisms in lungs and in cultured cells. Environ Health Perspect 2005;113(11):1555-1560.

Manuscript II

In vivo Imaging of Carbon Nanotube Biodistribution Using Magnetic Resonance Imaging

Nano Letters 2009, 9 (3), 1023-1027

1. Preface:

In the previous manuscript, the biodistribution of instilled iron nanoparticles (USPIO) was reported in a rat model using combined lung hyperpolarized ^{3}He and whole body ^{1}H MR imaging.

Hypo-intense and void signal regions associated with intrapulmonary USPIO were observed in the ^{3}He ventilation images throughout the 2-week longitudinal study, whereas no USPIO-related proton signal intensity changes were found.

This same approach was used to evaluate the biodistribution and biological impact of raw single-wall CNT (raw-SWCNT) and super-purified SWCNT (SP-SWCNT) after intrapulmonary exposition.

Prior to exposition, SWCNT physicochemical profiles were characterized with transmission electron microscopy (TEM) and inductively chemical plasma mass spectroscopy (ICP-MS) and show that raw-SWCNT sample contain 10% of iron impurities.

These intrinsic metal impurities were large enough to induce a significant drop in magnetic field homogeneity in ^{3}He MR image.

In order to detect and semiquantify the effects of SWCNT iron impurities, a multi-echo radial sequence was implemented to allow measurement of T2* values decrease (susceptibility effects) induced by these impurities.

At end point, histological analysis were performed to assess the integrity of tissue and localize the presence of SWCNT aggregates and to confirm MRI readouts. Inductively coupled plasma – optical emission spectroscopy (ICP-OES) was finally used to obtain a quantitative dosage of iron metal in different organs.

2. Manuscript 2:

In vivo Imaging of Carbon Nanotube Biodistribution Using Magnetic Resonance Imaging

Achraf Al Faraj[1], Katarzyna Cieslar[1], Ghislaine Lacroix[2], Sophie Gaillard[1], Emmanuelle Canet-Soulas[1], and Yannick Crémillieux[1*]

[1]: Université de Lyon, CREATIS-LRMN, CNRS UMR5220, INSERM U630, Lyon, France

[2]: Institut National de l'Environnement Industriel et des Risques, Verneuil-en-Halatte, France

Abstract:

As novel engineered nanoparticles such as carbon nanotubes (CNT) are extensively used in nanotechnology due to their superior properties, it becomes critical to fully understand their biodistribution and effect when accidently inhaled. A noninvasive follow-up study would be beneficial to evaluate the biodistribution and effect of nanotube deposition after exposure directly *in vivo*. Combined helium-3 and proton magnetic resonance resonance (MRI) were used in a rat model to evaluate the biodistribution and biological impact of raw single-wall CNT (raw-SWCNT) and superpurified SWCNT (SP-SWCNT). The susceptibility effects induced by metal impurity in the intrapulmonary instilled raw-SWCNT samples were large enough to induce a significant drop in magnetic field homogeneity detected in ^{3}He MR image acquired under spontaneous breathing conditions using a multiecho radial sequence. No MRI susceptibility variation was observed with SP-SWCNT exposition even though histological analysis confirmed their presence in instilled lungs. Proton MRI allowed detection of intravenously injected raw-SWCNT in spleen and kidneys using gradient echo sequence sensitive to changes of relaxation time values. No signal modifications were observed in the SP-SWCNT injected group. In instilled groups, the contrast-to-noise ratio in liver, spleen, and kidneys stayed unchanged and were comparable to values obtained in the control group. Histological analysis confirms the

absence of SWCNT in systemic organs when SWCNT were intrapulmonary instilled. In conclusion, the presence of SWCNT with associated metal impurities can be detected *in vivo* by noninvasive MR techniques. Hyperpolarized ^{3}He can be used for the investigation of CNT pulmonary biodistribution while standard proton MR can be performed for systemic investigation following injection of CNT solution.

The public health disaster associated with the use of asbestos fibers in the past highlights the importance of identifying rapidly the potential hazards of novel materials. The respiratory toxicity of inhaled dusts and fibers has been recognized for centuries, and related lung diseases are still commonly diagnosed all over the world.

Among different types of nanoparticles, single-walled carbon nanotubes (SWCNT) with their unique and fascinating mechanical, electric and thermal properties (1) may be also uniquely toxic , thus necessitating evaluation of their biodistribution and nanotoxicity.

SWCNT consist of a single layer of carbon atoms arranged in a series of condensed benzene rings rolled-up into a tubular structure. Since their discovery, they are among the most promising engineered nanomaterials used in different domains and for various industrial and commercial applications (2,3).

The extreme aspect ratio (length to diameter ratio) of SWCNT, in addition to their low solubility in aqueous media, suggests toxic properties similar to those observed for other ultrafine and fibrous particles (4). Additional concerns come from studies revealing that particles with nanoscopic dimension are markedly more toxic than larger sized particles (5,6). SWCNT impurities should also be taken into consideration when evaluating SWCNT biological impact. As-synthesized SWCNT contains particles of the transition-metal catalyst that can play a major role in their toxicity, biodistribution and properties (7). The potential hazard of SWCNT strongly depends on the metal content and on the size of the agglomerates.

SWCNT have received special attention with regard to their potential health risks. The majority of research assessing the nanotoxicity of inhaled carbon nanotubes reveals the presence of toxic signs after *in vitro* and *ex vivo* studies in the pulmonary system (8). A noninvasive follow-up study could help to evaluate the biodistribution and effect of nanotube deposition after intrapulmonary exposition directly *in vivo*.

Standard Magnetic Resonance Imaging (proton MRI) has potential advantages over competing noninvasive modalities with respect to spatial and temporal resolution, the range and specificity of functional measures available, and the lack of repeated exposure to

ionizing radiation during longitudinal studies. Because of magnetic susceptibility due to the heterogeneity of microscopic structures (air-tissue interfaces) and because of their weak proton density, the lung remains a difficult organ to image with proton MRI. With the introduction of hyperpolarized (HP) gases (i.e., ^{3}He and ^{129}Xe) acting as contrast agents that diffuse rapidly to fill the airspaces of the lungs and allow visualization and measurement of the ventilated airways and alveolar spaces, pulmonary ventilation imaging is possible (9).

Prior to studying SWCNT biodistribution and biological impacts, their physicochemical profiles were characterized on site (for carbon nanotubes characterization and solution preparation, see Supporting Information). Inductively coupled plasma mass spectrometry (ICP-MS) chemical dosage of 68 different metals showed that raw-SWCNT contained 10.14% (w/w) iron, 0.03% sodium, and 0.02% of nickel compared to 0.8% iron and 0.04% sodium in SP-SWCNT solution. Other metals concentrations were negligible (less than 0.005%). SWCNT characterizations using transmission electron microscopy (TEM) (Figure 1) revealed the presence of impurities (black dots) in the raw samples. These black dots were not observed in superpurified samples.

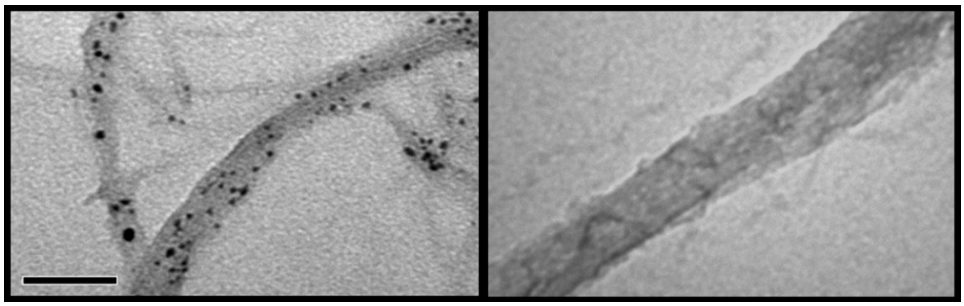

Figure1: TEM images showing the presence of impurities (black dots) in raw-SWCNT bundles (left) and their absence in SP-SWCNT bundles (right). Scale bar represents 50 nm.

In vivo detection and biodistribution imaging of carbon nanotubes (CNT) is an objective shared and pursued by research groups aiming either at developing CNT as drug delivery agents or/and at investigating the toxicity of these nano-objects. As mentioned above, when noninvasive and longitudinal imaging investigations are considered, MRI is a method of choice.

It was recently reported that CNT functionalized with paramagnetic contrast agents (Gadolinium chelates) could be detected *in vivo* with an MRI scanner (10). Similarly, one can certainly take advantages as well of the metal impurities located at the surface or inside the carbon nanotubes (11). Indeed, CNT products may contain non-NT carbon impurities, such as amorphous carbon and metallic nanoparticles (catalysts: Co, Fe, Ni and Mo). The amount and type of impurities are depending on the manufacturers and synthetic methods (i.e., iron carbonyl serve as catalyst during production process) (12,13) and can be the source of additional toxic effects (14).

Following ICP-MS characterization, it was found that the raw-SWCNT used in this study contain more than 10% (w/w) iron while the superpurified single-walled carbon nanotubes SP-SWCNT were almost free of metal impurities. Iron nanoparticles are widely used as a MRI contrast agent in most of the body organs. These particles attenuate the NMR signals of water molecules in surrounding tissues and their presence translates into hypointense regions in the MR image.

Since the overall objective of this work concerned the investigation of accidental exposure to CNT via the respiratory tract and since lung proton MRI has important limitations, hyperpolarized ^{3}He MRI was implemented in this study complementary to the proton MR image readouts.

The application of intravascular iron nanoparticles as contrast agents acting on ^{3}He NMR signal in the broncho-alveolar space was demonstrated previously (15,16). In a recent study, the detection in the lungs, using hyperpolarized ^{3}He, of instilled magnetite nanoparticles (0.5 mg of iron in total) in a rat model was reported (17).

In this study, 2-week follow-up investigations were performed with intrapulmonary intratracheally instilled (ITI) raw (< 35wt% impurities) (group1; n=6) and superpurified (< 5wt% impurities) (group2; n=6) single-walled carbon nanotubes to assess longitudinally their biodistribution and effect on a rat model using helium-3 (pulmonary imaging) and proton MRI (systemic imaging).

Intratracheal instillation (ITI) was preferred in this study because it is a reproducible administration technique in the lung allowing accurate control of the suspension dose administrated. Indeed, ITI is the most suitable technique for pulmonary absorption and deposition studies where dosage precision is of prime concern (18). When administrated by ITI, the bolus of particle suspension enters deeper into rat lungs during breathing after hyperventilation (for Animal exposure and experimental protocol, see Supporting Information).

Additionally, three control groups were included: group3 (n=6) was instilled with albumin-saline solution and group4 and 5 (n=3 for each) were intravenously injected in rat's tail with raw and superpurified carbon nanotubes suspension, respectively. A single exposition dose of 0.5mg SWCNT per animal corresponding approximately to a concentration of 2µg SWCNT per g of bodyweight was applied. This CNT dose was similar to those applied in recently published studies of CNT toxicity (12-14).

Instilled and injected rats started with a weight of 245±7g (n=18). They had a standard and normal weight gain, weighing 335±9g at the completion of the 2 weeks follow-up study, similar to controls (n=6), and without any abnormal behavior.

Superparamagnetic iron nanoparticles are widely used in biomedical MRI as a contrast agent influencing the transverse relaxation time of the nuclear magnetization and the proton magnetic environment (susceptibility effect). In order to detect and semiquantify the effects of SWCNT iron impurities on the NMR ^{3}He signal, a multiecho (TE=40µs, 1ms, 2ms and 3ms) imaging sequence was used (for HP ^{3}He lung MRI protocol, see Supporting Information). The reconstructed ventilation images were obtained at end-inspiration to visualize the largest fraction of ventilated alveolar spaces. A region of interest (ROI) encompassing right and left lung parenchyma was manually selected. The inclusion of lung parenchyma was based on the ventilation image obtained with the shortest echo-time; this image being the least prone to the magnetic susceptibility effect induced by iron impurities. T_2* values were obtained on a voxel by voxel basis after fitting of the NMR signal from the multiecho image set. The coefficient of variation (CV) of the NMR signal intensity from the ROI was calculated to assess the heterogeneity pattern of lung ventilation images. ^{3}He lung ventilation images acquired with the multiecho sequence exhibited hypointense and

void signal regions with 20% T_2* reduction and CV increase up to 48h postexposition (Figure2 and Table1) in animals instilled with the solution of 0.5 mg of raw-SWCNT. Figure2 shows ^{3}He ventilation images (left) at the different echo times for a control and instilled rat at D1, D2 and D7 after instillation with the corresponding T_2* map (right). Images corresponding to injected group, and those of 1 and 2-week postinstilled group did not exhibit any detectable hypointense regions and T_2* values were stable, varying from 7.61±0.23 ms in control group, 7.41±0.32 ms in injected group, and 7.57±0.38 ms after signal recovery in instilled group at D14. A CV increase was also measured in the lung images of raw-SWCNT injected group over the 2-week investigation (Table1). With SP-SWCNT sample, no noticeable defect was observed in instilled group compared to control group (Figure2). T_2* and CV values were statistically unchanged over the period of investigation.

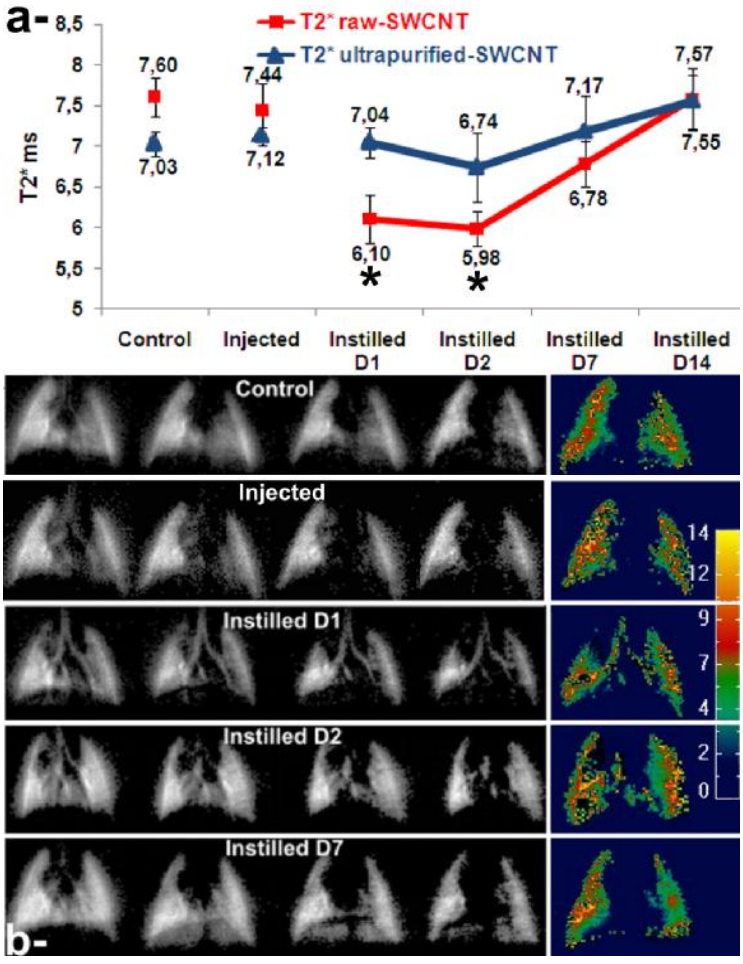

Figure2: (a) Graph showing T_2 measurement in ms for control, injected (averaged over the two weeks investigation) and instilled groups at D1, D2, D7 and D14 after raw-SWCNT exposition in lungs. Asterisk indicates that values are statistically different from control group ($p < 0.05$). (b) ^{3}He lung ventilation images of a control and instilled rat at D1, D2 and D7 after instillation of raw-SWCNT at the different echo time (from left to right: 0.04, 1, 2 and 3-ms) with the corresponding T_2* map (color scale gives the local ^{3}He T_2* in milliseconds).*

Groups		CV raw-SWCNT	CV SP-SWCNT
Group 1 and 2	Instilled D1 (n=3)	0.61±0.04*	0.46±0.01
	Instilled D2 (n=3)	0.59±0.06*	0.46±0.02
	Instilled D7 (n=3)	0.41±0.03	0.44±0.04
	Instilled D14 (n=3)	0.43±0.03	0.43±0.02
Group 3	Control (n=18)	0.44±0.03	
Group 4 and 5	Injected (n=9)	0.52±0.03*	0.45±0.03

Table1: Coefficient of variation of ^{3}He lung signal intensity of different groups in the raw-SWCNT and SP-SWCNT studies: control, injected (averaged over the 2 week investigation) and instilled at different imaging time points.

**: statistically different from control group ($p < 0.05$).*

In the present study, metal impurity in raw-SWCNT samples represented 0.05 mg of iron in the administrated dose. The susceptibility effects (decrease of T_2* values) induced by these impurities in the animal group instilled with raw-SWCNT were large enough to induced a significant drop in T_2* values and an increase in the coefficient of variation in ^{3}He MR image. Changes in T_2* and CV values were not observed (with the exception of CV in the raw-SWCNT injected group) in the control saline-instilled group and in the SP-SWCNT

instilled group. These findings sustain the attribution of susceptibility effects observed in the lungs to iron impurities.

After 2 weeks post-instillation of raw-SWCNT, the ^{3}He T_2* and CV values recovered their baseline values. This transient behavior can be related to a decrease with time of exogen iron concentration in the lungs or/and to changes in the effects of the CNT on the transverse relaxation time of ^{3}He magnetization.

The effects of CNT on the relaxation time of ^{3}He can vary with time through various mechanisms. The access of ^{3}He gas to iron relaxation sources can be limited by SWCNT encapsulation. Homogenization of CNT distribution in the alveolar space can affect the magnitude of the magnetic susceptibility effects. Finally, the incorporation and degradation of iron impurities in ferritin molecules or in hemosiderin deposits can modify the magnetic susceptibility of exogen iron.

To evaluate the presence of SWCNT in systemic organs, a gradient-echo imaging sequence sensitive to changes of relaxation time values was used. Contrast-to-noise ratios (CNR) measured in region of interest in liver, spleen and kidneys, was chosen as an index of SWCNT deposition (for systemic proton MRI protocol, see Supporting Information). Within the liver, ROIs were drawn around apparent vascular structures and these regions subtracted out of the map to retain liver parenchyma only. ROIs encompassing the whole spleen and the two kidneys were manually selected for signal measurement. In systemic MRI, no variation in axial proton images of the various organs of interest (kidneys, spleen, and liver) was observed in instilled groups. CNR values were statistically identical over the 2 week investigation in both raw- and SP-SWCNT exposed animals. The CNR values were similar to those measured in control instilled group. In raw-SWCNT injected group, a 2- to 3- fold decrease of CNR (corresponding to proton NMR signal attenuation) in the spleen and kidneys was observed up to 24 h after injection. This effect decreases gradually with time and CNR values become comparable to control groups two weeks after instillation (Figure3). No statistical changes in CNR values were measured in liver. Systemic proton images in SP-SWCNT groups did not reveal any detectable changes and presented comparable CNR values during the 2-week investigation (data not shown).

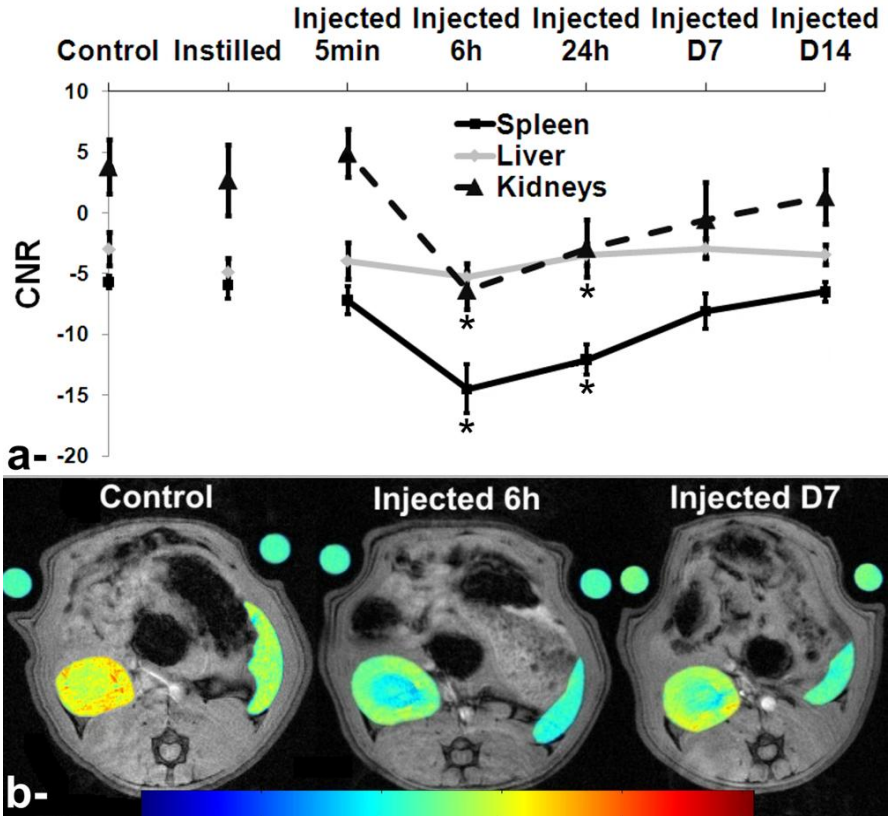

Figure3: (a) graph showing CNR variation of control, instilled (averaged over the two weeks investigation) and injected animals 6h, 24h, 1 and 2 weeks after raw-SWCNT injection in spleen, liver and kidneys.: statistically different from control group ($p < 0.05$); (b) Proton MR images of an injected rat: (i) before, (ii) 6h after, and (iii) 7 days after injection showing signal variation in the spleen and kidneys. The superimposed signal intensity color maps over kidneys and spleen indicate MR signal intensity drop post-injection.*

Susceptibility effects (decrease of proton signal intensity) were measured as well in the spleen and kidneys in the animal group injected with raw-SWCNT. These findings indicate that nanotubes impurities can be used for the detection of CNT in systemic organs using standard proton MR techniques.

Histological slices in lungs (for histological analyses, see Supporting Information), 2 weeks after raw-SWCNT instillation, show the presence of multifocal macrophage-containing granulomas (Figure 4b) which are evidence of a foreign tissue body reaction around the sites of SWCNT aggregates. In the raw-SWCNT injected group, histological lung images show as well the presence of SWCNT in lungs vessels (Figure 4c). Similarly to raw-SWCNT groups, histological lung slices of SP-SWCNT instilled group reveal the presence of multifocal macrophage-containing granulomas (Figure 4a). No presence of CNT was detected on histological slices in systemic organs (liver, spleen and kidneys) in both raw- and SP-SWCNT instilled and injected groups (Figure4d-i).

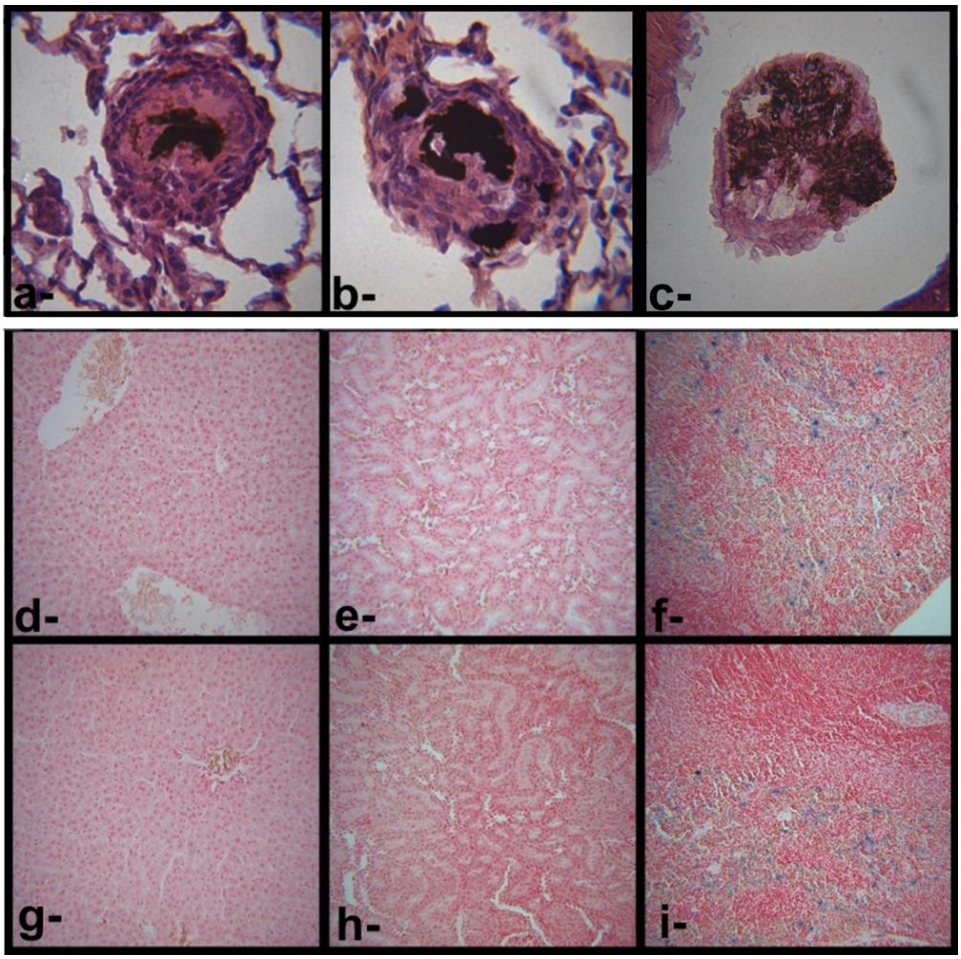

Figure4: (a – c) HES stained histological cuts of lung lobe (magnification: x400) showing the presence of multifocal macrophage-containing granulomas around the sites of SWCNT

aggregates in raw-SWCNT instilled group (a), SP-SWCNT instilled group (b) and raw-SWCNT injected group (c). (d-i) Prussian blue counterstained with NFR histological cuts (magnification: x100) of raw-SWCNT instilled (d–f) and injected (g–i) groups confirming the absence of CNT in systemic organs (liver: left, kidney: middle and spleen: right).

To obtain a quantitative dosage of metal in different organs, the *ex vivo* ICP-OES technique was used. Iron concentration in the liver, spleen, kidneys, and lungs were analyzed in the raw-SWCNT groups only. SWCNT concentration was quantified indirectly through their associated metal impurities. Figure 5 shows iron dosage in µg/g of organ. Animals were exposed to 0.05mg of iron (10.14% of 0.5mg raw-SWCNT) corresponding to 30µg/g of lung. An increase of iron content in lung tissue was observed in the raw-SWCNT instilled animal group (117.72µg/g) as compared to control instilled group (85.14µg/g). However, these values were not statistically different. Similarly, no statistical differences were noticed for the iron content in liver, spleen and kidneys in all the groups.

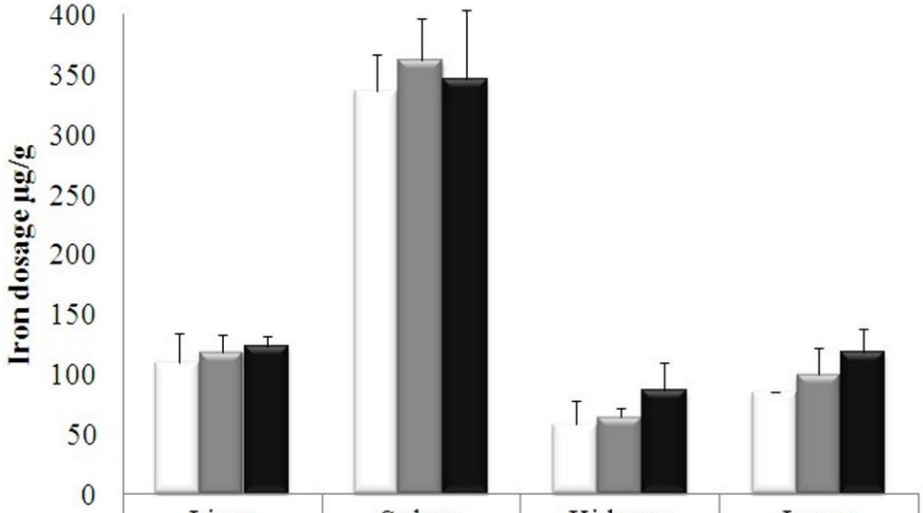

	Liver	Spleen	Kidneys	Lungs
Control	109.71±24.84	336.79±30.53	57.73±20.29	85.14±1.19
Injected	118.38±14.72	361.77±104.35	64.50±6.52	99.30±22.42
Instilled	122.67±8.34	346.56±138.70	85.74±24.36	117.72±19.80

Figure5: Iron dosage in µg/g of liver, spleen, kidneys and lungs in raw-SWCNT study (White: control group, gray: injected group (IV), black: instilled group (IT)) showing no significant difference between groups in the different organs.

Due to significant basal endogen iron concentration in organs as compared to the injected dose of iron, the change in iron concentration in organs after 2 weeks could not be assessed with a high degree of certainty using the *ex vivo* ICP-OES assays. Histopathological slices in lungs do confirm the presence of granulomas, indicative of encapsulated CNT, in the alveolar space. Similar pathological findings were reported in other studies after SWCNT exposition (19-22). Histopathological slices in systemic organs (liver, spleen and kidneys) did not reveal the presence of SWCNT after instillation that could indicate a passage of CNT from the alveolar space to the systemic circulation.

Most nanomaterials tend to exhibit high uptake in the reticuloendothelial system (RES) (i.e., spleen, liver, and lungs) once injected into animals depending on their size and coating materials and are not rapidly excreted by the kidneys. Two weeks post-injection, a slight (but not statistically significant) decrease of proton MR signal intensity was still observed in the kidneys.

In conclusion, the presence of SWCNT with associated metal impurities can be detected *in vivo* by noninvasive MR techniques. Hyperpolarized ^{3}He can be used for the investigation of CNT pulmonary biodistribution while standard proton MR can be performed for systemic investigation following injection of CNT solution. Longitudinal and quantitative evaluation of CNT concentration using MRI remains challenging due to the complex relationship between iron relaxing sources and MR signal amplitude changes. *Ex vivo* analysis at different stages (early, midpoints, and endpoints) might certainly help understand the correlation between iron presence and MR images readouts. For low instilled concentration of iron impurities, iron dosage (for instance using ICP-OES) might not the appropriate technique and an evaluation of CNT concentrations using Raman spectroscopy, as described previously (23), may present a more suitable *ex vivo* technique to quantify directly carbon nanotubes concentration in organs. *In vivo* detection of CNT with MRI as demonstrated in this work will be certainly applied in the future in research programs related to toxicologic impact of CNT and/or biomedical use of these nano-objects.

Acknowledgments: The authors thank INERIS staff for their help in postmortem analyses. This work was supported by the French ANR through RESPINTTOX project (SEST

program). A.A. acknowledges a fellowship from the French Ministry of Education and Research. K.C. acknowledges a fellowship from the European Union Marie Curie Research Training Network PHeLINet Contract number: MRTN-CT-2006-036002.

References:

1. Polizu S, Savadogo O, Poulin P, Yahia L. Applications of carbon nanotubes-based biomaterials in biomedical nanotechnology. J Nanosci Nanotechnol 2006;6(7):1883-1904.

2. Iijima S. Helical microtubules of graphitic carbon. Nature 1991;354(6348):56-58.

3. Giles J. Top five in physics. Nature 2006;441(7091):265.

4. Maynard AD, Baron PA, Foley M, Shvedova AA, Kisin ER, Castranova V. Exposure to carbon nanotube material: aerosol release during the handling of unrefined single-walled carbon nanotube material. Journal of toxicology and environmental health 2004;67(1):87-107.

5. Kipen HM, Laskin DL. Smaller is not always better: nanotechnology yields nanotoxicology. American journal of physiology 2005;289(5):L696-697.

6. Oberdorster G. Pulmonary effects of inhaled ultrafine particles. International archives of occupational and environmental health 2001;74(1):1-8.

7. Bussy C, Cambedouzou J, Lanone S, Leccia E, Heresanu V, Pinault M, Mayne-L'hermite M, Brun N, Mory C, Cotte M, Doucet J, Boczkowski J, Launois P. Carbon nanotubes in macrophages: imaging and chemical analysis by X-ray fluorescence microscopy. Nano letters 2008;8(9):2659-2663.

8. Stern ST, McNeil SE. Nanotechnology safety concerns revisited. Toxicol Sci 2008;101(1):4-21.

9. Fain SB, Korosec FR, Holmes JH, O'Halloran R, Sorkness RL, Grist TM. Functional lung imaging using hyperpolarized gas MRI. J Magn Reson Imaging 2007;25(5):910-923.

10. Richard C, Doan BT, Beloeil JC, Bessodes M, Toth E, Scherman D. Noncovalent functionalization of carbon nanotubes with amphiphilic gd3+ chelates: toward powerful t1 and t2 MRI contrast agents. Nano letters 2008;8(1):232-236.

11. Choi JH, Nguyen FT, Barone PW, Heller DA, Moll AE, Patel D, Boppart SA, Strano MS. Multimodal biomedical imaging with asymmetric single-walled carbon nanotube/iron oxide nanoparticle complexes. Nano letters 2007;7(4):861-867.

12. Vivekchand SR, Jayakanth R, Govindaraj A, Rao CN. The problem of purifying single-walled carbon nanotubes. Small 2005;1(10):920-923.

13. Moisala A, Nasibulin AG, Kauppinen EI. The role of metal nanoparticles in the catalytic production of single-walled carbon nanotubes - a review. Journal of Physics: Condensed Matter 2003;15.

14. Helland A, Wick P, Koehler A, Schmid K, Som C. Reviewing the environmental and human health knowledge base of carbon nanotubes. Environ Health Perspect 2007;115(8):1125-1131.

15. Viallon M, Berthezene Y, Decorps M, Wiart M, Callot V, Bourgeois M, Humblot H, Briguet A, Cremillieux Y. Laser-polarized (3)He as a probe for dynamic regional measurements of lung perfusion and ventilation using magnetic resonance imaging. Magn Reson Med 2000;44(1):1-4.

16. Vignaud A, Maitre X, Guillot G, Durand E, de Rochefort L, Robert P, Vives V, Santus R, Darrasse L. Magnetic susceptibility matching at the air-tissue interface in rat lung by using a superparamagnetic intravascular contrast agent: influence on transverse relaxation time of hyperpolarized helium-3. Magn Reson Med 2005;54(1):28-33.

17. Al Faraj A, Lacroix G, Alsaid H, Elgrabi D, Stupar V, Robidel F, Gaillard S, Canet-Soulas E, Cremillieux Y. Longitudinal 3He and proton imaging of magnetite biodistribution in a rat model of instilled nanoparticles. Magn Reson Med 2008;59(6):1298-1303.

18. Leong BK, Coombs JK, Sabaitis CP, Rop DA, Aaron CS. Quantitative morphometric analysis of pulmonary deposition of aerosol particles inhaled via intratracheal nebulization, intratracheal instillation or nose-only inhalation in rats. J Appl Toxicol 1998;18(2):149-160.

19. Warheit DB, Laurence BR, Reed KL, Roach DH, Reynolds GA, Webb TR. Comparative pulmonary toxicity assessment of single-wall carbon nanotubes in rats. Toxicol Sci 2004;77(1):117-125.

20. Li JG, Li WX, Xu JY, Cai XQ, Liu RL, Li YJ, Zhao QF, Li QN. Comparative study of pathological lesions induced by multiwalled carbon nanotubes in lungs of mice by intratracheal instillation and inhalation. Environ Toxicol 2007;22(4):415-421.

21. Lam CW, James JT, McCluskey R, Hunter RL. Pulmonary toxicity of single-wall carbon nanotubes in mice 7 and 90 days after intratracheal instillation. Toxicol Sci 2004;77(1):126-134.

22. Chou CC, Hsiao HY, Hong QS, Chen CH, Peng YW, Chen HW, Yang PC. Single-Walled Carbon Nanotubes Can Induce Pulmonary Injury in Mouse Model. Nano Lett 2008;8(2):437-445.

23. Liu Z, Cai W, He L, Nakayama N, Chen K, Sun X, Chen X, Dai H. In vivo biodistribution and highly efficient tumour targeting of carbon nanotubes in mice. Nat Nano 2007;2(1):47-52.

3. Supporting Information:

Carbon nanotubes characterization and solution preparation:

CNT were purchased from Carbon Nanotechnologies Incorporated (CNI® Buckytubes, Houston, TX). and synthesized using HiPco (High Pressure Carbon Monoxide) process (1) yielding an individual diameter of 0.8 to 1.2 nm and an individual length of 100 to 1000 nm. They were imaged by transmission electron microscopy (TEM) using a 120 kV microscope (JEM 1400, JOEL) and their metals impurities were analyzed using Inductively Coupled Plasma – Mass spectrometry (ICP-MS). Samples were mineralized with 5 ml nitric acid and 5 ml hydrochloric acid in the microwave oven. Concentrations of 67 different metals were semi-quantitatively measured by ICP-MS (Elan 6100DRC, Perkin-Elmer, ON, Canada). Upon administration to the animals, carbon nanotubes powder were suspended in 150µl saline solution (NaCl 0.9%) containing bovine serum albumin (BSA) to obtain a homogenous and better dispersed CNT solution after at least 10 minutes sonication in an ultrasonic bath (2).

Animal exposure and experimental protocol:

Six- to eight-week old male Sprague-Dawley rats were obtained from Charles River (L'Arbresle, France). Animals were housed in the Lyon-1 University animal-care unit, a facility accredited by the local veterinary authority. They had free access to conventional laboratory diet and water and were handled in accordance with official French guidelines for the care and use of laboratory animals. Animals were anesthetized by intramuscular administration of 0.12 ml/100g of the following mixture: 3.5 ml of ketamine (1000 mg/ml, Virbac, Carros, France), 3ml of xylazine (2%, Bayer HealthCare, Leverkusen, Germany) and 1 ml of atropine (1mg/ml, Aguettant, Lyon, France). Carbon nanotubes instillation was performed via an intratracheal plastic catheter after hyperventilation (ventilator model 683, Harvard apparatus, Holliston, MA) for 30 seconds at 150 strokes per min (tidal volume = 2.5 ml).

HP ^{3}He lung MRI protocol:

Lung ventilation imaging was performed on a 12-cm bore 2 Tesla Oxford magnet (Oxford magnet, Oxford, UK) with actively shielded gradients (180 mT/m) interfaced to an MRRS console (MRRS, Guildford, UK). An 8-cm diameter Alderman-Grant RF coil tuned to the ^{3}He frequency was used. ^{3}He polarization was achieved by a spin-exchange optical pumping system with end polarization levels in the order of 20%. A breathing mask was fitted on the rat's head and the animal was allowed to breathe freely from the ^{3}He reservoir during image acquisition. Pulmonary ventilation images were acquired during animal respiration using a multi-echo radial sequence with 4 interleaved echo times (TE=40µs, 1ms, 2ms and 3ms). A total of 100 radial projections with 128 samples were acquired per image. The repetition time (TR) was 10 ms and the field of view (FOV) was 80mm with a 20° flip angle. Pulmonary imaging protocol was performed 24h, 48h, 7 days and 14 days after exposure. Image reconstruction and analysis were carried out using IDL software (RSI, Boulder, CO).

Systemic proton MRI protocol:

Proton imaging was performed on a 10-cm bore actively-shielded 4.7 Tesla Bruker magnet (Bruker Biospin GmbH, Rheinstetten, Germany) interfaced to ParaVision software for preclinical MR imaging research. A Bruker transmission and reception proton volume RF coil was used for good RF homogeneity over the volume of interest. Gradient echo sequence with TR/TE = 200/3.6, flip angle = 30°, FOV = 6 cm, 2 averages, and a pixel resolution of 234x234µm was used. Axial slices (thickness = 2mm) were positioned so as to image the organs of interest (liver, spleen and kidneys). A water tube used as a reference was positioned on the rat to enable contrast-to-noise ratio (CNR) measurement and proton NMR signal normalization. Proton imaging protocol was repeated 5min, 6h, 24h, 7days and 14days after exposure identically for each animal.

Contrast-to-noise ratio (CNR) was defined as $CNR = \frac{(SNR_{ROI} - SNR_{ref})}{SNR_{ref}}$ with $SNR = \frac{Mean_{Signal}}{SD_{noise}}$ where ref denotes to the water tube reference and SD is the standard deviation of the noise in the image.

Post-mortem studies:

After completion of the imaging studies, the animals were sacrificed by intraperitoneal overdose injection of pentobarbital. Lungs, liver, spleen and kidneys were removed for histological analysis in order to assess the integrity of tissue and to localize the presence of carbon nanotubes, and ICP-OES (Inductively Coupled Plasma – Optical Emission Spectrometer) iron assay in raw-SWCNT study to correlate with non invasive MRI measurements. Systematically for each rat in the different groups, a portion of the lung, liver, spleen and one kidney were removed for histological analysis, and the remaining portion of organs for iron assay. Portions were distributed equally between analyses. In SP-SWCNT study, iron assay was not performed.

Histopathological analysis: Organs were removed and fixed in formaldehyde. They were then dehydrated and embedded in paraffin. 5-µm transverse sections were cut (Leica 2045 microtome) and stained with either hematoxylin-eosin-saffron (HES) or Prussian blue (Perl's reagent) counterstained with nuclear fast red (NFR). HES is a routine staining method which provides excellent contrast between elastic fibers, cytoplasm and connective tissues and allows assessing the integrity of the lung tissue and additionally localizing CNT aggregates which are detectable without any specific coloration. The hematoxylin stains cell nuclei (dark blue), the eosin stains the cytoplasm (red), and the saffron stains collagen and connective tissue (yellow). Prussian blue counterstained with NFR is used to confirm HES results with its high sensitivity. Prussian blue gives a bright blue coloration for iron (ferric ion) and NFR gives pink nonspecific background coloration allowing sensitive detection of carbon nanotubes especially in systemic organs (liver, spleen and kidneys).

Organs iron assay: Samples were weighed and lyophilized for 24 hours in a freeze dryer (Alpha 1-4, Christ, Osterode, Germany). They were then mineralized in 5 ml nitric acid, and heated at 180°C for 15 min in a microwave oven (MarsXpress, CEM, Matthews, NC). The mixture was filtrated and the volume was adjusted to 50 mL with distilled water. Samples were then analyzed for iron content by ICP-OES (Ultima, HORIBA Jobin Yvon, Edison, NJ). The difference in iron content measured between control and treated animals represent the iron from nanotubes.

Statistical analyses:

All data are expressed as means ± SD. Non-parametric statistical tests (SPSS, SPSS Inc, Chicago, IL) were performed; Kruskal Wallis test for unpaired groups and Friedman test for comparison between time. A p value <0.05 was considered significant for all tests.

Reference:

1. Nikolaev P. Gas-phase production of single-walled carbon nanotubes from carbon monoxide: a review of the hipco process. J Nanosci Nanotechnol 2004;4(4):307-316.

2. Elgrabli D, Abella-Gallart S, Aguerre-Chariol O, Robidel F, Rogerieux F, Boczkowski J, Lacroix G. Effect of BSA on carbon nanotube dispersion for *in vivo* and *in vitro* studies. Nanotoxicology 2007;1(4):266 - 278.

Manuscript III

Single-walled carbon nanotubes detection and evaluation of impact using multimodality imaging techniques in a 3-months follow-up study

Submitted manuscript

1. Preface:

As shown in the previous manuscript, the presence of SWCNT with associated metal impurities can be detected *in vivo* by noninvasive MR techniques. Hyperpolarized ^{3}He can be used for the investigation of SWCNT pulmonary biodistribution while standard proton MR can be performed for systemic investigation following injection of SWCNT solution. The object of this manuscript is to show that HP-^{3}He MRI allows *in vivo* detection of SWCNT which will be very useful in research programs related to toxicologic impact of SWCNT after intrapulmonary exposition.

Lung proton MRI is very potent in the detection of fluid secretion related to inflammation and edema or to collagen deposition and atelectasis by providing a high contrast-to-noise ratio with normal lung, i.e. the absence of lung parenchyma MR signal. Lung proton MRI was combined to HP-^{3}He MRI in this 3-month longitudinal study to assess noninvasively the presence of eventual inflammation after SWCNT deposition.

Noninvasive free-breathing lung MRI readouts were correlated to *ex vivo* optical and electron microscopy at different investigation time points to provide an in-depth and complementary view on the biological impact of SWCNT exposition.

Different doses of raw-SWCNT suspension were used to enable a dose dependent evaluation of the harmful effect of SWCNT pulmonary exposition.

2. Manuscript 3:

Single-walled carbon nanotubes detection and evaluation of impact using multimodality imaging techniques in a 3-months follow-up study

Achraf Al Faraj[1], Amine Bessaad[1], Katarzyna Cieslar[1], Ghislaine Lacroix[2], Emmanuelle Canet-Soulas[1], Yannick Crémillieux[1*]

[1] Université Lyon 1, CREATIS-LRMN, CNRS 5220, INSERM U630, Lyon, France.

[2] Institut National de l'Environnement et des Risques Industriels, Verneuil-en-Halatte, France.

Abstract:

Due to their distinctive properties, single-walled carbon nanotubes (SWCNT) are more and more extensively used in nanotechnology. It appears then essential to develop tools for detecting and evaluating their biological impact when accidently inhaled. In a 3-months follow-up study, multimodality imaging techniques combining noninvasive free breathing hyperpolarized ^{3}helium (HP-^{3}He) and proton (H) magnetic resonance imaging (MRI) to *ex vivo* light (histopathological analysis) and transmission electron microscopy (TEM) were used to assess the biodistribution and nanotoxicity of intrapulmonary instilled SWCNT. Specific detection of carbon nanotubes using MRI can be performed *in vivo* relying on their intrinsic metal impurities contained in SWCNT which induce a significant drop in magnetic field homogeneity detected in the ^{3}He MR images. SWCNT was found to produce granulomatous and inflammatory reactions in a time and dose dependent manner.

Introduction:

Single-walled carbon nanotubes (SWCNT) with their unique nanometer-scale structure based on a single layer of graphene with lengths on the order of tens of nanometers to micrometers and their fascinating mechanical, electric and thermal properties are more and more extensively used for different applications in nanotechnology (1). Their high aspect ratio (ratio of length to width) makes them an attractive structural material, but their nanometer-scale diameter and needle-like shape have drawn comparisons with asbestos (2,3). The disaster associated with the use of asbestos fibers in the past and the studies revealing that particles with nanoscopic dimension are markedly more toxic than larger sized particles (4) highlights the importance of identifying rapidly the potential hazards of new materials (5). Knowledge of CNT pathogenic mechanisms and nanotoxic effect is necessary to minimize the danger to exposed individuals (6).

Data on the toxicity of carbon nanotubes *in vivo* is poor and contradictory; however the majority of research performed on cellular or post-mortem models demonstrated that CNT can produce potential health problem after pulmonary exposition (7-10). Alternative ways to study their biodistribution and nanotoxicity *in vivo* after administration to living species are needed, in particular noninvasive imaging techniques.

Magnetic Resonance Imaging (proton MRI) has potential advantages over competing noninvasive modalities with respect to spatial and temporal resolution, the range and specificity of functional measures available, and the lack of repeated exposure to ionizing radiation during longitudinal studies. However, because of magnetic susceptibility due to the heterogeneity of microscopic structures (air-tissue interfaces) and because of their weak proton density, the lung remains a difficult organ to image with proton MRI. With the introduction of hyperpolarized (HP) gases (i.e. ^{3}He, ^{129}Xe) acting as contrast agents that diffuse rapidly to fill the airspaces of the lungs and allow visualization and measurement of the ventilated airways and alveolar spaces, pulmonary ventilation imaging is possible (11-13).

Besides, the absence of lung parenchyma MR proton signal in combination with a background free of artifacts provides a high contrast-to-noise ratio for the detection of fluid

secretion related to inflammation and edema (14,15) or to collagen deposition and atelectasis (hallmarks of fibrosis) (16).

Histopathological analysis, routinely used for *in vitro* and *in vivo* assessment of ultrafine particles toxicity, can be very useful in assessing the integrity of lung tissue and localizing CNT aggregates deposition and pathological effects (i.e. granulomas formation). Due to Van der Waals forces, CNT bundle into ropes, which are further associated into loose aggregates and may also be accessible for detection using light microscopy (17).

Finally, one of the great challenges in studying the impact of nanoparticles in the lung is their visualization within tissues or single cells at a sub-cellular scale. With its nanometric resolution, transmission electron microscopy provides an ideal tool to analyze CNT-related structural changes of the respiratory tract, to localize CNT and detect the presence of inflammatory cells produced with their presence and to investigate the nature of CNT-lung interactions (18). However TEM is not applicable for longitudinal *in vivo* studies.

Specific detection of carbon nanotubes in biological environment can be performed *in vivo* using radio or fluorescent labels (19,20) but these labels may gradually dissociate from the CNT or decay and lose activity over a short period of time. Direct detection of carbon nanotubes can be also performed *ex vivo* using their Raman spectroscopic signatures relying on their intrinsic physical properties rather than radiolabels or spectroscopic tags for indirect detection (21).

Similarly, one can certainly take advantage of different intrinsic metal impurities located at the surface or inside raw carbon nanotubes depending on the manufacturers and synthetic methods (i.e. iron carbonyl serves as catalyst during production process) or label carbon nanotubes with iron nanoparticles to allow their noninvasive *in vivo* detection using MRI.

Due to their strong magnetic moment, iron particles induce magnetic field inhomogeneities in their vicinity and attenuate the NMR signal of water molecules in surrounding tissues. With these contrast properties, CNT can be compared to standard MRI contrast agents used for cellular and molecular imaging in whole body MRI.

The application of injected and instilled iron nanoparticles as contrast agents acting on ^{3}He NMR signal in the broncho-alveolar space has been previously demonstrated (22-24). The presence of iron particles translate into local changes in the MR signal intensity of the ^{3}He ventilation image. Hence, it has been recently reported that SWCNT with associated metal impurities (0.05 mg of iron impurity in total) can be detected noninvasively using HP ^{3}He MRI in a rat model (25). The susceptibility effects induced by the metal impurities contained in the intrapulmonary instilled SWCNT samples were large enough to induce a significant drop in magnetic field homogeneity detected in the ^{3}He MR images.

The purpose of this long term longitudinal study was to assess the biodistribution and nanotoxicity of intratracheally instilled SWCNT in a rat model using multimodality imaging techniques combining noninvasive *in vivo* proton (H) and hyperpolarized ^{3}helium (HP ^{3}He) magnetic resonance imaging (MRI) to *ex vivo* light (histopathological analysis) and transmission electron microscopy (TEM).

Materials and methods:

SWCNT physicochemical characteristics:

Prior to SWCNT exposition, their main physicochemical properties have to be fully characterized. Table1 summarizes their main physicochemical properties.

SWCNT (CNI® Buckytubes, Houston, TX)	
Synthesis process	HiPco (High Pressure Carbon Monoxide)
Diameter	0.8 – 1.2 nm
Length	100 – 1000 nm
Metal impurities	10.14% iron, 0.03% sodium, 0.02% nickel and other metal impurities negligible (less than 0.005%)

Table1: Physicochemical properties of SWCNT used in this study.

SWCNT were characterized by transmission electron microscopy (TEM) using a 120 kV microscope (JEM 1400, JOEL) and their metals impurities were analyzed using Inductively Coupled Plasma – Mass spectrometry (ICP-MS). Samples were mineralized with 5 ml nitric acid and 5 ml hydrochloric acid in the microwave oven. Concentrations of 67 different metals were semi-quantitatively measured by ICP-MS (Elan 6100DRC, Perkin-Elmer, ON, Canada).

Study design:

Six- to eight-week old male Sprague-Dawley rats were obtained from Charles River (L'Arbresle, France). Animals were housed in the Lyon-1 University animal-care unit, a facility accredited by the local veterinary authority. They had free access to conventional laboratory diet and water and were handled in accordance with official French guidelines for the care and use of laboratory animals.

Animals were anesthetized by intramuscular administration of 0.12 ml/100g of the following mixture: 3.5 ml of ketamine (1000 mg/ml), 3ml of xylazine (2%) and 1 ml of atropine (1mg/ml). Atropine was used to reduce mucus secretion.

The numbers of animals in each group with the time of sacrifice for post-mortem analysis are provided in table2.

Groups	Short-term D1	Mid-term D7	Long-term D30	Very long-term D90	Total
Control (BSA-saline vehicle)	1	1	1	2	5
Low dose 0.1mg (0.4mg/kg)	3	3	3	-	9
Mid dose 0.5mg (2mg/kg)	3	3	3	4	13
High dose 1mg (4mg/kg)	3	3	3	-	9

Table2: Number of animals used in the different groups (with the instilled dose corresponding to each group) at the different investigation time point.

Carbon nanotubes intratracheal instillation was performed via an intratracheal plastic catheter after hyperventilation (ventilator model 683, Harvard apparatus, Holliston, MA) for 30 seconds at 150 strokes per min (tidal volume = 2.5 ml).

HP ^{3}He lung MRI:

Acquisition:

HP ^{3}He lung ventilation imaging was performed on a 12-cm bore 2 Tesla Oxford magnet (Oxford magnet, Oxford, UK) with actively shielded gradients (180 mT/m) interfaced to an MRRS console (MRRS, Guildford, UK). An 8-cm diameter Alderman-Grant RF coil tuned to the ^{3}He frequency was used. ^{3}He polarization was achieved by a spin-exchange optical pumping. End polarization levels between 20% and 30% were obtained (26). Ventilation images were acquired using a free breathing imaging protocol to avoid repeated animal's

intubation. A breathing mask was fitted on the rat's head and the animal was allowed to breathe freely from the ^{3}He reservoir during the 20 seconds image acquisition (27).

Pulmonary ventilation images using a radial sequence were acquired with an echo time (TE) of 1-ms which shows a good compromise between image quality and sensibility to simultaneously evaluate ventilation and lung susceptibility effects after iron containing CNT deposition (24). A total of 200 radial projections with 128 samples were acquired per image. The repetition time was 10 ms, the field of view (FOV) was 80 mm and a flip angle was 30°. Pulmonary imaging protocol was performed 24h, 7 days and 30 days after exposure. Pulmonary imaging protocol was performed 24h, 7 days and 30 days after exposure.

Image reconstruction and analysis:

Image reconstruction and analysis were carried out using IDL software (RSI, Boulder, CO). Ventilation images were reconstructed using a retrospective Cine approach (27) with the synchronization of the image acquisition with the breathing pattern of the animal. Each reconstructed ventilation image corresponded to a 100-ms time window.

For the measurement of the image signal-to-noise ratio (SNR) and coefficient of variation (CV) to assess the homogeneity of lung images, the maximal intensity grayscale image, corresponding to the end-inspiration breathing cycle, was selected to visualize the largest fraction of ventilation airspaces. A region of interest (ROI) encompassing the right and left lung was manually selected.

Proton lung MRI:

Acquisition:

Proton lung imaging was performed on a 10-cm bore actively-shielded 4.7 Tesla Bruker magnet (Bruker Biospin GmbH, Rheinstetten, Germany) interfaced to ParaVision software for preclinical MR imaging research. A Bruker transmission and reception proton volume RF coil was used providing good RF homogeneity over the volume of interest.

Gradient echo sequence (TR/TE=7/3.6ms) with the following parameters was used: field-of-view (FOV) 6x6 cm, flip angle 15°, matrix size 256x128, bandwidth 70 kHz and slice thickness of 1.5 mm. A single-slice image was obtained by computing the 2DFT of the averaged signal from 45 individual image acquisitions and interpolating the data set to 256 x 256 pixels. A tube containing gadolinium solution used as a reference was positioned on the rat chest to enable contrast-to-noise ratio (CNR) measurement and proton MR signal normalization.

Image analysis:

To monitor inflammation events in the lung, the number of hyper-intensity pixels (blood vessel and edema) was assessed in lung parenchyma using IDL software on the set of proton MRI images corresponding to each rat. Since the signals from injured lung regions and vessels were of comparable intensities, hyper-intensity pixels corresponding to the vessels were subtracted from the volumes determined on post-challenge images (14) and an average percentage increase in the set of axial images was calculated for each rat. The segmentation parameters were the same for all the analyzed images, chosen to segment regions corresponding to high intensity signals. Threshold was chosen to include all apparent fluid signal in lung parenchyma.

Lung histopathology:

At different investigation time points (table2), lungs were removed and fixed by filling with 4% para-formaldehyde (PFA) to an airway pressure of 25 cmH_2O. They were then dehydrated and embedded in paraffin. Five-µm transverse sections were cut (Leica 2045 microtome) and stained with hematoxylin-eosin-saffron (HES) for general morphology and the assessment of the dispersion of nanotubes.

HES is a routine staining which provides excellent contrast between elastic fibers, cytoplasm and connective tissues and allows assessing the integrity of the lung tissue and additionally localizing CNT aggregates which are detectable without any specific

coloration. The hematoxylin stains cell nuclei (dark blue), the eosin stains the cytoplasm (red), and the saffron stains collagen and connective tissue (yellow).

Transmission electron microscopy:

Small portion of lung corresponding to each group were removed and chemically fixed for conventional TEM. Briefly, specimen was immediately covered with 4% glutaraldehyde (GA) in 0.2M cacodylate buffer pH 7.4, cut in 1-mm^3 pieces and fixed for 2 hours at 4°C in the same fixative medium. Samples were then rinsed 3 times in 0.4M saccharose and 0.2M cacodylate buffer and postfixed for 2h in 2% osmium tetroxide in the same buffer after 1 night in vacuum bell jar. This procedure was followed by dehydration in graded ethanol and embedding in epon. Ultrathin sections were contrasted with methanolic uranyl acetate (30 min) and lead citrate (10 min) and observed under a 120 kV transmission electron microscope (JEOL JEM 1400, JEOL ltd) equipped with Gatan Orius CCD camera.

Statistical analyses:

All data are expressed as means ± SD. Non-parametric statistical tests (SPSS, SPSS Inc, Chicago, IL) were performed; Kruskal Wallis test for unpaired groups and Friedman test for comparison between time. A p value <0.05 was considered significant for all tests.

Results and discussion:

Owing to their widespread use and easy commercial availability, the supplied SWCNT (CNI® Buckytubes, Houston, TX) used in this study were produced by chemical vapor deposition (CVD) by means of the HiPco which is a commonly used technology in the manufacturing of SWCNT synthesized using a metal catalyst. Thus raw SWCNT usually contain significant amounts (10% wt in our case) of iron that may have the potential to cause additional toxic effects, but could also be detected *in vivo* using MRI (table1 and figure1). The lung is the prime target for SWCNT toxicity, as they can be inhaled during technologic processing and use. Intratracheal instillation (ITI) was preferred in our feasibility study because it is a reproducible administration technique in the lung allowing accurate control of the suspension dose administrated. Indeed, ITI is the most suitable technique for pulmonary absorption and deposition studies where dosage precision is of prime concern (28). When administrated by intra-tracheal instillation (ITI), the bolus of particle suspension enters deeper into rat lungs during breathing after hyperventilation.

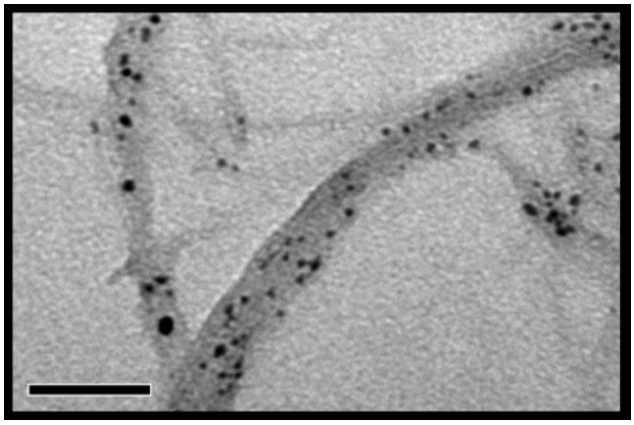

Figure1: Transmission electron micrograph of SWCNT showing the presence of impurities (black dots) and the structural shape of SWCNT bundles. Scale bar represents 50 nm.

In the current 3-months longitudinal study (measurements performed at day1 (D1), day7 (D7), day30 (D30) and day90 (D90)), rats were divided in different groups (table2) and received a single bolus (0, 0.1, 0.5 and 1mg) of SWCNT suspension. Upon the administration to the animals, carbon nanotubes powder was suspended in 150µl saline

solution (NaCl 0.9%) containing bovine serum albumin (BSA) to obtain a homogenous and better dispersed CNT solution after at least 10 minutes sonication in an ultrasonic bath (29).

Body weight was assessed throughout the experimental schedule to monitor the general health of the animals exposed to SWCNT. Upon instillation, and throughout the entire study, no unusual behavior or differences between groups were observed. Starting with a weight of 250±10g (n=36), the treated animals had a normal weight gain, weighing 540±6g (n=6) at the completion of the 3 months follow-up study, identical to controls.

HP-^{3}He MR imaging performed under free-breathing protocol (27) exhibited dose dependent hypo-intense and void signal regions in the short-term (D1) imaging period with a signal-to-noise (SNR) decrease and coefficient of variation (CV) increase ($p < 0.05$) observed in lung images (figure2).

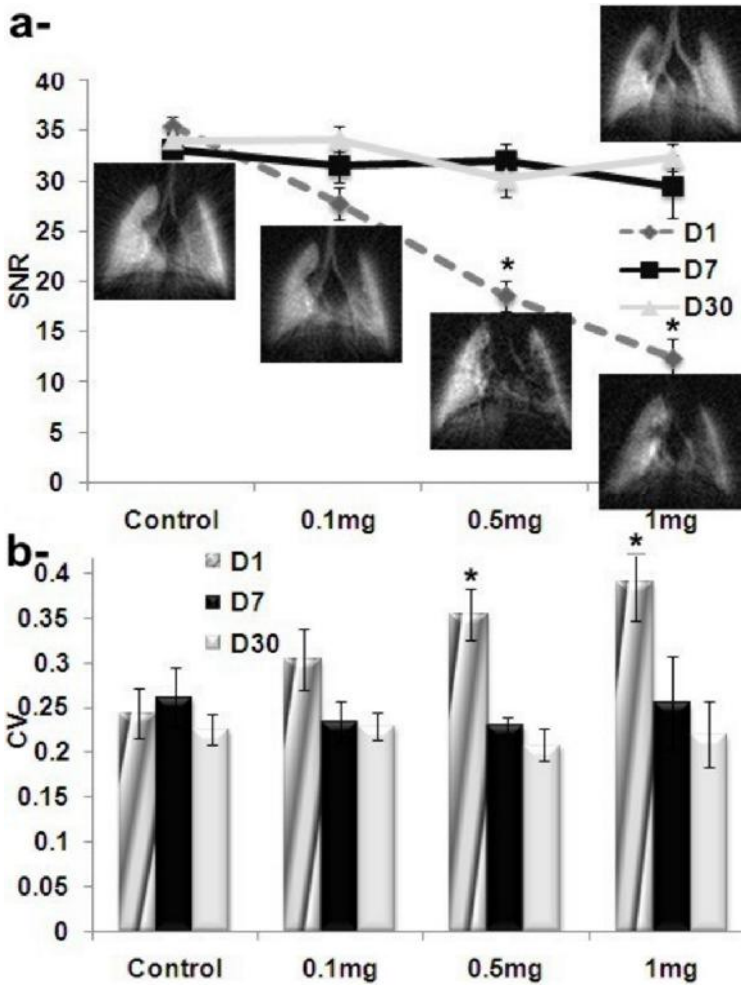

Figure2: a- Signal-to-noise ratio (SNR) variation of ^{3}He lung ventilation images for the different groups at D1, D7 and D30 with the corresponding images for all the groups (control, 0.1mg, 0.5mg and 1mg) at D1 and an example of 1mg instilled group at D30. b- Coefficient of variation (CV) for all the groups at different MRI protocol investigation time.: statistically different from control group ($p < 0.05$).*

At mid and long term investigations points (D7 and D30), HP ^{3}He lung images show homogeneous ventilation patterns with a SNR and CV statistically comparable to control images. The observed signal recovery with time might be related to SWCNT bundles encapsulation, homogenization of SWCNT distribution and incorporation of iron impurities in ferritin molecules or in hemosiderin deposits.

No ventilation defects were observed in the lung of all animals throughout the longitudinal study and no presence of SWCNT in systemic organs susceptible to accumulate or eliminate particles (liver, spleen and kidneys) was detected using systemic proton MRI and histopathology as showed in a previous study (25).

Pulmonary biodistribution and clearance of SWCNT with associated metal impurities (or more generally, any magnetically labeled nanoparticles) can be detected *in vivo* in the lung by noninvasive free-breathing HP ^{3}He MRI which can certainly help in research programs related to toxicological impacts of inhaled nanoparticles.

Proton lung MR imaging was also performed using a free-breathing protocol by image averaging technique providing sufficiently suppressed cardiac and respiratory motions artifacts and having the advantage of being less time consuming and more adapted for routine applications than cardio-respiratory triggered MR imaging (30).

One month after SWCNT exposition, proton MRI revealed the presence of some hyper-intensity pixels ($p < 0.05$) which can be related to small detectable inflammatory nodules in animal groups instilled with 0.5 and 1mg of SWCNT and in the same degree in the 0.5mg SWCNT instilled group after 3 months (figure3).

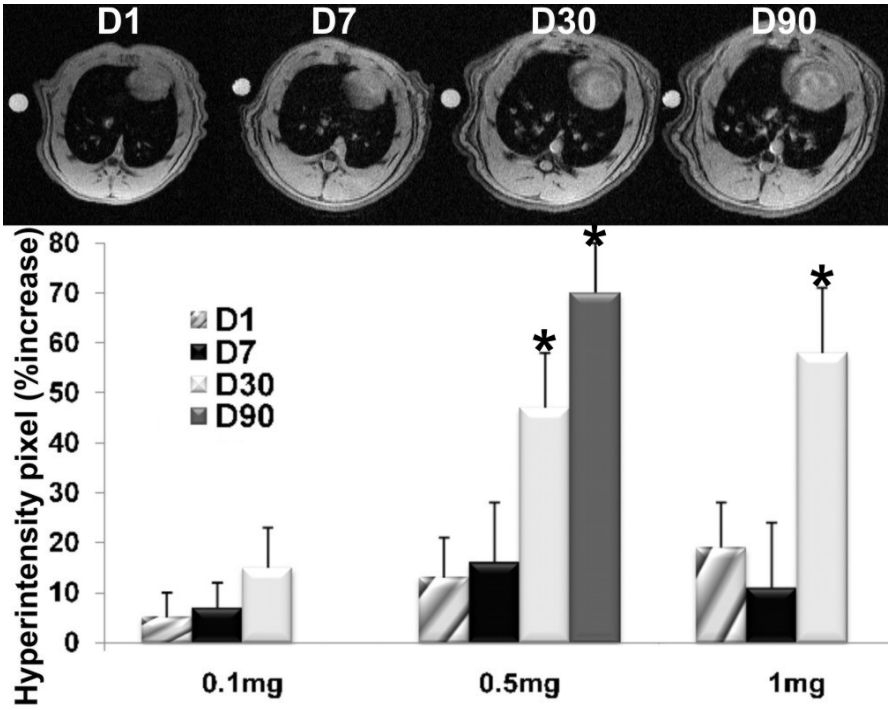

*Figure3: Top: MR images for 0.5mg instilled group at different investigation time at approximately the same slice position. Bottom: Histogram of hyper-intensity pixels (% increase per image) compared to control proton lung images showing an increase of hyper-signal pixels due to the presence of inflammatory regions at D30 and D90. *: statistically different from control group ($p < 0.05$).*

No presence of acute inflammatory effects induced by SWCNT presence in the pleura was detected using MRI (31).

Contrast-enhanced (CE) proton lung MRI can be very useful in assessing the presence of inflammatory nodules in the lung parenchyma and pleura and will be applied in future research. CE-MRI with its excellent contrast resolution can provide additional information to Computed Tomography (CT) considered the standard technique for assessing morphologic findings with it higher spatial resolution (32,33).

To provide an in-depth and complementary view on the biological impacts of CNT, lungs were carefully examined for tissue changes associated with nanotubes deposition and their

nanotoxicity at microscopic scale using light microscopy on HES stained histopathological lung slices (figure4).

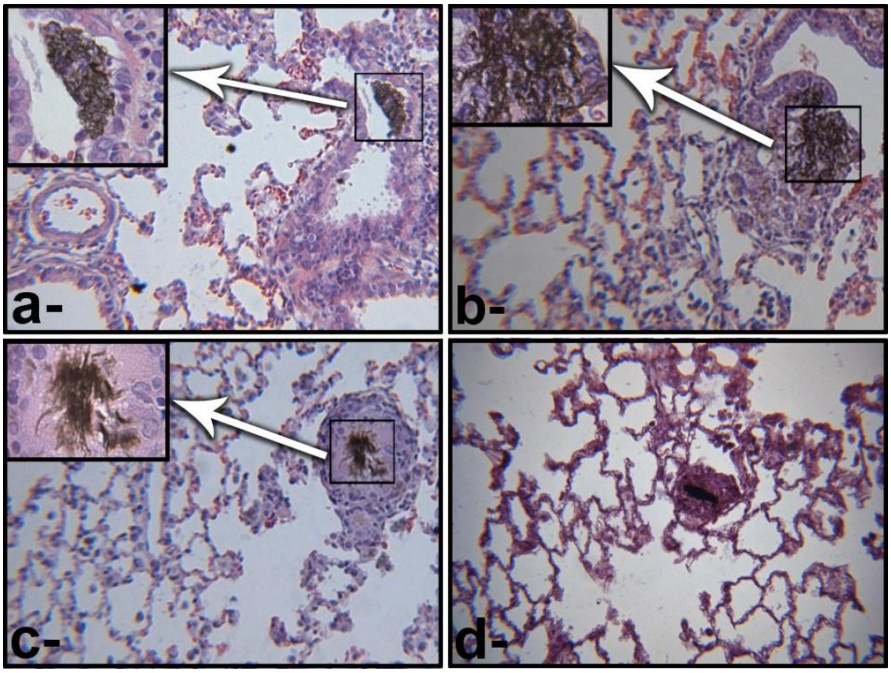

Figure4: Representative HES histopathological lung images after 0.5mg (2mg/Kg) intratracheal instillation of SWCNT in a rat model. Dose and time dependent inflammatory responses characterized by interstitial granulomas located beneath the bronchial epithelium were induced after SWCNT persistence. a- at early time point (D1), SWCNT were found in the lumen of bronchioles and alveoli without evidence of epithelial damage. b- at mid time point (D7), SWCNT aggregates tend to infiltrate neighboring lung interstitium inducing a mononuclear cell infiltrate. c- at long time point (D30), multifocal granulomatous reaction (giant cells) were present around the sites of SWCNT deposition. d- at very long time point (D90), granulomatous reaction persisted with SWCNT deposition, with membrane thickness and alveolar collapses presence.

Original magnification: x100 (x400 in zoomed regions).

At early stage time point (D1), SWCNT aggregates were found in the lumen of bronchioles and alveoli without evidence of epithelial damage or inflammation for all exposed doses (0.1, 0.5 and 1mg). An increased number of SWCNT was qualitatively correlated on light microscopic images with exposure concentrations.

Although the sonication and albumin addition have been taken into consideration before instillation to obtain homogenous distribution due to the poor solubility and Van der Walls interaction of the SWCNT, they tend to aggregate into clumps in bronchioles and alveoli.

At mid stage time point (D7), the alveolar septa became thicker and SWCNT aggregates forming a pellicle firmly adhering to bronchiolar wall tended to penetrate the wall and infiltrate neighboring lung interstitium, inducing a mononuclear cell infiltrate (figure4).

The effects persisted and progressed to give rise to multifocal granulomatous reaction containing macrophages, lymphocytes, fibroblasts, and collagen deposition around the sites of SWCNT deposition at the late stage investigation time point (D30) and in the same degree at the very late stage (D90) with membrane thickening and alveolar collapses presence due to SWCNT bio-persistence.

With the increase of the SWCNT dose, collagen deposition and pulmonary fibrosis which are typical features following inflammatory response became more severe. Pneumonitis, characterized by a peribronchiolar accumulation of polymorphonuclear neutrophils (PMN) and the appearance of granulomatous lesions, was observed in the different histopathological lung slices.

Even with the lowest exposition dose (0.1mg) corresponding to 0.4mg/kg, production of inflammatory response around the site of SWCNT deposition was observed in histological slices. This suggests a potential health hazard after SWCNT exposition.

The dose-dependent inflammatory responses observed at each time point after the SWCNT instillation in rats being the evidence of a foreign tissue body reaction is in accordance with different CNT-related studies (7,34-36).

No inflammatory process in the pleura was observed by means of the histopathological analysis, in agreement with the proton lung MR readouts.

SWCNT bundles encapsulation with the formation of multifocal granulomas observed 1-week after exposition might have resulted in preventing the SWCNT iron impurities from direct contact with HP gases in lung alveoli confirming the transient effect on SNR observed in HP ^{3}He MRI. The accentuation of inflammatory effects with collagen fiber deposition and giant cells formation 1-month after exposition can explain the hyper-intensity pixels observed in proton lung MRI.

Even histopathological analysis is limited in localizing non-aggregated SWCNT and assessing their biological effect at a sub-cellular level. SWCNT aggregates producing inflammatory granulomas may have different effects when more homogeneously distributed in the lungs after inhalation. The ultra-structural features of the lung tissue were observed by transmission electron microscopy which provides an ideal tool to analyze SWCNT-related sub-structural changes in the lung and understand the inflammatory process after SWCNT deposition.

At early time point, SWCNT reaching the gas-exchange region of the alveoli has been found to interact with surfactant proteins and alveolar proteinase or being exposed to different cells including alveolar epithelial type II (AT II) or alveolar macrophages (AM) (10). A significant increase of alveolar type II cells, the progenitor cells that replicate following alveolar type I cells' death, was detected (figure5).

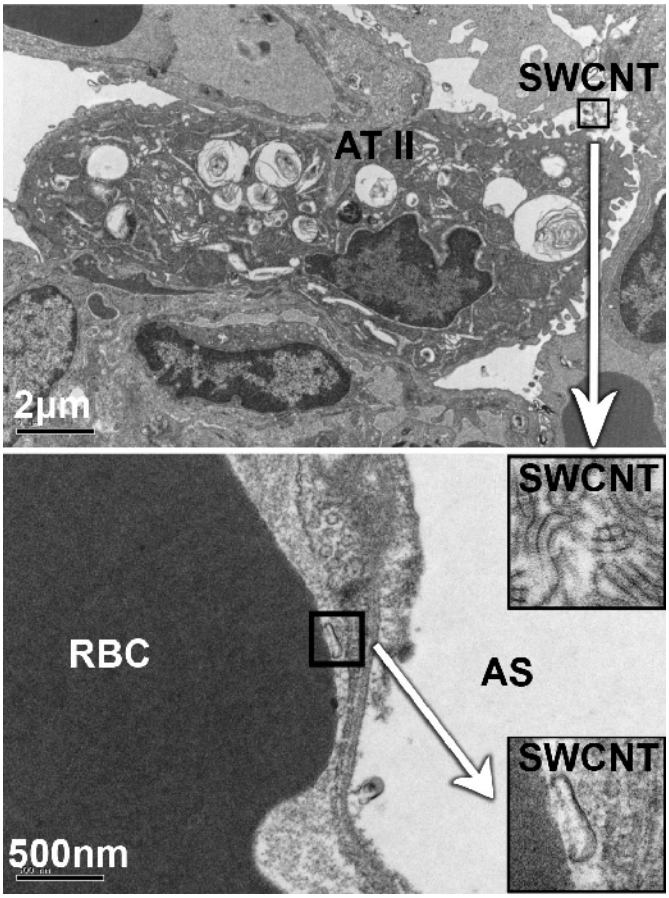

Figure5: TEM micrograph at early time point (D1) after 0.5mg (2mg/Kg) instillation of SWCNT showing: Top: SWCNT in interaction with surfactant proteins or alveolar proteinase (zoomed image) exposed to alveolar epithelial type II (ATII). Bottom: SWCNT traversing the wall of capillary vessel and in direct contact with a red blood cell. AT II: alveolar epithelial type II, RBC: red blood cell, AS: alveolar space.

Some of SWCNT instilled in the alveolar spaces could also have the potential to traverse the wall of the capillary vessels downstream and to "invade" other organs and be detected in liver, spleen and kidneys. However, such effect was not observed, as reported for the intrapulmonary instillation of 0.5mg of SWCNT in a previous study (25). Therefore, it can be assumed that the passage of intrapulmonary instilled SWCNT to the blood circulation is limited or their uptake by systemic organs is absent.

1-week after instillation, a significant increase in activated alveolar macrophages which form the first line of defense against foreign materials in many tissues and an activation of interstitial cells were detected in lung tissue around the site of SWCNT deposition (figure6).

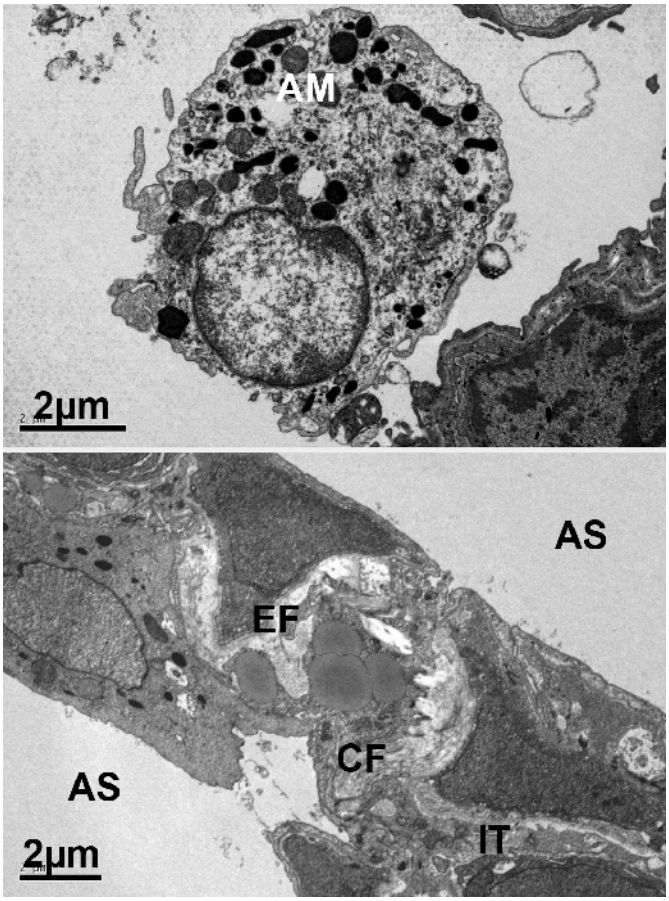

Figure6: TEM micrograph at mid time point (D7) after 0.5mg (2mg/Kg) instillation of SWCNT showing an activation of: Top: alveolar macrophages (AM) with SWCNT presence. Bottom: interstitial cells around the site of SWCNT deposition. AM: alveolar macrophage, AS: alveolar space, EF: elastic fibers, CF: collagen fibers, IT: interstitium.

At 1-month time point, an amplification of inflammatory reaction and a severe granulomatous lesion were assessed in transmission electron micrograph (figure7), in accordance with the giant cells detected with light microscopy. At the very late investigation time point, alveolar collapses and wall thickening with abundant alveolar macrophage activation were observed (figure8).

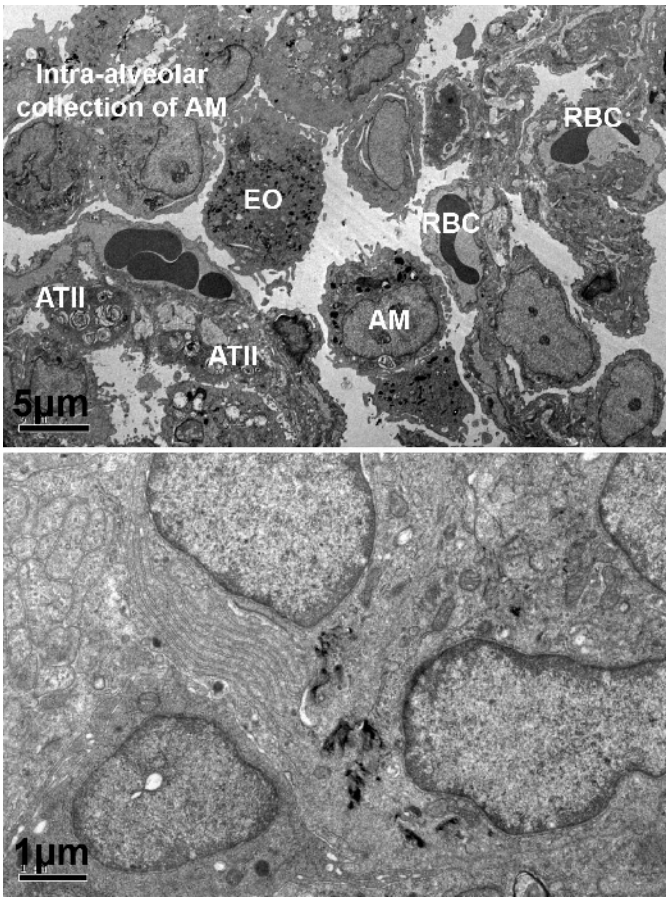

Figure7: TEM micrograph at late time point (D30) after 0.5mg (2mg/Kg) instillation of SWCNT showing an amplification of inflammatory reaction and severe granulomatous lesions characterized by the presence of: Top: an increased number of inflammatory cells (ATII, AM, EO). Bottom: collagen deposition with SWCNT persistence.

AT II: alveolar epithelial type II, AM: alveolar macrophages, EO: eosinophil, RBC: red blood cell.

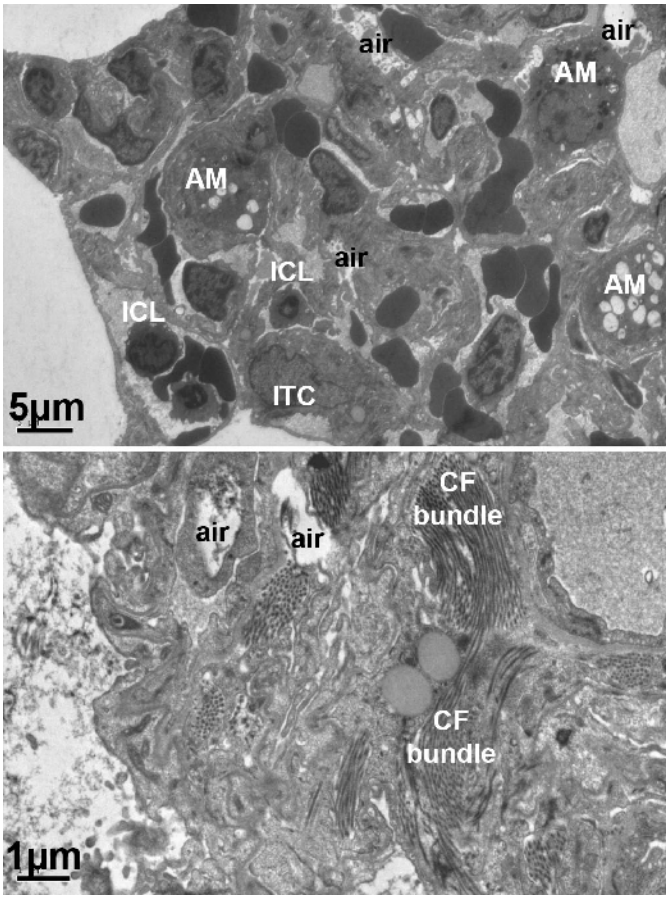

Figure8: TEM micrograph at very late time point (D90) after 0.5mg (2mg/Kg) instillation of SWCNT showing alveolar collapses and wall thickening with abundant alveolar macrophage activation and an emphysema-like phenotype.

AM: alveolar macrophages, ICL: intra-capillary lymphocyte, ITC: interstitial cell, CF: collagen fiber.

Conclusion:

Noninvasive HP ^{3}He and proton MRI combined to *ex vivo* optical and transmission electron microscopy represent powerful multimodality imaging techniques which allows full characterization of biodistribution and biological impacts of iron containing SWCNT.

After intrapulmonary instillation in a rat model, SWCNT was found to produce granulomatous and inflammatory reactions in a time and dose dependent manner. These findings in addition to SWCNT bio-persistence suggest an increased risk of developing lung cancer and the overall toxicity of these nanoparticles.

Similar studies have to be performed on different types of CNT or ultrafine related particles on different animal models and under different expositions conditions (i.e. inhalation) to obtain a comparable full characterization of their nanotoxicity and identify physicochemical properties that influence their deposition and potential health effect (i.e. fiber length, chemical stability, impurities …). Great caution when using and producing such nanomaterials are crucial to protect the individuals in direct contact with these materials and protection strategies to minimize human exposures should be implemented.

Grant sponsors:

This work was supported by the French ANR through RESPINTTOX project (SEST program), the French Ministry of Education and Research, and the European Union Marie Curie Research Training Network PHeLINet Contract number: MRTN-CT-2006-036002.

References:

1. Baughman RH, Zakhidov AA, de Heer WA. Carbon nanotubes--the route toward applications. Science (New York, NY 2002;297(5582):787-792.

2. Muller J, Huaux F, Moreau N, Misson P, Heilier JF, Delos M, Arras M, Fonseca A, Nagy JB, Lison D. Respiratory toxicity of multi-wall carbon nanotubes. Toxicology and applied pharmacology 2005;207(3):221-231.

3. Service RF. Nanotoxicology. Nanotechnology grows up. Science (New York, NY 2004;304(5678):1732-1734.

4. Oberdorster G. Pulmonary effects of inhaled ultrafine particles. International archives of occupational and environmental health 2001;74(1):1-8.

5. Mossman BT, Bignon J, Corn M, Seaton A, Gee JB. Asbestos: scientific developments and implications for public policy. Science (New York, NY 1990;247(4940):294-301.

6. Maynard AD, Aitken RJ, Butz T, Colvin V, Donaldson K, Oberdorster G, Philbert MA, Ryan J, Seaton A, Stone V, Tinkle SS, Tran L, Walker NJ, Warheit DB. Safe handling of nanotechnology. Nature 2006;444(7117):267-269.

7. Lam CW, James JT, McCluskey R, Hunter RL. Pulmonary toxicity of single-wall carbon nanotubes in mice 7 and 90 days after intratracheal instillation. Toxicol Sci 2004;77(1):126-134.

8. Chou CC, Hsiao HY, Hong QS, Chen CH, Peng YW, Chen HW, Yang PC. Single-walled carbon nanotubes can induce pulmonary injury in mouse model. Nano letters 2008;8(2):437-445.

9. Donaldson K, Aitken R, Tran L, Stone V, Duffin R, Forrest G, Alexander A. Carbon nanotubes: a review of their properties in relation to pulmonary toxicology and workplace safety. Toxicol Sci 2006;92(1):5-22.

10. Shvedova AA, Kisin ER, Mercer R, Murray AR, Johnson VJ, Potapovich AI, Tyurina YY, Gorelik O, Arepalli S, Schwegler-Berry D, Hubbs AF, Antonini J, Evans DE, Ku BK, Ramsey D, Maynard A, Kagan VE, Castranova V, Baron P. Unusual inflammatory and fibrogenic pulmonary responses to single-walled carbon nanotubes in mice. American journal of physiology 2005;289(5):L698-708.

11. Driehuys B, Hedlund LW. Imaging techniques for small animal models of pulmonary disease: MR microscopy. Toxicologic pathology 2007;35(1):49-58.

12. Albert MS, Cates GD, Driehuys B, Happer W, Saam B, Springer CS, Jr., Wishnia A. Biological magnetic resonance imaging using laser-polarized 129Xe. Nature 1994;370(6486):199-201.

13. Driehuys B, Cofer GP, Pollaro J, Mackel JB, Hedlund LW, Johnson GA. Imaging alveolar-capillary gas transfer using hyperpolarized 129Xe MRI. Proceedings of the National Academy of Sciences of the United States of America 2006;103(48):18278-18283.

14. Beckmann N, Tigani B, Ekatodramis D, Borer R, Mazzoni L, Fozard JR. Pulmonary edema induced by allergen challenge in the rat: noninvasive assessment by magnetic resonance imaging. Magn Reson Med 2001;45(1):88-95.

15. Tigani B, Schaeublin E, Sugar R, Jackson AD, Fozard JR, Beckmann N. Pulmonary inflammation monitored noninvasively by MRI in freely breathing rats. Biochemical and biophysical research communications 2002;292(1):216-221.

16. Karmouty-Quintana H, Cannet C, Zurbruegg S, Ble FX, Fozard JR, Page CP, Beckmann N. Bleomycin-induced lung injury assessed noninvasively and in spontaneously breathing rats by proton MRI. J Magn Reson Imaging 2007;26(4):941-949.

17. Lam CW, James JT, McCluskey R, Arepalli S, Hunter RL. A review of carbon nanotube toxicity and assessment of potential occupational and environmental health risks. Critical reviews in toxicology 2006;36(3):189-217.

18. Muhlfeld C, Rothen-Rutishauser B, Vanhecke D, Blank F, Gehr P, Ochs M. Visualization and quantitative analysis of nanoparticles in the respiratory tract by transmission electron microscopy. Particle and fibre toxicology 2007;4:11.

19. Lewin M, Carlesso N, Tung CH, Tang XW, Cory D, Scadden DT, Weissleder R. Tat peptide-derivatized magnetic nanoparticles allow in vivo tracking and recovery of progenitor cells. Nature biotechnology 2000;18(4):410-414.

20. Liu Z, Cai W, He L, Nakayama N, Chen K, Sun X, Chen X, Dai H. In vivo biodistribution and highly efficient tumour targeting of carbon nanotubes in mice. Nature nanotechnology 2007;2(1):47-52.

21. Liu Z, Davis C, Cai W, He L, Chen X, Dai H. Circulation and long-term fate of functionalized, biocompatible single-walled carbon nanotubes in mice probed by Raman spectroscopy. Proceedings of the National Academy of Sciences of the United States of America 2008;105(5):1410-1415.

22. Viallon M, Berthezene Y, Decorps M, Wiart M, Callot V, Bourgeois M, Humblot H, Briguet A, Cremillieux Y. Laser-polarized (3)He as a probe for dynamic regional measurements of lung perfusion and ventilation using magnetic resonance imaging. Magn Reson Med 2000;44(1):1-4.

23. Vignaud A, Maitre X, Guillot G, Durand E, de Rochefort L, Robert P, Vives V, Santus R, Darrasse L. Magnetic susceptibility matching at the air-tissue interface in rat lung by using a superparamagnetic intravascular contrast agent: influence on transverse relaxation time of hyperpolarized helium-3. Magn Reson Med 2005;54(1):28-33.

24. Al Faraj A, Lacroix G, Alsaid H, Elgrabi D, Stupar V, Robidel F, Gaillard S, Canet-Soulas E, Cremillieux Y. Longitudinal 3He and proton imaging of magnetite biodistribution in a rat model of instilled nanoparticles. Magn Reson Med 2008;59(6):1298-1303.

25. Al Faraj A, Cieslar K, Lacroix G, Gaillard S, Canet-Soulas E, Crémillieux Y. In Vivo Imaging of Carbon Nanotubes Biodistribution Using MRI. Nano letters 2008;In press.

26. Stupar V, Berthezene Y, Canet E, Tournier H, Dupuich D, Cremillieux Y. Helium3 polarization using spin exchange technique: application to simultaneous pulmonary ventilation/perfusion imaging in small animals. Investigative radiology 2003;38(6):334-340.

27. Stupar V, Canet-Soulas E, Gaillard S, Alsaid H, Beckmann N, Cremillieux Y. Retrospective cine 3He ventilation imaging under spontaneous breathing conditions: a non-invasive protocol for small-animal lung function imaging. NMR in biomedicine 2007;20(2):104-112.

28. Leong BK, Coombs JK, Sabaitis CP, Rop DA, Aaron CS. Quantitative morphometric analysis of pulmonary deposition of aerosol particles inhaled via intratracheal nebulization, intratracheal instillation or nose-only inhalation in rats. J Appl Toxicol 1998;18(2):149-160.

29. Elgrabli D, Abella-Gallart S, Aguerre-Chariol O, Robidel F, Rogerieux F, Boczkowski J, Lacroix G. Effect of BSA on carbon nanotube dispersion for *in vivo* and *in vitro* studies. Nanotoxicology 2007;1(4):266 - 278.

30. Beckmann N, Tigani B, Mazzoni L, Fozard JR. MRI of lung parenchyma in rats and mice using a gradient-echo sequence. NMR in biomedicine 2001;14(5):297-306.

31. Quintana HK, Cannet C, Schaeublin E, Zurbruegg S, Sugar R, Mazzoni L, Page CP, Fozard JR, Beckmann N. Identification with MRI of the pleura as a major site of the acute inflammatory effects induced by ovalbumin and endotoxin challenge in the airways of the rat. American journal of physiology 2006;291(4):L651-657.

32. Fujimoto K. Usefulness of contrast-enhanced magnetic resonance imaging for evaluating solitary pulmonary nodules. Cancer Imaging 2008;8:36-44.

33. Yamamuro M, Gerbaudo VH, Gill RR, Jacobson FL, Sugarbaker DJ, Hatabu H. Morphologic and functional imaging of malignant pleural mesothelioma. European journal of radiology 2007;64(3):356-366.

34. Liu A, Sun K, Yang J, Zhao D. Toxicological effects of multi-wall carbon nanotubes in rats. Journal of Nanoparticle Research 2008;10(8):1303-1307.

35. Muller J, Huaux F, Lison D. Respiratory toxicity of carbon nanotubes: How worried should we be? . Carbon 2006;44(6):1048-1056.

36. Carrero-Sanchez JC, Elias AL, Mancilla R, Arrellin G, Terrones H, Laclette JP, Terrones M. Biocompatibility and toxicological studies of carbon nanotubes doped with nitrogen. Nano letters 2006;6(8):1609-1616.

Manuscript IV

In vivo biodistribution and biological impacts of injected carbon nanotubes using MR techniques

Submitted manuscript

1. Preface:

As reported in manuscript 2, SWCNT with associated metal impurities can be noninvasively detected using susceptibility weighted proton MRI after their *in vivo* administration. In the previous manuscript the biodistribution and biological impact of intrapulmonary exposed SWCNT were found to produce granulomatous and inflammatory reactions in a time and dose dependent manner.

However, studies reported on well-dispersed and functionalized SWCNT were associated with much lower toxicity by improving their biocompatibility profile.

With their distinct architecture and their novel physicochemical properties, SWCNT hold promise for applications in nanomedicine field as contrast agents or target delivery carriers designed to improve the distribution and performance of drug molecules. When administered *in vivo*, their biodistribution and pharmacological profile have to be fully characterized.

In this manuscript, the biodistribution of various (pristine and functionalized) SWCNT were assessed in blood and target tissues after their intravenous administration by longitudinal *in vivo* MRI and their potential effect on liver metabolism by HR-MAS spectroscopy, a well-established technique for studying the endogenous metabolic changes caused by drug toxicity and disease processes. *Ex vivo* Raman spectroscopy, iron assay and histological analysis were performed to correlate with the MRI readouts.

2. Manuscript 4:

In vivo Biodistribution and Biological Impacts of Injected Carbon Nanotubes using MR techniques

Achraf AL FARAJ[1], Florence Fauvelle[2], Ghislaine Lacroix[3], Florence Lagarde[4], Cyrille Richard[5], Yannick Crémillieux[1], Emmanuelle Canet-Soulas[1]

1: Université Lyon1, Créatis-LRMN, CNRS UMR 5220, INSERM U630, Lyon

2: CRSSA, Biophysique Cellulaire et Moléculaire, Laboratoire de RMN, La Tronche

3: Institut National de l'Environnement et des Risques Industriels (INERIS), Verneuil-en-Halatte

4: Université Lyon1, Laboratoire des Sciences Analytiques, CNRS UMR 5180, Villeurbanne

5: Université Paris Descartes, Faculté de pharmacie, CNRS UMR 8151, INSERM U 640, Paris

Abstract:

Single-walled carbon nanotubes (SWCNT) hold promise for applications in nanomedicine field as contrast agents or target delivery carriers. When administered *in vivo*, their biodistribution and pharmacological profile have to be fully characterized. Tissue distribution of carbon nanotubes and potential impact on metabolism depend both on nanotubes shape, coating and metallic impurities. As standard radio- or fluorescently-labeled pharmaceuticals are not well suited for *in vivo* long term follow-up of carbon nanotubes, alternative methods were proposed and applied. Biodistribution and biological impacts of intravenously injected pristine (raw and purified) and functionalized SWCNT were assessed in a 2 weeks longitudinal study. Iron impurities allowed raw SWCNT *in vivo* detection by susceptibility-weighted Magnetic Resonance Imaging (MRI). A transitional accumulation in spleen and liver were observed by MRI. *Ex vivo* Raman spectroscopy, iron assays and histological analysis confirmed MRI readouts. Moreover, no acute toxicological effect on liver metabolic profile was observed using *ex vivo* High Resolution Magic Angle Spinning (HR-MAS). HR-MAS combined to pattern recognition methods (principal component and partial least squares-discriminant analysis) is a well-established technique for studying the endogenous metabolic changes caused by drug toxicity and disease processes.

Single-walled carbon nanotubes (SWCNT) with their unique nanometer-scale structure based on a single layer of carbon atoms arranged in a series of condensed benzene rings rolled-up into a tubular structure, and their fascinating mechanical, electric and thermal properties are more and more extensively used for different applications in nanotechnology (1). With their distinct architecture which allows them to selectively penetrate across biological barriers and their novel physicochemical properties in particular their high aspect ratio and propensity to functional modification, SWCNT hold promise for applications in nanomedicine field as contrast agents or target delivery carriers designed to improve the distribution and performance of drug molecules (2,3). For example, SWCNT have been shown to effectively shuttle various biomolecules into cells, including drugs, peptides, proteins, plasmid DNA, and small interfering RNA (4).

When administered *in vivo*, carbon nanotubes biodistribution and pharmacological profile have yet to be fully characterized for safe biomedical applications. Chemical modifications or functionalization of carbon nanotubes surfaces render them more hydrophilic which can improve their biocompatibility profile and reduce the aggregation of individual tubes through van der Waals forces.(5,6) In addition, in vitro studies reported on well-dispersed SWCNT were associated with lesser cytotoxicity when compared with the same SWCNT present in an agglomerated form (7,8).

Tissue distribution of carbon nanotubes and potential impact on metabolism depends on nanotubes shape, coating and metallic impurities (9).

Rather than relying on radiolabels or spectroscopic tags for indirect detection of carbon nanotubes, which may gradually dissociate from the materials or decay and lose activity over time, direct detection of carbon nanotubes can be performed based on their intrinsic physical properties, i.e. the intrinsic Raman scattering intensity of SWCNT (10) and their intrinsic near infrared (NIR) photoluminescence (11,12) which allow for their specific and direct detection. However these techniques are more adapted to *ex vivo* or *in vivo* investigations limited to surface due to poor penetration inside the body with the detection methods.

In a previous study, we have proposed an *in vivo* follow-up method to noninvasively detect SWCNT based on their metal impurity located at the surface or inside raw SWCNT (depending on the manufacturers and synthetic methods) using susceptibility-weighted Magnetic Resonance Imaging (MRI) (13). MRI has potential advantages over competing noninvasive modalities with respect to high soft-tissue resolution deep inside the body and discrimination in any imaging plane, and the lack of repeated exposure to ionizing radiation during longitudinal studies.

Among techniques to evaluate biological impact, NMR spectroscopy (MRS) is unique to get pertinent metabolic information about the target organs and biomarker metabolites (14). *In vivo* MRS, however, is often limited by its poor spectral resolution and sensitivity resulting in ambiguity in metabolite assignment and quantification. High-Resolution Magic Angle Spinning (HR-MAS) ^{1}H NMR enables setting up richer metabolite profiles of *ex vivo* tissues (biopsies) by providing much higher spectral resolution and sensitivity.

MAS NMR spectroscopy is a non destructive technique requiring small amounts and minimal sample preparation. It has been successfully applied to the analysis of biological samples such as brain, liver, kidney, intestine, cardiac tissue, and prostate. Pattern recognition methods (i.e. multivariate statistical methods) enable convenient visualization of spectral changes in NMR data and are useful for the detection of specific biomarkers of toxicity and for disease diagnosis (15-17).

In this 2-week follow-up study, we investigated the biodistribution of various SWCNT in blood and target tissues after their intravenous administration by longitudinal *in vivo* MRI and their potential effect on liver metabolism by HR-MAS spectroscopy after liver biopsy. *Ex vivo* Raman spectroscopy, iron assay and histological analysis were performed to correlate with the MRI readouts.

Three different types of SWCNT were used in this study: raw and purified pristine SWCNT were purchased from Carbon Nanotechnologies Incorporated (CNI® Buckytubes, Houston, TX). They have an individual diameter of 0.8 to 1.2 nm and an individual length of 0.1 to 1 µm according to the manufacturer. Pristine SWCNT were well-dispersed in NaCl in the presence of bovine serum albumin (BSA), after at least 20 minutes sonication in an

ultrasonic bath (18). Functionalized SWCNT (*f*-SWCNT) were initially purchased from Sigma Aldrich (Sigma, Lyon, France). They have an individual diameter of 1 to 2 nm and an individual length of 0.5 to 2 µm. The functionalization was achieved by suspending 60 mg of SWCNT in 20 ml of concentrated HNO_3 (15 M) and 60 ml of concentrated H_2SO_4 (18M). The mixture was stirred at 70°C for 2 hours. It was then filtered, washed with distilled water until the pH of the aqueous phase was neutral and then dried at 120°C for 12 hours. The oxidized materials were re-dispersed in water at a concentration of 3 mg/ml. This protocol was adapted from the article of Jie Liu, et al (19).

An ultrasmall supermagnetic iron oxide (USPIO) contrast agent Sinerem© (Ferumoxtran-10) kindly provided by Guerbet (Guerbet, Paris, France) was also included in this study as a positive control for contrast MRI. Sinerem is used for pre-clinical and clinical studies of inflammatory diseases. It has a mean particle diameter of 30 nm and consists of an iron oxide core coated with low molecular weight dextran (20) The lyophilized preparation was reconstituted with physiological saline to provide an initial iso-osmolar injectable suspension at 20 mg Fe/ml.

Prior to NP administration *in vivo*, their physicochemical properties were characterized by Raman spectroscopy and Inductively Coupled Plasma – Optical emission spectrometry (ICP-OES) for iron impurities dosage (Supporting Information). In vitro Raman spectra of SWCNT suspensions revealed very similar profiles with the presence of SWCNT characteristic peaks (Figure 1): RBM (radial breathing mode) features (appearing between 190 cm^{-1} and 254 cm^{-1}) which correspond to the atomic vibration of the C atoms in the radial direction, are very useful for characterizing nanotube diameters (21). The tangential graphene-like G-band (appearing at 1582cm^{-1} for R- and P-SWCNT and at 1578cm^{-1} for *f*-SWCNT) which gives information about the metallic character of the SWCNT in resonance, were used to detect nanotubes in solution and blood as it is relatively insensitive to the diameter and bundling of nanotubes and present a high Raman scattering intensity (10).

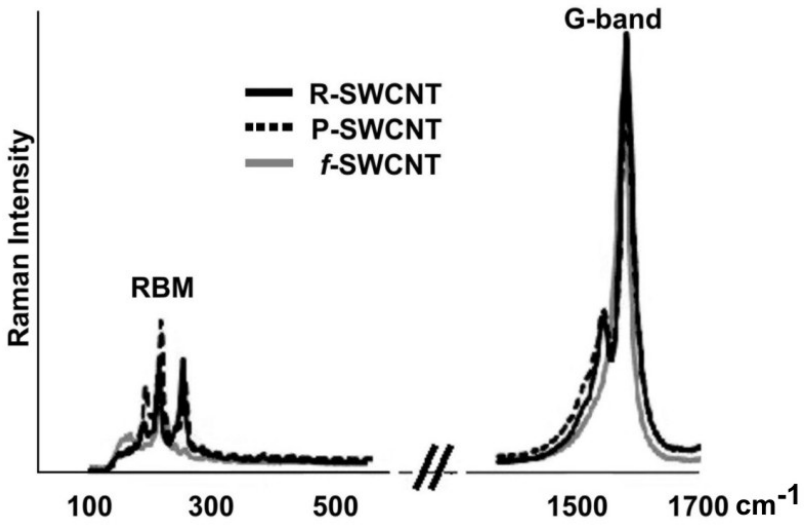

Figure1: Raman spectra of R-, P-, and f-SWCNT solutions showing the presence of SWCNT characteristic RBM and G-band features.

Following ICP-OES characterization of the prepared SWCNT solutions, it was found that the raw sample contain 11% (w/w) iron while the purified and functionalized samples contain 2% and 0.7% respectively.

Due to their strong magnetic moment, iron particles induce magnetic field inhomogeneities in their vicinity and attenuate the NMR signal of water molecules in surrounding tissues. With these contrast properties, R-SWCNT or iron-labeled SWCNT can be compared to iron-based MRI contrast agents used for noninvasive cellular and molecular imaging MRI characterization for the whole body (13).

To evaluate the presence of SWCNT in systemic organs, a gradient-echo imaging sequence sensitive to changes of susceptibility effect was used. Contrast-to-noise ratios (CNRs) measured in regions of interest, in liver, spleen, and kidneys, was chosen as an index of SWCNT deposition (for MR Imaging protocol, see Supporting Information).

Six- to eight-week old male Sprague-Dawley rats (n=40) were obtained from Charles River (L'Arbresle, France). Animals were housed in the Lyon-1 University animal-care unit, a facility accredited by the local veterinary authority. They had free access to conventional laboratory diet and water and were handled in accordance with official French guidelines

for the care and use of laboratory animals. Animals were anesthetized by intramuscular administration of 0.12 ml/100g of the following mixture: 3.5 ml of ketamine (1000 mg/ml), 3ml of xylazine (2%) and 1 ml of atropine (1mg/ml).

They were divided in 5 groups of 8 rats each: control injected with saline (C), raw (R), purified (P) and functionalized (*f*) SWCNT and Sinerem (S). Nanoparticles solutions (V= 150µl) were intravenously injected as a single bolus via the vein tail (0.5 mg / animal) and MR imaging protocol was performed at -1h and at 5h, 24h (D1), 48h (D2), 7 days (D7) and 14 days (D14) post-injection (p.i.) of nanoparticles, identically for each animal.

In the Sinerem injected group, a 2 to 3 fold decrease of CNR in the spleen and liver was observed up to 7 days p.i. and in the kidneys in the 5h imaging time point. This effect decreased gradually over the 2-week investigation study, however, CNR values were still statistically lower than those of control groups in the spleen and liver (figure2).

Similarly in the raw-SWCNT injected group, a 1 to 2 fold decrease of CNR was detected in the spleen up to 7 days p.i., in the liver up to 2days p.i. and in the kidneys up to 5h p.i. This effect decreased with time, and CNR values became comparable to control groups.

No statistical changes in CNR values were measured in the purified and functionalized SWCNT injected groups during the 2-week investigation (figure2).

These findings indicate that iron impurities can be used for the detection of R-SWCNT in systemic organs using standard proton MR techniques.

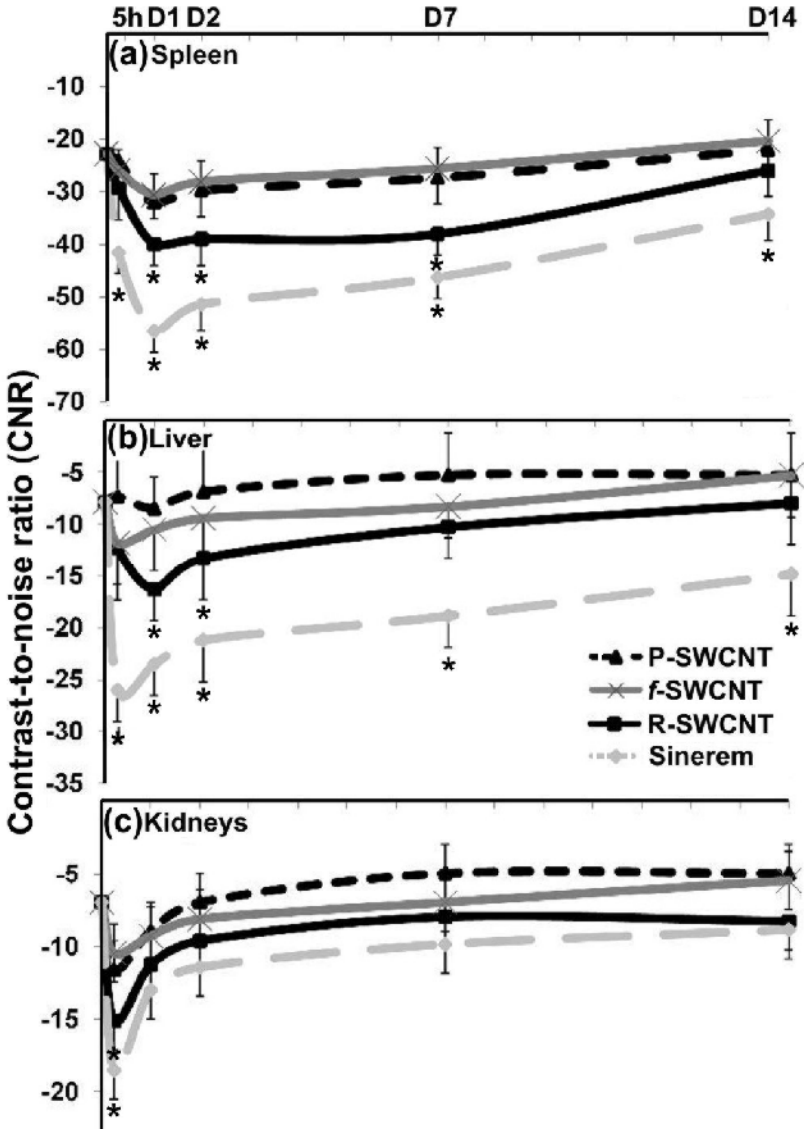

Figure2: CNR variation of Sinerem, raw (R-), purified (P-) and functionalized (f-) SWCNT injected groups compared to control values at 5h, D1, D2, D7 and D14 investigation time point in the (a) spleen, (b) liver, and (c) kidneys. Asterisks indicate statistically different values from the control group ($p < 0.05$).

After completion of the imaging studies, the same number of animals was sacrificed (n=4 per group) at D1 and D14 by exsanguination under isoflurane anesthesia. Spleen, liver, kidneys and blood were removed for different post-mortem *ex vivo* studies for blood Raman measurements, iron assay of rat organs and histopathological analyses protocols (see Supporting Information).

Raman spectroscopy measurements performed 24 hours after SWCNT injection on homogenized blood samples to detect the presence of nanotubes did not reveal the presence of the characteristic G-band with a similar profile as compared to control (data not shown). To increase the detection sensitivity of the presence of SWCNT in the blood, SERS technique was also used. SERS is a plasmonic effect where molecules adsorbed onto nano-roughened noble metal surfaces experience a dramatic increase in the incident electromagnetic field, resulting in high Raman intensities (22) Figure3 shows the spectra of the different blood samples and confirms the absence of SWCNT in the blood samples.

The absence of SWCNT in the blood 24h after injection is in accordance with different reported studies which showed that the blood circulation of SWCNT is limited to few hours (16h in maximum) and can vary with the type of nanotubes and their functionalization (10,23).

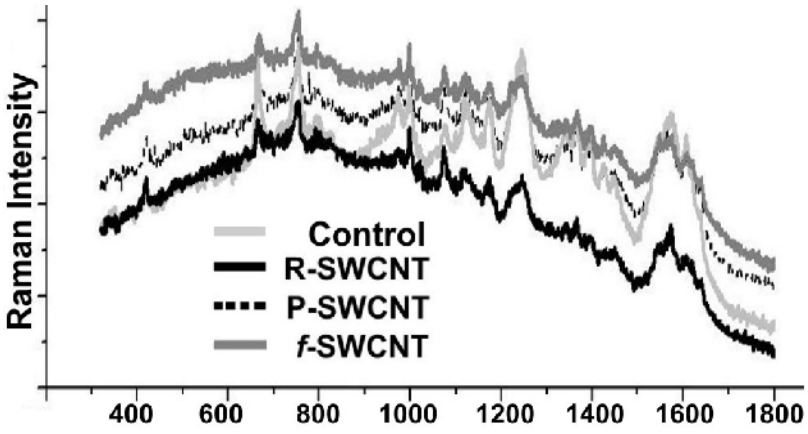

Figure3: Surface-enhanced Raman spectra of control, R-, P- and f-SWCNT blood samples at 24h p.i.

To obtain an estimation of the amount of injected nanoparticles recovered in different organs at D1 and D14 time points and correlate with MRI readouts, *ex vivo* quantification of iron by ICP-OES technique was used. Due to significant basal endogen iron concentration in organs as compared to the injected dose of iron, iron assay was only

performed in the spleen, liver, kidneys, lungs and blood for Control, Sinerem and R-SWCNT injected groups.

A statistically increase in iron was measured in the spleen and liver for both D1 and D14 Sinerem groups and for R-SWCNT D1 group (figure4) which is in accordance with the obtained CNR attenuation in the MR images (figure2).

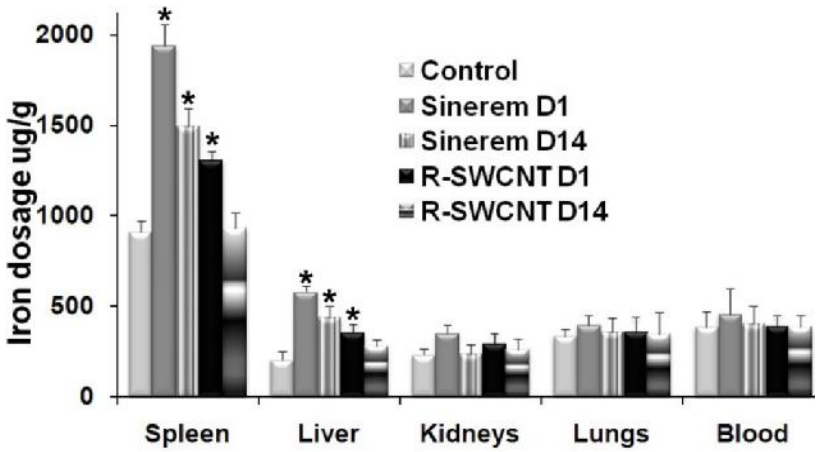

Figure4: Iron dosage in µg/g of spleen, liver, kidneys, lungs and blood for Control, Sinerem (D1 and D14) and R-SWCNT (D1 and D14) groups. Asterisks indicate statistically different values from the control group ($p < 0.05$).

Histopathological analyses were performed at D1 and D14 p.i. to correlate with the MRI readouts and to assess the integrity of tissue and localize the presence of SWCNT aggregates after i.v. injection. Due to Van der Waals forces, SWCNT bundle into ropes, which are further associated into loose aggregates and may be accessible for detection using light microscopy.

No histopathological changes or any signs of acute toxicological effects were observed in the different organs after the injection of both functionalized and well-dispersed pristine SWCNT. At D1 p.i., liver, spleen and lung slices show the presence of SWCNT and Sinerem small aggregates (figure5). No presence of SWCNT was detected 2 weeks after

injection. However Sinerem nanoparticles were still detectable in liver and spleen slices at that time point.

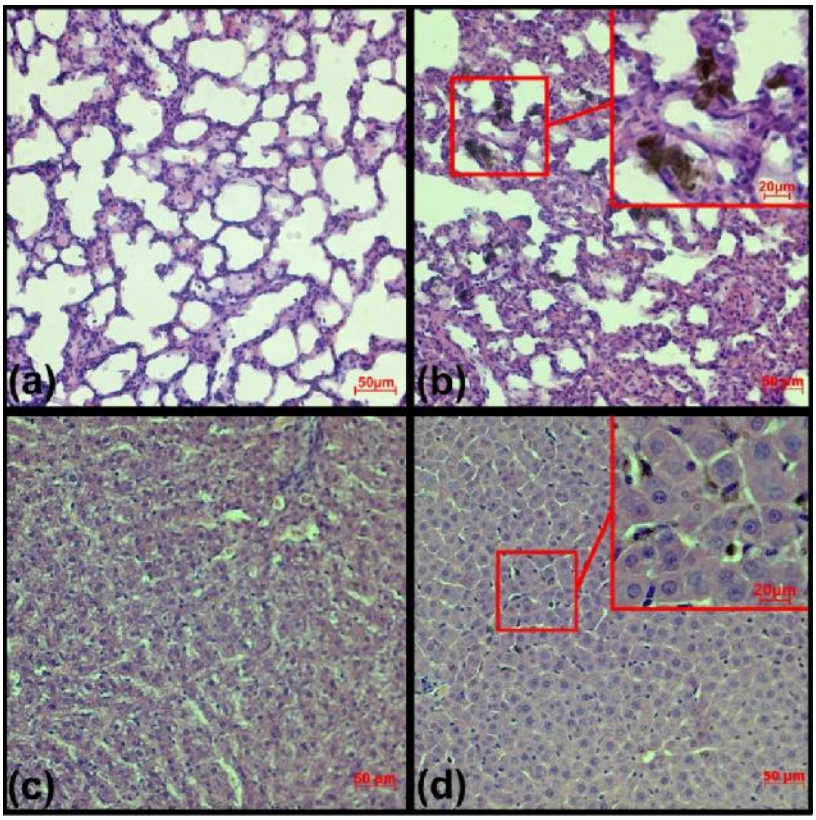

Figure5: Hematoxylin-Eosin-Saffron (HES) histopathological cuts of lung lobe (a: control, b: injected) and liver (c: control and d: injected) showing the presence of SWCNT aggregates after f-SWCNT injection at D1 investigation time point.

To monitor the general health of the animals, body weight was assessed throughout the experimental schedule. Upon SWCNT injection, and throughout the entire study, no unusual behavior or differences between groups were observed. Starting with a weight of 244±8g (n=32), the treated animals had a normal weight gain, weighing 336±7g at the completion of the 2-week follow-up study, identically to controls (n=8).

HR-MAS ^{1}H NMR is a well-established technique for studying the endogenous metabolic changes caused by drug toxicity and disease processes (24-26). It was performed in this

study to assess the biological impacts of SWCNT i.v. injection on the liver metabolism as a general index of toxicity (for HR-MAS NMR spectroscopy protocol, see Supporting Information). HRMAS ^{1}H NMR spectroscopy of intact tissue enables the simultaneous measurement of both lipids and low-molecular weight metabolites, which is important in a toxicological diagnosis. This approach is capable of detecting a wide range of metabolites in intact tissue, circumventing the need for extraction procedures that may introduce artifacts in the quantification of some metabolites and allowing the investigation of metabolic compartmentation within tissues.

A representative spectrum of intact control liver with the assigned peaks is shown in figure6a (bottom).

The main peaks arise from glucose, glycogen, trimethylamine-N-oxide (TMAO), and lipid moieties. Spinning tissue samples at high speed at the magic angle markedly improves spectral resolution and information content.

No variation was observed among the analyzed liver samples extracted from the different experimental groups (for HR-MAS data statistical analysis, see Supporting Information). Principal Component Analysis (PCA), the most used statistical method for the discrimination of variations in NMR spectra, did not reveal any differences between the analyzed liver samples with no clustering in PCA plot (figure6b) (R^2=0.84, Q^2=0.6).

Partial least squares-discriminant analysis (PLS-DA), a technique that generalizes and combines features from principal component analysis and multiple regression, was run to discriminate populations of rats by adding a supplementary data matrix containing our experimental group: D1 and D14. The size of groups being relatively small (based upon the kind of nanotubes injected), the sole effect of age could be tested. Therefore, no significant variation in liver metabolite was observed after SWCNT i.v. injection, but the classification allowed the clustering of spectra according to age (figure6c) (R^2=0.52, Q^2=0.47). Age metabolic profile evolution is not based on single metabolic variation, but rather on a global evolution of the spectrum due to age-related organ maturation (27).

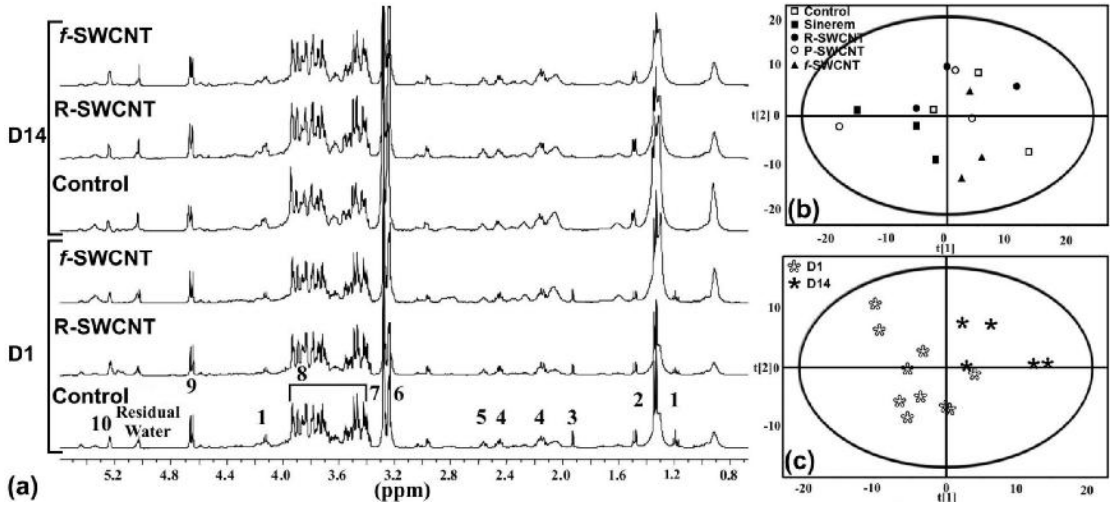

Figure6: a- One dimensional 400 MHz HR-MAS ^{1}H NMR spectra of liver sample acquired using CPMG pulse sequence. The numbers refer to the assignments of different peaks arising from the main metabolites (1: lactate, 2: alanine, 3: acetate, 4: glutamate/glutamine, 5: GSH (glutathione), 6: phosphocholine / glycerophosphocholine, 7: TMAO (trimethylamine oxide), 8: glucose/glycogen, 9: β-glucose, 10: α-glucose). b- Principal Component Analysis (PCA) score plot showing no clustering of liver samples from the different groups following HR-MAS ^{1}H NMR spectroscopy. c- Partial least squares-discriminant analysis (PLS-DA) score plot showing clustering between D1 and D14.

In conclusion, this study illustrates the potential of noninvasive MR imaging protocols for assessing longitudinally the biodistribution of SWCNT with associated intrinsic metal impurities. The same approach can be used to any other magnetically labeled nanoparticles. A transitional accumulation of raw SWCNT was detected in the spleen (up to D7), liver (up to D2) and kidneys (up to 5h). MRI readouts were correlated and confirmed by *ex vivo* Raman spectroscopy performed on blood samples as well as iron assay and histological analysis performed on different body organs.

No presence of acute toxicological effect on liver metabolism was observed after injection of both well-dispersed and functionalized SWCNT assessed using *ex vivo* High Resolution Magic Angle Spinning (HR-MAS) ^{1}H NMR. No clustering of NMR spectra was found using PCA (specific biomarkers of toxicity).

Acknowledgement:

The authors acknowledge V. Martinez for help in Raman spectroscopy.

References:

1. Baughman RH, Zakhidov AA, de Heer WA. Carbon nanotubes--the route toward applications. Science (New York, NY 2002;297(5582):787-792.

2. Ajayan PM, Tour JM. Materials Science: Nanotube composites. Nature 2007;447(7148):1066-1068.

3. Liu Y, Wang H. Nanomedicine: Nanotechnology tackles tumours. Nature nanotechnology 2007;2(1):20-21.

4. Liu Z, Chen K, Davis C, Sherlock S, Cao Q, Chen X, Dai H. Drug delivery with carbon nanotubes for in vivo cancer treatment. Cancer research 2008;68(16):6652-6660.

5. Lacerda L, Bianco A, Prato M, Kostarelos K. Carbon nanotubes as nanomedicines: from toxicology to pharmacology. Advanced drug delivery reviews 2006;58(14):1460-1470.

6. Sayes CM, Liang F, Hudson JL, Mendez J, Guo W, Beach JM, Moore VC, Doyle CD, West JL, Billups WE, Ausman KD, Colvin VL. Functionalization density dependence of single-walled carbon nanotubes cytotoxicity in vitro. Toxicology letters 2006;161(2):135-142.

7. Wick P, Manser P, Limbach LK, Dettlaff-Weglikowska U, Krumeich F, Roth S, Stark WJ, Bruinink A. The degree and kind of agglomeration affect carbon nanotube cytotoxicity. Toxicology letters 2007;168(2):121-131.

8. Raja PM, Connolley J, Ganesan GP, Ci L, Ajayan PM, Nalamasu O, Thompson DM. Impact of carbon nanotube exposure, dosage and aggregation on smooth muscle cells. Toxicology letters 2007;169(1):51-63.

9. Schipper ML, Nakayama-Ratchford N, Davis CR, Kam NW, Chu P, Liu Z, Sun X, Dai H, Gambhir SS. A pilot toxicology study of single-walled carbon nanotubes in a small sample of mice. Nature nanotechnology 2008;3(4):216-221.

10. Liu Z, Davis C, Cai W, He L, Chen X, Dai H. Circulation and long-term fate of functionalized, biocompatible single-walled carbon nanotubes in mice probed by Raman spectroscopy. Proceedings of the National Academy of Sciences of the United States of America 2008;105(5):1410-1415.

11. Welsher K, Liu Z, Daranciang D, Dai H. Selective probing and imaging of cells with single walled carbon nanotubes as near-infrared fluorescent molecules. Nano Lett 2008;8(2):586-590.

12. O'Connell MJ, Bachilo SM, Huffman CB, Moore VC, Strano MS, Haroz EH, Rialon KL, Boul PJ, Noon WH, Kittrell C, Ma J, Hauge RH, Weisman RB, Smalley RE. Band gap fluorescence from individual single-walled carbon nanotubes. Science (New York, NY 2002;297(5581):593-596.

13. Al Faraj A, Cieslar K, Lacroix G, Gaillard S, Canet-Soulas E, Cremillieux Y. In Vivo Imaging of Carbon Nanotube Biodistribution Using Magnetic Resonance Imaging. Nano Lett 2009.

14. Fischbach F, Bruhn H. Assessment of in vivo 1H magnetic resonance spectroscopy in the liver: a review. Liver Int 2008;28(3):297-307.

15. Wang Y, Bollard ME, Keun H, Antti H, Beckonert O, Ebbels TM, Lindon JC, Holmes E, Tang H, Nicholson JK. Spectral editing and pattern recognition methods applied to high-resolution magic-angle spinning 1H nuclear magnetic resonance spectroscopy of liver tissues. Analytical biochemistry 2003;323(1):26-32.

16. Holmes E, Cloarec O, Nicholson JK. Probing latent biomarker signatures and in vivo pathway activity in experimental disease states via statistical total correlation spectroscopy (STOCSY) of biofluids: application to HgCl2 toxicity. Journal of proteome research 2006;5(6):1313-1320.

17. Righi V, Durante C, Cocchi M, Calabrese C, Di Febo G, Lecce F, Pisi A, Tugnoli V, Mucci A, Schenetti L. Discrimination of healthy and neoplastic human colon tissues by ex vivo HR-MAS NMR spectroscopy and chemometric analyses. Journal of proteome research 2009.

18. Elgrabli D, Abella-Gallart S, Aguerre-Chariol O, Robidel F, Rogerieux F, Boczkowski J, Lacroix G. Effect of BSA on carbon nanotube dispersion for *in vivo* and *in vitro* studies. Nanotoxicology 2007;1(4):266 - 278.

19. Liu J, Rinzler AG, Dai H, Hafner JH, Bradley RK, Boul PJ, Lu A, Iverson T, Shelimov K, Huffman CB, Rodriguez-Macias F, Shon YS, Lee TR, Colbert DT, Smalley RE. Fullerene pipes. Science (New York, NY 1998;280(5367):1253-1256.

20. Jung CW, Jacobs P. Physical and chemical properties of superparamagnetic iron oxide MR contrast agents: ferumoxides, ferumoxtran, ferumoxsil. Magnetic resonance imaging 1995;13(5):661-674.

21. Jorio A, Pimenta MA, Filho AGS, Saito R, Dresselhaus G, Dresselhaus MS. Characterizing carbon nanotube samples with resonance Raman scattering. New Journal of Physics 2003;5:139-139.

22. Faulds K, Barbagallo RP, Keer JT, Smith WE, Graham D. SERRS as a more sensitive technique for the detection of labelled oligonucleotides compared to fluorescence. The Analyst 2004;129(7):567-568.

23. Liu Z, Cai W, He L, Nakayama N, Chen K, Sun X, Chen X, Dai H. In vivo biodistribution and highly efficient tumour targeting of carbon nanotubes in mice. Nature nanotechnology 2007;2(1):47-52.

24. Wei L, Liao P, Wu H, Li X, Pei F, Li W, Wu Y. Metabolic profiling studies on the toxicological effects of realgar in rats by (1)H NMR spectroscopy. Toxicology and applied pharmacology 2009;234(3):314-325.

25. Shi C, Wu CQ, Cao AM, Sheng HZ, Yan XZ, Liao MY. NMR-spectroscopy-based metabonomic approach to the analysis of Bay41-4109, a novel anti-HBV compound, induced hepatotoxicity in rats. Toxicology letters 2007;173(3):161-167.

26. Garrod S, Humpher E, Connor SC, Connelly JC, Spraul M, Nicholson JK, Holmes E. High-resolution (1)H NMR and magic angle spinning NMR spectroscopic investigation of the biochemical effects of 2-bromoethanamine in intact renal and hepatic tissue. Magn Reson Med 2001;45(5):781-790.

27. Espandiari P, Zhang J, Schnackenberg LK, Miller TJ, Knapton A, Herman EH, Beger RD, Hanig JP. Age-related differences in susceptibility to toxic effects of valproic acid in rats. J Appl Toxicol 2008;28(5):628-637.

3. Supporting Information:

Materials and methods:

Raman spectroscopy:

SWCNT samples were characterized by Raman spectroscopy. Volumes as low as 10µl of each sample were used to obtain the Raman signatures (RBM and G-band) of SWCNT using a labRAM ARAMIS micro-spectrometer Raman instrument (HORIBA Jobin Yvon Inc, Edison, NJ). Raman spectrum was recorded using a laser spot of 2µm^2 (6mW power on the sample, laser excitation wavelength = 632.5 nm), 50x objective and 10s collection time.

Iron dosage in SWCNT solutions and rat organs:

Iron metal impurities were measured in the different SWCNT solutions prior to their *in vivo* administration. 1ml of each solution was analyzed. Samples were centrifuged (30min, 10000rpm) and then mineralized at 200°C for 45 min with 7 ml nitric acid in a microwave oven (MarsXpress, Matthews, NC). Digested samples were diluted to 250 mL with ultrapure water (18 MΩ) and analyzed by Inductively Coupled Plasma – Optical emission spectrometry (ICP-OES) using a JY138 Ultrace instrument (HORIBA Jobin Yvon Inc, Edison, NJ) transformed into an axial view prototype, operating at 1075 W and equipped with a Meinhard type nebulizer and a Scott spray chamber. Detection was performed at 259.94 nm.

A portion of lung, liver, spleen and one kidney from the R-SWCNT and Sinerem groups of rats were also removed for iron assay using ICP-OES to correlate with noninvasive MRI measurements. Samples were dried at 80°C, weighed and then mineralized in 5 ml nitric acid and 2 ml hydrogen peroxide in the microwave oven (same conditions). Iron detection was carried out after dilution of the samples as described before.

MR Imaging protocol:

MR imaging was performed on a 10-cm bore actively-shielded 4.7T Bruker magnet (Bruker Biospin GmbH, Rheinstetten, Germany) interfaced to ParaVision software for preclinical MR imaging research. A Bruker transmission and reception proton volume RF

coil was used for good RF homogeneity over the volume of interest. Gradient echo sequence with TR/TE = 200/3.6, flip angle = 30°, FOV = 6 cm, 2 averages, and a pixel resolution of 234x234µm was used. Axial slices (thickness = 2mm) were positioned so as to image the organs of interest (ROIs) (liver, spleen and kidneys). A water tube used as a reference was positioned on the rat to enable contrast-to-noise ratio (CNR) measurement and proton NMR signal normalization.

Contrast-to-noise ratio (CNR) was defined as $CNR = \frac{(SNR_{ROI} - SNR_{ref})}{SNR_{ref}}$ with $SNR = \frac{Mean_{Signal}}{SD_{Noise}}$ where *ref* denotes the water tube reference and SD is the standard deviation of the noise in the image.

Within the liver, ROIs were drawn around apparent vascular structures and these regions subtracted out of the map to retain liver parenchyma only. ROIs encompassing the whole spleen and the two kidneys were manually selected for signal measurement.

MRI statistical analysis:

All data are expressed as means ± SD. Nonparametric statistical tests (SPSS, Chicago, IL) were done: Kruskal Wallis for unpaired groups and a Friedman test for comparison between different time points. A P value < 0.05 was considered significant for all tests.

Blood Raman measurements:

0.5ml of blood was sampled from the different rat groups sacrificed at 24h. It was then dissolved in equal volume of lysis buffer (1% SDS, 1% Triton X-100, 40 mM Tris acetate, 10 mM EDTA, 10 mM DTT) for detection of the SWCNT in the blood samples by Raman spectroscopy.

Surface enhanced Raman spectroscopy (SERS) technique was also used to enhance SWCNT Raman scattering (1,2). Volumes as low as 10µL of homogenized blood sample were putted on gold coated silicon surface (Mesophotonics United, Southampton, UK) to

enhance Raman signal and spectra were acquired using the same parameters as described above.

Histopathology:

For each rat in each of the group, a portion of the lung, liver, spleen and one kidney were removed for histological analysis. Organs were fixed in formaldehyde, dehydrated and embedded in paraffin. 5-µm transverse sections were cut (Leica 2045 microtome) and stained with hematoxylin-eosin (HE). HE is a routine staining method which provides excellent contrast between elastic fibers, cytoplasm and connective tissues and allows assessing the integrity of the tissue and additionally localizing SWCNT aggregates without any specific coloration.

HR-MAS NMR spectroscopy:

The liver tissue samples were analyzed by ^{1}H MAS NMR spectroscopy using a 9.4T (proton frequency 400.13 MHz) Bruker DRX Avance spectrometer (Bruker Biospin, Rheinstetten, Germany) equipped with a 4mm ^{1}H-^{13}C-^{31}P high-resolution magic-angle-spinning (HR-MAS) probehead. Approximately 15mg of frozen liver tissue (duplicata) sampled using a 3-mm biopsy punch were introduced in a 4mm zirconium oxide rotor and adjusted to 50 µl with a 1mM trimethylsilylpropionate (TSP) in D_2O solution. The rotor was then sealed and transferred into the pre-cooled probe. Samples were spun at 4 kHz and temperature was maintained at 4°C to prevent tissue degradation processes. One dimensional spectra were all acquired using a Carr-Purcell-Meiboom-Gill (CPMG) pulse sequence to attenuate macromolecule and lipid resonances, synchronized with the spinning rate (interpulse delay 250 µs, total spin echo time 30 ms). Residual water signal was presaturated during the 2 s relaxation delay time. Total acquisition of one spectrum with 256 scans lasted 16 minutes. Resonance assignment was performed as previously described by Waters et al (3).

HR-MAS data statistical analysis:

Data preprocessing: A 0.5Hz line broadening was applied to all data before Fourier transform. Data were phased and aligned on the TSP chemical shift (fixed to 0 ppm). Then

all spectral region between 4.65 and 0.5ppm were segmented in 0.02 ppm rectangular buckets using the Bruker software AMIX version 35.1 (Bruker, Wissembourg, France). Buckets were normalized to total intensity. The bucket tables (the X matrix) were then loaded in the SIMCA-P software version 10 (Umetrics, Umea, Sweden) and scaled to unit variance before PLS-DA analysis.

PCA and PLS-DA analysis: The unsupervised multivariate analysis PCA (principal component analysis) was carried out in a first step in order to find if NMR variables can discriminate SWCNT injected animals from control one. Then PLS-DA analysis was run by adding a supplementary data matrix Y, containing our experimental groups for a better discrimination of populations. All PLS-DA models were cross validated to allow evaluation of the statistical significance of the model. Cross validation lead to the calculation of the Q^2Y and R^2Y factors. Typically, a robust model has an $R^2>0.5$ and a $Q^2>0.4$.

All results will be visualized in this paper by scores plots.

References:

1. Nie S, Emory SR. Probing Single Molecules and Single Nanoparticles by Surface-Enhanced Raman Scattering. Science (New York, NY 1997;275(5303):1102-1106.

2. Faulds K, Barbagallo RP, Keer JT, Smith WE, Graham D. SERRS as a more sensitive technique for the detection of labelled oligonucleotides compared to fluorescence. The Analyst 2004;129(7):567-568.

3. Waters NJ, Holmes E, Waterfield CJ, Farrant RD, Nicholson JK. NMR and pattern recognition studies on liver extracts and intact livers from rats treated with alpha-naphthylisothiocyanate. Biochemical pharmacology 2002;64(1):67-77.

General Discussion and Conclusion

The rapid growth in research and development involving materials of nanoscale size has propelled nanotechnology to the forefront of science and technology development. With their novel properties, single-walled carbon nanotubes (SWCNT) have attracted a great deal of attention due to their expected industrial and biomedical applications.

However, the same novel properties that make them interesting raise concerns about their potential adverse effects on biological systems. The public health disaster associated with the use of asbestos fibers in the past highlights the importance of identifying rapidly the potential hazards of novel materials and the knowledge of SWCNT pathogenic mechanisms and nanotoxic effect is necessary to minimize the danger to exposed individuals (1).

Data on the toxicity of carbon nanotubes *in vivo* is poor and contradictory. Therefore, alternative ways to study their biodistribution and nanotoxicity *in vivo* after administration to living species are needed, in particular noninvasive imaging techniques relying on their intrinsic properties.

When noninvasive and longitudinal imaging investigations are considered, Magnetic Resonance Imaging (MRI) could be a method of choice. Magnetic Resonance Imaging has potential advantages over competing noninvasive modalities with respect to spatial and temporal resolution, the range and specificity of functional measures available, and the lack of repeated exposure to ionizing radiation during longitudinal studies.

Because of magnetic susceptibility due to the heterogeneity of microscopic structures (air-tissue interfaces) and because of their weak proton density, the lung remains a difficult organ to image with proton MRI. With the introduction of hyperpolarized (HP) gases (i.e., ^{3}He and ^{129}Xe) acting as contrast agents that diffuse rapidly to fill the airspaces of the lungs and allow visualization and measurement of the ventilated airways and alveolar spaces, pulmonary ventilation imaging is possible.

Schematically, there are two major situations in which people could be exposed to SWCNT: accidental respiratory exposure, essentially to an aerosol in the context of

SWCNT production and manipulation; and exposure as a result of SWCNT use for biomedical purposes.

Owing to their widespread use and easy commercial availability, as-synthesized SWCNT are more likely to be accidentally inhaled by workers or general public. These nanotubes usually contain particles of the transition metal catalyst that can play a major role in their toxicity, biodistribution, and properties, but could also be used for SWCNT noninvasive detection using MRI.

Due to their strong magnetic moment, iron particles induce magnetic field inhomogeneities in their vicinity and attenuate the NMR signal of water molecules in surrounding tissues. With these contrast properties, SWCNT can be compared to standard MRI contrast agents used for cellular and molecular imaging in whole body MRI.

To validate our approach in assessing noninvasively the biodistribution and biological impact of nanoparticles, ultra-small particle iron oxide (USPIO) nanoparticles were preferred in the first feasibility study.

Since the overall objective of this work concerned the investigation of accidental exposure to nanoparticles via the respiratory tract and since lung proton MRI has important limitations, noninvasive free-breathing hyperpolarized ^{3}He lung MRI protocol was implemented in this study complementary to proton systemic MRI protocol.

A dose range and a follow-up study of the USPIO distribution in lungs, liver, spleen, and kidneys using ^{3}He and proton MRI were reported. *In vivo* MRI findings were compared with *ex vivo* iron assay and histological analysis.

In ^{3}He lung imaging, an echo time (TE) of 1-ms using a radial sequence was shown to give a good compromise between image quality and sensibility to simultaneously evaluate ventilation and lung susceptibility effects after nanoparticles deposition.

Hypo-intense and void signal regions associated with intrapulmonary USPIO were observed in the ^{3}He ventilation images throughout the study, whereas no USPIO-related proton signal intensity changes were found.

This same approach was used to evaluate the biodistribution and biological impact of raw single-walled CNT (raw-SWCNT) and super-purified SWCNT (SP-SWCNT) after intrapulmonary exposition.

Prior to exposition, SWCNT physicochemical profiles were characterized with transmission electron microscopy (TEM) and inductively coupled plasma mass spectroscopy (ICP-MS) and show that raw-SWCNT sample contain 10% of iron impurities whereas SP-SWCNT sample was almost free of metal impurities.

In order to detect and semi-quantify the effects of SWCNT iron impurities, a multi-echo radial sequence was implemented to allow measurement of T2* values decrease (susceptibility effects) induced by these impurities.

The intrinsic metal impurities were large enough to induce a significant drop in magnetic field homogeneity in ^{3}He MR image and therefore the presence of SWCNT with associated metal impurities can be detected *in vivo* by noninvasive MR techniques. Hyperpolarized ^{3}He was used for the investigation of SWCNT pulmonary biodistribution while standard proton MR was performed for systemic investigation following injection of CNT solution.

In vivo detection of SWCNT with MRI as demonstrated in this work will be certainly applied in the future in research programs related to toxicologic impact of CNT and/or biomedical use of these nano-objects. The main advantage of this technique is that it can be applied to any type of iron-containing or iron-labeled nanoparticles without relying on specific properties of SWCNT (i.e. Raman scattering and Near Infrared photoluminescence).

However, the availability and the price of ^{3}He put a limitation to the widespread application of this technique. In addition, projection reconstruction of ^{3}He images does not allow a precise localization of nanoparticles in a single slice which can be obtained using multiple extraction of gaz. Current improvement in proton MRI sequences to obtain ultra-short echo time (few µs) can be very useful to detect iron containing nanoparticles by increasing the lung parenchyma MR signal (2).

The biodistribution and biological impacts of intrapulmonary instilled SWCNT were then assessed in a 3-months longitudinal study combining the potential of HP-^{3}He lung MRI in noninvasively monitoring SWCNT with associated metal impurities and proton lung MRI in assessing the eventual inflammatory processes after SWCNT deposition to *ex vivo* optical and electron microscopy at different investigation time points to provide an in-depth and complementary view.

The absence of lung parenchyma MR proton signal in combination with a background free of artifacts was shown to provide a high contrast-to-noise ratio for the detection of fluid secretion related to inflammation and edema or to collagen deposition and atelectasis (hallmarks of fibrosis).

Different doses of raw-SWCNT suspension were used to enable a dose dependent evaluation of the harmful effect of SWCNT pulmonary exposition.

After intrapulmonary instillation in a rat model, SWCNT was found to produce granulomatous and inflammatory reactions in a time and dose dependent manner. These findings in addition to SWCNT bio-persistence suggest an increased risk of developing lung cancer following inhalation of SWCNT and the overall toxicity of these nanoparticles.

However, efforts should be made to expose experimental animals under more realistic conditions (controlled inhalation exposure conditions) in order to verify the relevance of the inflammatory reactions observed in studies conducted by instillation (SWCNT aggregation). Similar studies have to be performed on different types of CNT or ultrafine related particles to identify the pathogenic mechanisms that influence their deposition and potential health effect (i.e. fiber length, chemical stability, impurities, dose…).

Based on the available literature and our results reported for one specific type of raw SWCNT, a number of additional factors are likely to influence the pulmonary toxicity of nanoparticles. These include the particle number and size distribution, their dose to target tissue, chemical surface modifications (functionalization) of engineered nanoparticles, the degree of agglomeration, their surface charge and electrostatic attraction depending on the method of particle synthesis, etc (3).

Although there are enormous differences between the lungs of rodents and human beings (4), great caution when using and producing such nanomaterials are therefore crucial to protect the individuals in direct contact with these materials and protection strategies to minimize human exposures should be implemented.

From biological impact evaluations after intrapulmonary exposition towards biomedical applications of single-walled carbon nanotubes, the recent bloom of chemical modification and functionalization methods has opened the path for their easy manipulation and processing in physiological environments (5,6). Equally important is the recent experimental demonstration that biological and bioactive species such as proteins, carbohydrates, and nucleic acids can be conjugated with carbon nanotubes.

With their distinct architecture which allows them to selectively penetrate across biological barriers and their novel physicochemical properties in particular their high aspect ratio and propensity to functional modification, single-walled carbon nanotubes hold promise for applications in nanomedicine field as contrast agents or target delivery carriers designed to improve the distribution and performance of drug molecules (7).

When administered *in vivo*, their biodistribution and pharmacological profile have to be fully characterized for safe biomedical applications. Tissue distribution of carbon nanotubes and potential impact on metabolism depends both on nanotubes shape, coating and metallic impurities.

The biodistribution of various (pristine and functionalized) SWCNT were assessed in blood and target tissues after their intravenous administration by longitudinal *in vivo* MRI and their potential effect was investigated on liver metabolism by High Resolution Magic Angle Spinning (HR-MAS) spectroscopy, a well-established technique for studying the endogenous metabolic changes caused by drug toxicity and disease processes. *Ex vivo* Raman spectroscopy, iron assay and histological analysis were performed to correlate with the MRI readouts.

Iron impurities allowed raw SWCNT *in vivo* detection by susceptibility-weighted MRI. A transitional accumulation of raw SWCNT was detected in the spleen (up to D7), liver (up to

D2) and kidneys (up to 5h). MRI readouts were correlated and confirmed by *ex vivo* Raman spectroscopy performed on blood samples as well as iron assay and histological analysis performed on different body organs.

No presence of acute toxicological effect on liver metabolism was observed after injection of both well-dispersed and functionalized SWCNT assessed using *ex vivo* HR-MAS ^{1}H NMR. No clustering of NMR spectra was found using PCA (specific biomarkers of toxicity). Albumin dispersion and carboxyl functionalization have been found to reduce considerably the harmful effect of intravenously injected SWCNT under the current study conditions.

The investigation of SWCNT use for biomedical purposes has just begun. As researchers gain greater control over the synthesis, purity, and functionalization of carbon nanotubes, it is reasonably likely that these materials will make their way into biomedical products (8).

References:

1. Mossman BT, Bignon J, Corn M, Seaton A, Gee JB. Asbestos: scientific developments and implications for public policy. Science 1990;247(4940):294-301.
2. Tyler DJ, Robson MD, Henkelman RM, Young IR, Bydder GM. Magnetic resonance imaging with ultrashort TE (UTE) PULSE sequences: technical considerations. J Magn Reson Imaging 2007;25(2):279-289.
3. Tsuji JS, Maynard AD, Howard PC, James JT, Lam CW, Warheit DB, Santamaria AB. Research strategies for safety evaluation of nanomaterials, part IV: risk assessment of nanoparticles. Toxicol Sci 2006;89(1):42-50.
4. Wallau BR, Schmitz A, Perry SF. Lung morphology in rodents (Mammalia, Rodentia) and its implications for systematics. J Morphol 2000;246(3):228-248.
5. Vairavapandian D, Vichchulada P, Lay MD. Preparation and modification of carbon nanotubes: review of recent advances and applications in catalysis and sensing. Anal Chim Acta 2008;626(2):119-129.
6. Lin Y, Taylor S, Li H, Fernando KAS, Qu L, Wang W, Gu L, Zhou B, Sun Y-P. Advances toward bioapplications of carbon nanotubes. Journal of Materials Chemistry 2004;14(4):527-541.
7. Liu Y, Wang H. Nanomedicine: Nanotechnology tackles tumours. Nat Nanotechnol 2007;2(1):20-21.
8. REY DA, BATT CA, MILLER JC. Carbon Nanotubes in Biomedical Applications. NANOTECHNOLOGY LAW & BUSINESS 2006;3(3).

Annex Studies

In collaboration with LAGEP (Laboratoire d'Automatique et de Génie de Procédés), Pharmaceutical Technology Department at the Université Lyon1, the longitudinal (r_1) and transverse (r_2) relaxivities of a biocompatible magnetic nanoparticles (MNP), PLLA (polyesters like polylactide) based super-paramagnetic nanoparticles were characterized in vitro using MRI (1) (figure1).

For the measurement of T_1 relaxation times, 2D imaging with an inversion-recovery fast imaging with steady state precession (IR-FISP) sequence was preferred. T_1 was calculated automatically from the data analysis of the Bruker system using the equation:

$Y = A + |C \times 1 - 2 \times e(-t/T_1)|$; where A is the absolute biais; C the signal intensity; T_1 is the spin lattice relaxation time.

For measurements of T_2 relaxation times, Multi Spin Multi Echo (MSME) sequences were used. Using Image J software (NIH), T_2 was calculated using a simplex algorithm to fit the values from each slice in a T_2 stack to the exponential equation:

$$\Delta S_n = S_0 exp^{\frac{-TE_n}{T_2}}$$

Relaxivities (r_1 and r_2) are generally defined as the slope of the linear regression generated from a plot of the measured relaxation rate ($1/T_i$, where i = 1, 2) versus the concentration of the particles. $(1/T_i) = (1/T_{i(0)}) + r_i[MNP]$ where Ti denotes the longitudinal (T_1) or transverse (T_2) relaxation times of a suspension containing the particles and Ti(0) is the relaxation time of the solvent (water) without particles.

T_1 and T_2 relaxivities of these MNP (4.7 T, 20°C) were 1.7±0.1 and 228.3±13.1 s^{-1} mM^{-1}, respectively, rendering them in the same category of known negative contrast agents which shorten the T_2 relaxation time. Therefore, by using an appropriate anticancer drug in their formulation, these magnetic nanoparticles can present a promising mean for simultaneous tumor imaging, drug delivery and real time monitoring of therapeutic effect.

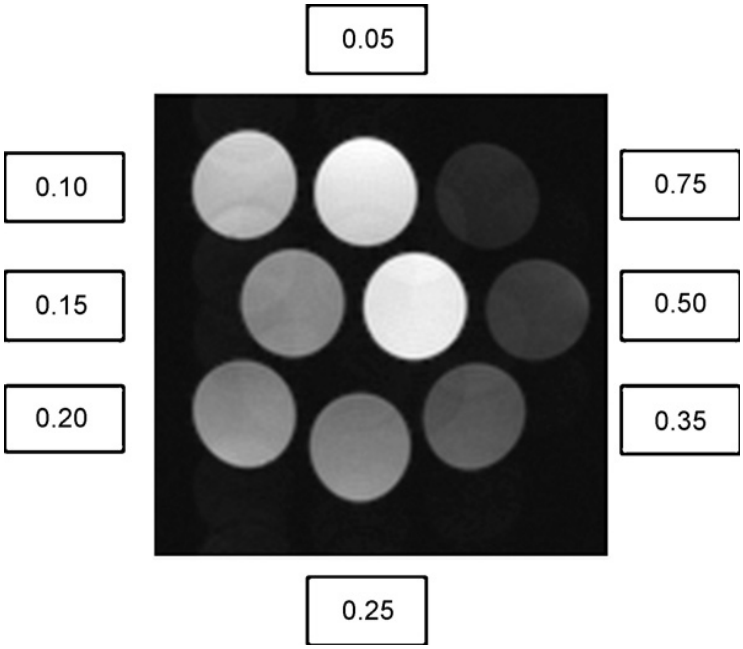

Figure1: T_2-weighted image of MNP at different iron concentrations (mM). The tube in the centre has 0% mM iron. Reproduced with permission from (1).

In another study (2), elaborated superparamagnetic non radioactive nanoparticles were loaded with $Re_2(CO)_{10}$ (dirhenium decacarbonyl) and oleic-acid coated magnetite as novel interesting candidate for local intra-tumoral radiotherapy. In a feasibility MRI study, these nanoparticles were injected into a mice animal model via Targeted Multi Therapy (TMT) technique.

Nanoparticles suspension has been prepared at a metallic iron concentration of 0.25 mMol which was estimated to be sufficient to allow following the local distribution of these nanoparticles being loaded with magnetite; a MRI negative contrast.

MR imaging was carried out on a 4.7T Bruker magnet immediately after injection (D_0), the next day (D_1) and three days after (D_3) using a gradient echo sequence (TR/TE = 200/5 ms; 30° flip angle) at a resolution of 390x390 µm with four excitations to obtain a good signal-to-noise ratio. Gadolinium tubes (103 µM) positioned horizontally to mice were used to normalize the signal and allow a proper contrast-to-noise ratio analysis. Coronal slices (slice thickness=2mm) were positioned in order to image both mice legs and the gadolinium tubes.

Contrast to noise ratio (CNR) was calculated using Creatools software (Créatis-LRMN, France) in a region of interest (ROI) where nanoparticles were located to compare and quantify their negative effect on MRI signal. The applied equation to calculate (CNR) was:

$$CNR = \frac{(SNR_{Muscle} - SNR_{ROI})}{SNR_{Muscle}} \text{; with } SNR = \frac{Mean_{Signal}}{SD_{noise}}$$

where CNR, contrast to noise ratio; SNR, signal to noise ratio; S.D., standard deviation; ROI, region of interest where nanoparticles were located in D_0. This region was propagated in the other days and in the muscle of mice right leg.

Nanoparticles have been successfully injected via the TMT technique with a strong negative contrast area detected in the left leg (the point of injection) (figure2). Furthermore the high pressure of injection has allowed obtaining a localized nanoparticles zone useful to obtain a radioactive zone of nanoparticles in the interior of tumour for future investigations.

These super-paramagnetic nanoparticles were still localized preciously 24 hours after injection however their negative contrast was clearly lower three days after injection which can be explained by their elimination via the lymphatic network out from the injection area.

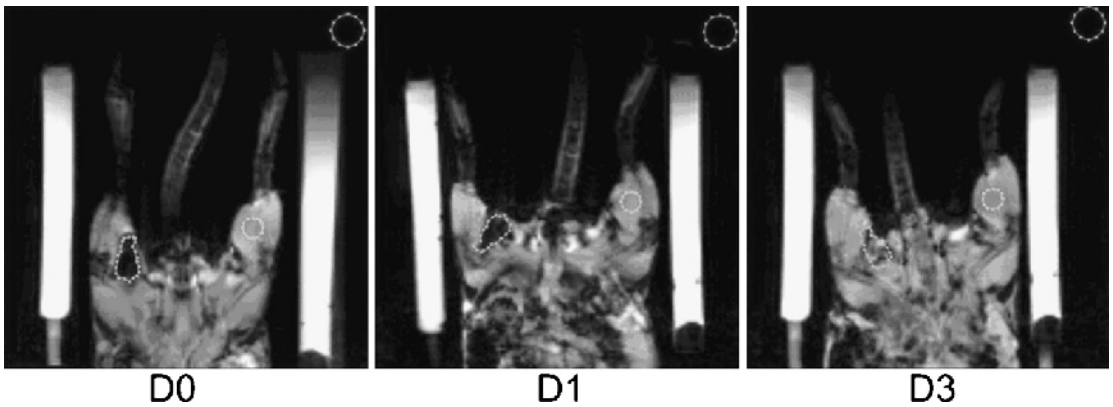

Figure: MRI images of the two legs of a mice immediately (D_0), one day after (D_1) and three days after (D_3) injection of non radioactive superparamagnetic $Re_2(CO)_{10}$ nanoparticles (0.25mM iron). Reproduced with permission from (2).

During this same MR imaging protocol, the positive contrast MRI was tested using the gradient compensation method for the detection of a novel super-paramagnetic nanosystem designed for local radiation therapy (3). Iron oxide based particles with super-paramagnetic properties are extremely strong contrast enhancers for proton MR imaging.

In vivo images were acquired for this respect in coronal sections using a T2*-weighted gradient echo sequence: TR/TE= 10/300 ms; flip angle = 25°; matrix of 256 x 256; slice thickness, 1.11 mm; spatial resolution of 234μm × 234μm; number of averages = 1. (figure3). For positive contrast, the rephasing gradient amplitude was modified.

The gradient compensation method for positive contrast MRI was shown to be effective at relatively high field strength and it offers additional information to standard negative contrast. Furthermore, it allowed the *in vivo* follow-up of contrast enhancement variation. However, this technique does not provide anatomical information and thus should be used in complement to standard T2*-weighted imaging, in order to obtain a multi-contrast type approach for *in vivo* iron characterization.

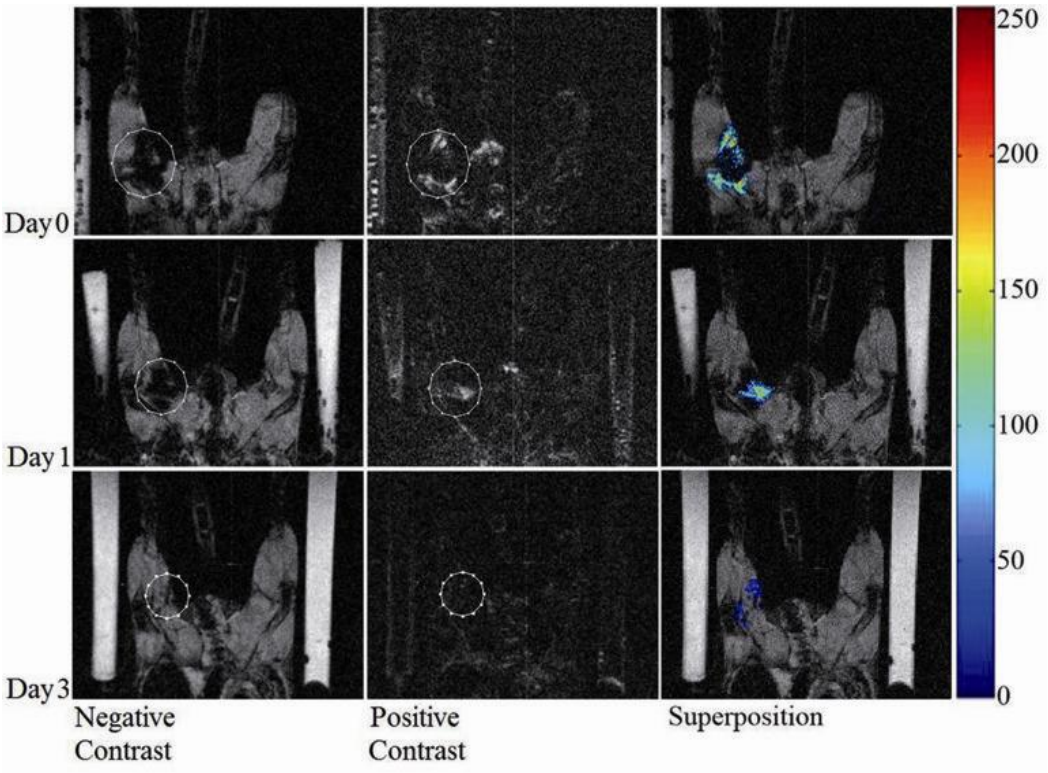

Figure3: T2-weighted gradient echo images obtained from one animal during the longitudinal study, showing signal evolution over time, from immediately after nanoparticles administration (Day 0) to Day 3, respectively with the standard negative contrast (left column) and the positive contrast (middle column) of the same image slice. Gradient compensation leads to the appearance of bright spots at the injection site (circle). The images on the right show the superimposition of the injection site and the bright signal regions. Reproduced with permission from(3).*

Within the framework of Phelinet (Polarized Helium Lung Imaging Network), the HYPR (HighlY constrained backPRojection) algorithm was implemented for small animal studies, aimed at increasing the temporal resolution of ^{3}He ventilation imaging for multiple inspirations protocols experiments. Rats were chosen as animal model as their breathing rate is about 5 times higher than that of humans, therefore a temporal resolution of the order of tens of milliseconds is desired.

The results presented in this study demonstrate the feasibility of using the HYPR technique for ^{3}He ventilation protocols in small animals. Series of high quality HYPR images were obtained for multiple inspirations protocols (4). Although the multiple inspiration experiment was performed under free breathing conditions, it would be possible as well to apply this technique if the gas is to be administrated by means of a mechanical ventilator.

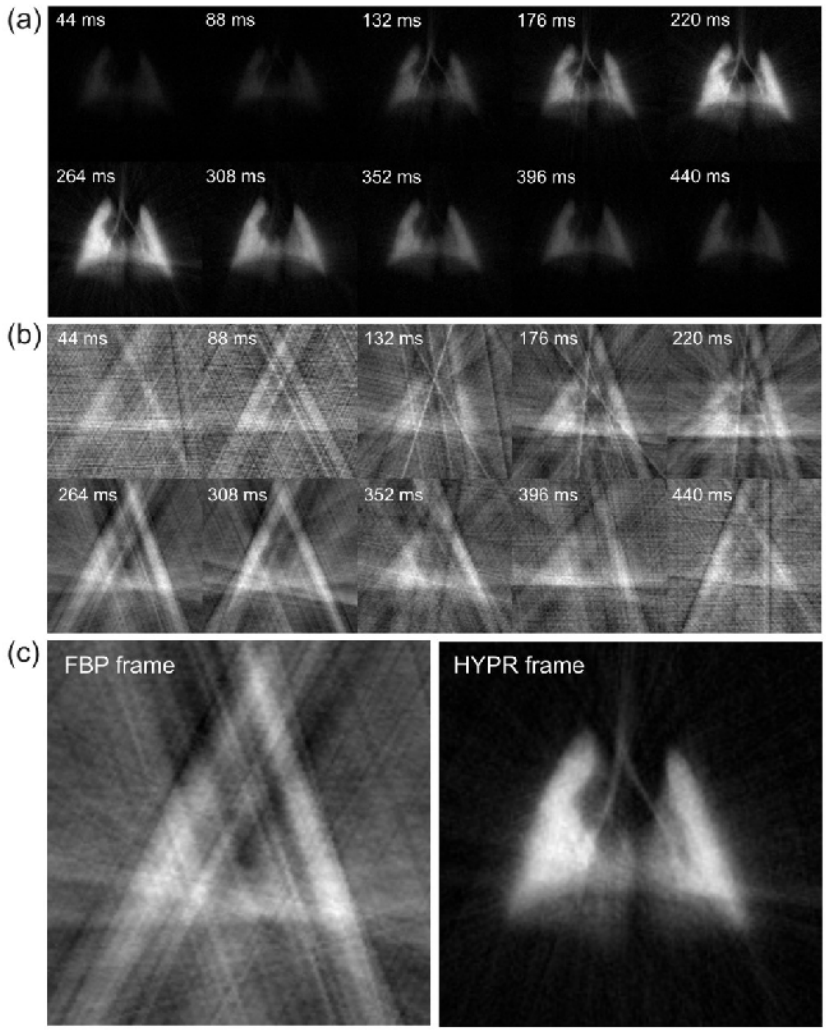

Figure4: Multiple inspirations protocol in a healthy animal. Comparison of the HYPR frames (a) and the filtered backprojection images (b) reconstructed using 8 radial projections per frame. Individual retrospective CINE composite images were used for each phase of the breathing phase in case of the HYPR frames. In part (c) the enlarged HYPR frame at maximum inspiration is compared to the corresponding filtered backprojection image. Reproduced with permission from(4)

References:

1. Hamoudeh M, **Al Faraj A**, Canet-Soulas E, Bessueille F, Leonard D, Fessi H. Elaboration of PLLA-based superparamagnetic nanoparticles: characterization, magnetic behaviour study and in vitro relaxivity evaluation. International journal of pharmaceutics 2007;338(1-2):248-257.

2. Hamoudeh M, Fessi H, Mehier H, **Al Faraj A**, Canet-Soulas E. Dirhenium decacarbonyl-loaded PLLA nanoparticles: influence of neutron irradiation and preliminary in vivo administration by the TMT technique. International journal of pharmaceutics 2008;348(1-2):125-136.

3. Sigovan MO, Hamoudeh M, **Al Faraj A**, Fessi H, Canet-Soulas E. Positive Contrast with Therapeutic Nanoparticles at 4.7T. submitted manuscript.

4. Cieślar K, **Al Faraj A**, Stupar V, Gaillard S, Crémillieux Y. HYPR method for increasing the performance of dynamic 3He MR ventilation imaging in rats. submitted manuscript.

Articles in International Journals

1. **A. Al Faraj**, G. Lacroix, H. Alsaid, D. Elgrabi, V. Stupar, F. Robidel, S. Gaillard, E. Canet-Soulas, and Y. Crémillieux: *Longitudinal 3He and Proton imaging of magnetite biodistribution in a rat model of instilled nanoparticles.* **Magnetic Resonance in Medicine 59:1298-1303 (2008).**

2. **A. Al Faraj**, K. Cieslar, G. Lacroix, S. Gaillard, E. Canet-Soulas, and Y. Crémillieux: *In Vivo Imaging of Carbon Nanotube Biodistribution using Magnetic Resonance Imaging*. **Nano Letters 2009, 9 (3), 1023-1027.**

3. **A. Al Faraj**, A. Bessaad, K. Cieslar, S. Peyrol, G. Lacroix, E. Canet-Soulas, and Y. Crémillieux: *Single-walled carbon nanotubes detection and evaluation of impact using multimodality imaging techniques in a 3-months follow-up study*. **Submitted manuscript.**

4. **A. Al Faraj**, F. Fauvelle, G. Lacroix, Y. Crémillieux, and E. Canet-Soulas: *In vivo biodistribution and biological impacts of injected carbon nanotubes*. **Submitted manuscript.**

5. M. Hamoudeh, **A. Al Faraj**, E. Canet-Soulas, F. Bessueille, D. Léonard and H. Fessi: *Elaboration of PLLA-based superparamagnetic nanoparticles: Characterization, magnetic behaviour study and in vitro relaxivity evaluation.* **International Journal of Pharmaceutics**, Volume 338, Issues 1-2, 29 June **2007**, Pages 248-257

6. M. Hamoudeh, H. Fessi, H. Mehier, **A. Al Faraj**, E. Canet-Soulas: *Dirhenium decacarbonyl-loaded PLLA nanoparticles: Influence of neutron irradiation and preliminary in vivo administration by the TMT technique.* **International Journal of Pharmaceutics**, Volume 348, Issues 1-2, 4 February **2008**, Pages 125-136

7. K. Cieslar, **A. Al Faraj**, V. Stupar, S. Gaillard, Y. Crémillieux: *HYPR method for increasing the performance of dynamic 3He MR ventilation imaging in rats*. **Submitted manuscript.**

8. M. Sigovan, M. Hamoudeh, **A. Al Faraj**, H. Fessi, E. Canet-Soulas: *Positive Contrast with Therapeutic Iron Nanoparticles at 4.7T*. **Submitted manuscript.**

Communication Proceedings

1. **A. Al Faraj**, A. Besaad, K. Cieslar, G. Lacroix, E. Canet-Soulas, Y. Crémillieux: *Evaluation longitudinale de l'impact des NTC utilisant l'IRM pulmonaire hélium-3 et proton combiné avec la microscopie optique et électronique*. **RITS2009,** Lille, France.

2. **A. Al Faraj**, F. Fauvelle, G. Lacroix, F. Lagarde, C. Richard, Y. Crémillieux, E. Canet-Soulas: *In vivo Injection of Single-Walled Carbon Nanotubes (SWCNT): noninvasive detection and biological impacts using MR techniques.* **WMI2009,** Montréal, Canada.

3. **A. Al Faraj**, F. Fauvelle, G. Lacroix, Y. Crémillieux, E. Canet-Soulas: *Injection in vivo des nanotubes de carbone: biodistribution et impact biologique par imagerie et spectroscopie de résonance magnétique (IRM et HRMAS).* **RITS2009,** Lille, France.

4. **A. Al Faraj**, A. Besaad, K. Cieslar, G. Lacroix, E. Canet-Soulas, Y. Crémillieux: *Detection and evaluation of impact of instilled carbon nanotubes. A 3-months follow-up investigation using ^{3}He, proton lung MR, optical and electronic microscopy*. **ISMRM2009,** Honolulu, Hawaii, USA.

5. K. Cieslar, **A. Al Faraj**, S. Gaillard, Y. Crémillieux: *Single acquisition time-resolved T2* mapping in lungs using HYPR ^{3}He MRI.* **ISMRM2009,** Honolulu, Hawaii, USA.

6. **A. Al Faraj**, S. Peyrol, A. Besaad, K. Cieslar, G. Lacroix, E. Canet-Soulas, Y. Crémillieux: *Multimodality Imaging Techniques to assess Biodistribution and Nanotoxicity of SWCNT*. **World Molecular Imaging 2008**, Nice, France.

7. **A. Al Faraj**, K. Cieslar, G. Lacroix, S. Gaillard, E. Canet-Soulas, Y. Crémillieux: *Assessment of Single-Walled Carbon Nanotubes (SWCNT) biodistribution and biological impact using ^{3}Helium and Proton MRI in an intrapulmonary instilled rat model*. **ESMRMB 2008**, Valencia, Spain.

8. M. Sigovan, M. Hamoudeh, **A. Al Faraj**, H. Fessi, and E. Canet-Soulas. *Positive Contrast with Therapeutic Iron Nanoparticles at 4.7T.* **ISMRM 2008**, Toronto, Canada.

9. **A. Al Faraj**, G. Lacroix, A. Besaad, Y. Crémillieux, E. Canet-Soulas: *Nanotubes de carbone en nanomedecine: biodistribution longitudinale par IRM.* **Gramm 2008**, Lyon, France.

10. **A. Al Faraj**, K. Cieslar, G. Lacroix, D. Elgarbi, S. Gaillard, E. Canet-Soulas, Y. Crémillieux : *Suivi longitudinal par IRM He3 et proton de la biodistribution de nanotubes de carbone dans un modèle expérimental d'exposition par voie aérienne.* **Gramm 2008**, Lyon, France.

11. K. Cieslar, **A. Al Faraj**, V. Stupar, Y. Crémillieux: *Imagerie radiale hautement sous-échantillonnée – Application à l'imagerie de la ventilation chez le petit animal.* **Gramm 2008**, Lyon, France.

12. **A. Al Faraj**, G. Lacroix, H. Alsaid, D. Elgrabi, V. Stupar, F. Robidel, S. Gaillard, E. Canet-Soulas, and Y. Crémillieux: *Longitudinal Helium-3 and Proton imaging of magnetite biodistribution in a rat model of instilled nanoparticles*. **ISMRM 2007**, Berlin, Germany.

13. V. Stupar, **A. Al Faraj**, H. Alsaid, E. Bannier, K. Cieslar, S. Gaillard, E. Canet-Soulas, Y. Crémillieux: *Hyperpolarized 3He MRI: a comprehensive tool for the investigation of lung function in physio-pathological animal models?* **Contrast Media Research 2007**, Banff, Canada.

14. **A. Al Faraj**, M. Hamoudeh, H. Fessi, E. Canet-Soulas: *Nanoparticules de PLLA dopées en oxyde de fer: un nouvel agent diagnostique et thérapeutique pour le suivi des tumeurs musculaires.* **JRIM 2007**, Dijon, France

15. **A. Al Faraj**: *Imagerie de Résonance Magnétique Proton et Hélium-3 des Nanoparticules*. **Journée du savoir 2007**, Dijon, France.

Abstract:
As novel engineered nanoparticles such as single-walled carbon nanotubes (SWCNT) are extensively used in nanotechnology due to their superior properties, it becomes critical to fully understand their biodistribution and effect when accidently inhaled. Therefore, development of an imaging technique which allow longitudinal in vivo follow-up of SWCNT effect based on their intrinsic properties is highly desirable. Noninvasive free-breathing hyperpolarized ^{3}He lung MRI protocol was developed complementary to proton systemic MR protocol to allow monitoring SWCNT based on their intrinsic iron impurities after intrapulmonary exposition. Combined to proton lung MRI and ex vivo optical and electron microscopy at different time points, this protocol represents a powerful multimodality imaging techniques which allows a full characterization of the biodistribution and biological impacts of iron containing SWCNT. SWCNT was found to produce granulomatous and inflammatory reactions in a time and dose dependent manner with their bio-persistence after intrapulmonary exposition.
From biological impact evaluations after intrapulmonary exposition towards biomedical applications, SWCNT hold promise for applications in nanomedicine field with their distinct architecture and their novel physicochemical properties. The biodistribution and pharmacological profile of various well-dispersed pristine and functionalized SWCNT were assessed in blood and target tissues after their intravenous administration by longitudinal in vivo susceptibility weighted MRI and their potential effect on liver metabolism by ex vivo HRMAS ^{1}H NMR. No presence of acute toxicological effect (variation in liver metabolism) was observed confirmed by the absence of clustering in NMR spectra using Principal Component Analysis (specific biomarkers of toxicity).

Keywords: HP-^{3}He MRI; Proton systemic MRI; Lung imaging; Nanoparticles; Single-walled carbon nanotubes; biodistribution and biological impact; optical and electron microscopy; HRMAS ^{1}H NMR; Raman spectroscopy.

Résumé:
En raison de leurs propriétés uniques, des nanoparticules industriellement fabriquées comme les nanotubes de carbone (NTC) ont révolutionné le domaine de la nanotechnologie. Il apparait nécessaire de développer des techniques d'investigation in vivo basées sur les propriétés intrinsèques de ces particules et permettant un suivi longitudinal pour évaluer leur risque après inhalation accidentelle par voie respiratoire. Un protocole d'IRM pulmonaire non-invasive utilisant l'hélium-3 hyperpolarisé sous respiration spontanée a été développé en complément d'un protocole d'IRM systémique proton pour permettre la détection des NTC grâce à l'effet de susceptibilité magnétique induit par les impuretés de fer, associées aux nanotubes après leur exposition intrapulmonaire. Combiné avec l'IRM pulmonaire proton et des analyses en microscopie optique et électronique à différents temps d'investigation, ce protocole d'imagerie multimodale permet d'évaluer la biodistribution et l'impact biologique des NTC bruts après exposition intrapulmonaire. Une accentuation des réactions inflammatoires (granulomes multifocaux, dépôt de fibres de collagène…) avec le temps et la dose administrée a été observée.
De l'évaluation de l'impact biologique des NTC après une exposition intrapulmonaire vers leurs applications biomédicales, les nanotubes de carbone avec leurs propriétés physicochimiques fascinantes et leur forme spécifique laissent entrevoir des applications potentielles en nanomédecine. La biodistribution et le profil pharmacologique des différents types de NTC ont été évalués longitudinalement par IRM et dosage dans le sang et les organes cibles après une injection intraveineuse, et leur impact biologique sur le métabolisme du foie a été examiné ex vivo par RMN haute résolution à l'angle magique (HR-MAS). Aucun signe de toxicité aiguë (variation du métabolisme du foie) n'a été observé et les analyses statistiques conduits sur les spectres RMN (tests PCA) ne montrent aucune différence entre les échantillons analysés et donc l'absence de discrimination entre les différents groupes par rapport aux animaux contrôles.

Mots clés: IRM hélium-3; IRM proton systémique; imagerie pulmonaire; nanoparticules; nanotubes de carbone; biodistribution et effet biologique; microscopie optique et électronique; RMN HR-MAS proton; spectroscopie Raman.